12. MICROSTRUCTURAL STABILITY OF CO-BASED ALLOYS

12.1 Introduction

The as-received microstructure of cobalt-based hardfacing alloys deposited by manual metal arc (MMA) welding, tungsten inert gas (TIG) welding, and laser cladding process was investigated in detail in Chapter 10, and the results showed that the microstructure consists of fcc primary dendrites within an interdendritic network of M_7C_3 eutectic carbides. This is not a thermodynamically stable microstructure, which for the Co-Cr-C-W system is expected to contain face-centered-cubic matrix (γ), M_7C_3, $M_{23}C_6$, and M_6C type carbides and depending upon temperature and chemical composition some hexagonal-closed-packed (hcp) ε.(1) The aim of this chapter is to investigate to what extent these phases are stable and how they influence the microstructure of these alloys. It is also of interest here to study the nucleation and growth mechanisms of the different carbides as the microstructure evolves during aging at high temperatures.

12.2 Experimental Technique

High temperature heat treatments were carried out in Stellite 6 Co-based hardfacing alloys deposited by manual metal arc welding, tungsten inert gas welding and laser cladding processes. The chemical compositions of the alloys have been given in Chapter 10. A number of 3mm diameter and 2mm thick rods were machined from the weld deposits and sealed off in a quartz tube with a partial pressure of 10^{-6} torr argon, before heat treatments. The specimens were quenched into the water after aging at $850^{\circ}C$. The thin foils were prepared from the top layer of the deposits, so that micrographs represent undiluted regions of the deposits. Thin foil preparation and microanalysis techniques were carried out as in Chapter 10.

12.3 Results and Discussion

The short time heat treatments resulted in extensive formation of $M_{23}C_6$ carbides which nucleated probably either on stacking faults (Fig. 12.1a) or on dislocations (Fig. 12.1b). At this stage the shape of the $M_{23}C_6$ carbides was not observable. As expected a cube-cube orientation relationship was observed between the fcc matrix and $M_{23}C_6$ carbides which could be explained in terms of the matching of metal atoms on the interface between the two phases as will be discussed later. Some hcp platelets were also observed as seen in Fig. 12.2. The existence of the hcp phase is not surprising since fcc and hcp structures are interrelated, each being obtained by an appropriate stacking sequence of closed-packed planes of atoms, when the region of hcp is able to form by intrinsic faulting on every alternate {1 1 1} plane in the fcc lattice.(2) It has been suggested that intersections of hcp platelets with faults on other planes create high vacancy concentrations, and therefore can promote diffusion and accommodate part of the mismatch between the matrix and the precipitate, creating preferential nucleation sites.(3) However, there is no direct evidence that this as occurred in the present study.

With increasing time, the $M_{23}C_6$ carbides were observed to grow, as shown in Figs. 12.3.a,b,c. On further growth (after 1 day at 850°C) the $M_{23}C_6$ carbides are clearly rectangular (Fig. 12.4) and after 125 hours appear in clusters (Fig. 12.5). Discontinuous M_7C_3 carbides were about 1μm long and 0.2μm wide after aging for 450 hours (Fig. 12.6). In a large number of cases, $M_{23}C_6$ carbides appeared to grow preferentially within the fcc matrix as illustrated from the bright field transmission electron micrographs from samples aged for 1 month at 850°C (Fig. 12.7). Preferential alignment of precipitates has been observed in a number of studies, and several proposals for this behaviour have been given.(4-15) It has been suggested that following the heterogenous nucleation, successive new plates are nucleated in the stress and diffusion fields of existing ones autocatalytically.(5)[1] Perovic et al.(5) have shown that strain fields around the precipitates are the major reason for subsequent nucleation and are responsible for the preferential alignment and dominance of a certain variant of precipitates. It is possible that the morphology of precipitates is controlled by elastic interaction if the overall driving force for the homegenous nucleation is small. However, when precipitates form uniformly throughout a matrix, elastic interactions between particles have been postulated to be responsible for subsequent alignment and carbide morphology during coarsening.(7,10) Although several variants of precipitates have been observed at the nucleation stage, one variant in a given region became dominant during coarsening.(7) The degree of undercooling was suggested to be an important factor in determining the initiation of alignment of precipitates.(7) If the undercooling is large then the elastic energy is small compared to the free energy change of nucleation so that evaluation of a specific variant of precipitates occurs during coarsening rather than during nucleation or growth. Under these circumstances, the influence of the elastic interactions between adjacent particles is observed after the system begins to coarsen, since the elastic interaction energy is then of the same order of magnitude as the driving force for coarsening. It has also been predicted that there is an increasing tendency towards alignment as the precipitates grow.(10) This proposal could seem to be incompatible with the high stacking fault density of the experimental alloys. The high density of faults will probably prevent heterogenous nucleation, so that the elastic interaction energy will be relatively small compared to the free energy change of nucleation. However, as emphasized earlier, the influence of elastic strain energy can be dominant during coarsening. This seems to be consistent with the experimental observations which showed that alignment begins to occur after ≈135 hours at 850°C.

Another possible reason for the alignment of precipitates has been shown to be an applied stress.(9,11-13) This makes certain planes favourable for precipitation and growth along a direction where the stress is better minimised. This possibility can be ruled out easily since the aging heat

---

[1] Autocatalytic nucleation, the process whereby one precipitate of a daughter phase catalyses the formation of another. This is a well-documented phenomenon in martensite transformations.(5)

treatments were carried out in stress-free conditions.

The third possibility is that the residual stresses within the deposits can influence subsequent alignment. This statement has been supported by a number of experiments showing that residual stresses cause a preferential precipitation and growth on certain variants of precipitates.(10,11) A schematic diagram is illustrated in Fig. 12.8 in order to explain the nature of the carbide growth. Initially, stacking faults exist on a particular variant of the four possible {1 1 1} planes due to residual stresses within the deposits. Nucleation of the carbides on the stacking faults leads to the formation of one set of carbides on a particular {1 1 1} plane. Subsequently, growth takes place and supersaturation is released from the matrix phase. This suppresses further nucleation of carbides on new faults as seen in Fig. 12.7. It should be also pointed out that the distribution of stresses within weld deposits may be complex so that tensile and compressive stresses can be present together. This creates further difficulties since the tensile and compressive stresses lead to preferential precipitation at different directions.(9,11,13,14) During tension, precipitation is favoured on planes perpendicular to the stress axis, whereas in compression precipitation takes place on planes parallel to the stress axis.

From these discussions, it is reasonable to suggest that either the elastic interactions between particles during coarsening or the residual stresses within deposits or both are responsible for the alignment of $M_{23}C_6$ carbides during aging.

The morphology of precipitates sometimes depends on the nature of the precipitate-matrix interface.(16-18) Hence, studies were carried out on the main interface planes between the matrix and the precipitates.

12.3.1 Habit Plane Determination

The crystallography of the habit plane was carried out using single-surface trace analyses performed with transmission electron micrographs and corresponding diffraction patterns.

The lens optics used in transmission electron microscopes result in a rotation of the image with respect to the diffraction pattern. The rotations were calibrated over a range of magnifications and camera lengths by use of MoO_3 crystals, which have facetted surfaces of known indices. Using the straight interface trace of the habit plane, (Fig. 12.9a) the trace analyses were carried out as follows (Fig. 12.9b);

(1) The normal $\underline{n}$ (hkl), to the trace was marked on the bright field image.

(2) The indexed diffraction pattern was then placed upon the bright field image and rotated into coincidence.

(3) The angles (θ_i) of the trace normal, $\underline{n}$, from two $\underline{g}$ vectors in the diffraction pattern were measured.

(4) The two $\underline{g}$ vectors are used to calculate the zone axis, [UVW].

(5) The indices of $\underline{n}$ were determined.

It is likely that the fcc matrix/$M_{23}C_6$ interface will be at an angle θ to the plane of the thin foil sample. However, its true normal (HKL) must lie on the great circle on the stereogram defined by the measured trace normal (hkl) and the zone axis of the diffraction pattern [UVW]. The great circle thus defined represents the locus of the possible positions of the habit plane normal so that the intersection of many such great circles can give the actual habit plane normal. A great number of trace analyses are needed in order to establish the existence of any reproducible irrational habit plane, otherwise the method can be ambiguous. However, the habit plane can be determined from a single bright field image and corresponding diffraction pattern if the thickness of the thin foil and the projected thickness of the precipitate are known. The thickness of the thin foil was determined as follows;

(i) The great circle defined by the measured trace normal to the stacking fault and the zone axis of the diffraction pattern [UVW] was drawn on a stereogram.

(ii) The angle θ between the zone axis and the {1 1 1} pole on the stereogram was measured. θ defines the angle between the zone axis and the habit plane normal since stacking faults lie on {1 1 1} planes of fcc phase.

(iii) The thickness of the thin foil was then calculated for a given projected width of the fault as illustrated in Fig. 12.9c.

The local thickness determined in this manner was used in conjunction with the projected width of the particle habit to determine the angle θ between the interface normal of the $M_{23}C_6$ and the zone axis. Thus, the fcc matrix/$M_{23}C_6$ interface plane could be indexed uniquely on a great circle.

The analysis revealed that the habit plane corresponds to {1 1 1} $M_{23}C_6$ which is parallel to {1 1 1} fcc matrix. The analyses of planar atomic configurations of $M_{23}C_6$ and fcc phases provide an explanation of the interface plane.(19) The crystal structure of $M_{23}C_6$ is a complex cubic with 92 metal atoms and 24 carbon atoms per cell. On the basis of this information, the atomic configurations on the {1 0 0}, {1 1 0} and {1 1 1} planes of both $M_{23}C_6$ and fcc matrix are shown in Fig. 12.10a,b,c.(23) These figures clearly demonstrate that {1 1 1} planes provide the best atomic correspondence, in which case only four atoms out of 28 are not full in the $M_{23}C_6$ plane resulting in the overall 0.99% misfit. However, in the case of {1 1 0} planes, only fourteen $M_{23}C_6$ atoms coincide with the fcc lattice. In the case of {1 0 0} planes $M_{23}C_6$ lattice has only thirteen atoms in the interface compared with 25 atoms in the fcc lattice. Consequently thirteen $M_{23}C_6$ atoms are all in positions which correspond closely to the fcc lattice. This observation indicates that {1 1 1} planes are the most likely interface planes and the chance of the {1 1 0} planes being an interface plane is greater than for the {1 0 0} planes. In fact, the trace analyses confirmed that the interface plane is {1 1 0} type at the ends, and {1 1 1} type at the sides of the plates, consistent with the observed anisotropy in the interfacial free energy which results in the plate shape. The orientational dependence of interfacial free energy leads to an equivalent orientation dependence of the mechanism and kinetics of the precipitate growth.(20-22) Since interfaces parallel to {1 1 0} planes are likely to be relatively disordered compared with those parallel to {1 1 1} planes, they should be more mobile. Lewis and Hattersley have shown that the facets which develop on one side of the $M_{23}C_6$ particles have {1 1 1} interfacial planes.(23) It has been suggested that these carbides grow into the grain with which carbides have limited coincident lattice relationship(24) leading to discontinuous precipitation.(23,25) A similar conclusion has been drawn by Speich and Oriani(26) who found that the ends of the rod shape particles have relatively poor crystallographic fit. These results are consistent with the common observation of the precipitation of plates with the long axis of the plane of the plate having interfaces with good crystallographic fit.(27)

Some carbides have been found almost in cubic shape (Fig. 12.11). In this case no joining of carbides has been observed. This is consistent with the work of Beckitt and Clark(28) who found that $M_{23}C_6$ particles are almost cubic in shape and grow until they join together. The matrix after 1000 hours was found to be fcc with a significant amount of hcp platelets (Fig. 12.12).

After heat treatment for one year at 850°C it was discovered that there are in fact two different carbide morphologies that may be adopted. Firstly, the carbides may be aligned. In this case, scanning electron microscopy reveals a parallel array of plates each about 10μm long, and all preferentially orientated within the matrix (Fig. 12.13a). Alternatively, the carbides exist as discrete irregular particles 1-2μm in diameter and with no favoured orientation (Fig. 12.13b). When the preferential coarsening of specific variants of precipitates takes place, each grain of a deposit is altered differently, depending on the grain orientation resulting in the observed microstructure after one year.

Transmission electron micrographs corresponding to the different morphologies indicate that the carbides tend to be in a disc shape, which is probably the equilibrium shape representing the minimum strain energy morphology (Figs. 12.14a,b). The crystal structure of the matrix was found to be fcc containing a great amount of annealing twins as evidenced from the inserted diffraction pattern in Fig. 12.14a.

Microanalysis experiments were carried out using transmission electron microscopy in the MMA and laser clad samples. The results showed a decrease in the Cr, Fe, and W concentrations in the fcc matrix compared with the initial composition. The difference in the chemical compositions probably arises because the fcc matrix after solidification has a composition corresponding to the temperature of configurationally freezing, whereas the aging introduces equilibrium composition. The microanalysis results in the present study indicate that the chemical composition of eutectic carbides after aging 1 year at 850°C is not significantly different than that of as-received condition. It is interesting to note that the composition of $M_{23}C_6$ carbides is quite similar to that of the eutectic carbides. The small variations arise because $M_{23}C_6$ carbides first nucleated in the supersaturated matrix.

Table 12.1: Microanalytical data obtained using transmission electron microscopy and energy dispersive X-ray analysis. Z refers to the atomic percent calculated without taking account of the presence of carbon. Notice that Z is very nearly the same as the actual atomic percent for the matrix, since the amount of carbon in the matrix is rather small, but for the carbide, Z will represent an overestimation of the actual atomic percent by a factor (1/0.7), assuming that the M_7C_3 carbide is stoichiometric.

	Matrix		$M_{23}C_6$		Eutectic Carbide	
	MMA	Laser	MMA	Laser	MMA	Laser
Z_{Co}	61.8	71.0	12.6	15.81	12.67	15.5
Z_{Cr}	23.0	20.8	78.9	77.3	80.65	77.2
Z_W	0.73	1.01	3.18	3.62	2.0	3.42
Z_{Fe}	8.8	4.7	2.5	1.66	2.59	1.85
Z_{Mn}	0.36	2.12	0.27	1.58	0.05	2.18
Z_{Ni}	3.2	-	1.09	-	0.64	-

The selected area diffraction patterns from the eutectic carbides (inserted in Fig. 12.15a) showed that these are $M_{23}C_6$ type carbides, indicating that eutectic M_7C_3 carbides transformed to $M_{23}C_6$ during aging. The M_7C_3 to $M_{23}C_6$ transformation has been proposed to occur *in situ*(29) and by separate nucleation.(30,31) It has been suggested that variations in chemical composition of the carbides lead to the *in situ* transformation.(29) However, it has been argued that an *in situ* transformation requires diffusion of substitutional alloying elements within a carbide so that such diffusion will be much slower compared with the diffusion in the matrix.(31) The relatively low interfacial energy of the matrix/particle interface compared to that of carbide/carbide boundaries within the particle suggested that nucleation at the interfaces is more probable.(31) In Co-based superalloys the M_7C_3 carbides have been found to transform to more stable $M_{23}C_6$ carbide during aging.(32) The following decomposition reaction has been suggested.(32)

$$23\ Cr_7C_3 = 7Cr_{23}C_6 + 27C \qquad .....(1)$$

$$6\ C + 23Cr = Cr_{23}C_6 \qquad .....(2)$$

There is no indication of separate nucleation of $M_{23}C_6$ carbides at the M_7C_3/fcc matrix interfaces as evidenced from transmission electron micrographs in the the samples aged up to 1000 hours. Furthermore, assuming that $M_{23}C_6$ nucleates at those interfaces, then the facetted advancement of the carbide interface will be the most likely growth mechanism of these carbides. However, eutectic carbide/matrix interfaces are clearly irregular, suggesting that an *in situ* transformation mechanism is likely to be dominant. However, the mechanism is not clear, and, as yet, has to be determined.

12.4 Conclusions

The high temperature microstructural stability of Co-based Stellite 6 alloys deposited by manual metal arc welding, tungsten inert gas welding, and laser cladding processes has been investigated by annealing at 850°C. In the as-deposited condition the face-centred-cubic matrix contains a high density of stacking faults which lie preferentially on a particular variant of {1 1 1} plane due to residual stresses within each deposit. For a given thermal activation, the $M_{23}C_6$ carbides nucleate on the stacking faults and dislocations. With increasing time, two different carbide morphologies are observed; $\approx 10\mu m$ long continuous carbides which are preferentially orientated in the matrix, and discrete irregular particles with no favoured orientation. The elastic interaction between precipitates during coarsening or the residual stresses or both are probably responsible for the alignment of precipitates. Trace analysis has indicated that long axis of the $M_{23}C_6$ platelets have {1 1 1} type, and the ends have {1 1 0} type interfacial planes. The overall mismatch is only 0.99% when the {1 1 1} planes of the fcc matrix coincide with the {1 1 1} $M_{23}C_6$ planes. This good crystallographic fit is probably the reason for low mobility of those interfaces. The platelets having {1 1 0} planes are relatively disordered and possess less obstacles to growth, giving rise to high mobility of these faces resulting in an observed carbide morphology.

After aging for 1 year at 850°C, the particles were found to be disc-shaped. This is probably their equilibrium morphology, and has resulted due to the minimisation of strain energy. The interdendritic M_7C_3 carbides were found to have transformed to the $M_{23}C_6$ during the aging process. Even though an *in situ* growth mechanism is less probable than separate nucleation of carbides on the carbide/matrix interfaces, there was no strong evidence to verify the actual transformation mechanism.

12.5 References

1) S. HAMAR-THIBAULT, M. DURAND-CHARRE, and B. ANDRIES: Metall. Trans. A, 1982, **12A**, 545.
2) J. B. VANDER SANDE, J. R. COKE, and J. WULFF: Metall. Trans. A, 1976, **7A**, 389.
3) K. RAJAN: Metall. Trans. A, 1982, **13A**, 1161.
4) W. M. STOBBS, and G. R. PURDY: Acta Metall., 1978, **26**, 1069.
5) V. PEROVIC, G. R. PURDY, and L. M. BROWN: Acta Metall., 1981, **29**, 889.
6) V. PEROVIC, G. R. PURDY, and L. M. BROWN: Acta Metall., 1979, **27**, 1075.
7) R. J. RIOJA, and D. E. LAUGHLIN: WHO WHO
8) J. M. OBLAK, D. F. PAULONIS, and D. S. DUVALL: Metall. Trans. A, 1974, **5**, 143.
9) M. R. LOUTHAN: Trans. AIME, 1963, **227**, 1166.
10) A. J. ARDELL, and R. B. NICHOLSON, (with the Appendix J. D. ESHELBY): Acta Metall., 1966, **14**, 1295.
11) Y. NAKADA, W. C. LESLIE, and T. P. CHURAY (with the Appendix J. C. M. LI): Trans. ASM, 1967, **60**, 223.
12) T. ETO, A. SATO, and T. MORI: Acta Metall., 1978, **26**, 499.
13) W. H. HOSFORD, and S. P. AGRAWAL: Metall. Trans. A, 1975, **6A**, 487.
14) J. K. TIEN, and S. M. COPLEY: Metall. Trans. A, 1971, **2A**, 543.
15) S. H. WEN, A. G. KHATCHATURYAN, and J. W. MORRIS: Metall. Trans. A, 1981, **12A**, 581.
16) G. J. COCKS, R. A. LEGGE, and D. R. MILLER: Met. Sci. J., 1980, **14**,480.
17) J. V. BEE, P. R. HOWELL, and R. W. K. HONEYCOMBE: Metall. Trans. A, 1979, **10A**, 1049.
18) P. R. HOWELL, J. V. BEE, and R. W. K. HONEYCOMBE: Metall. Trans. A, 1979, **10A**, 1313.
19) K. H. KUO, and C. L. JIA: Acta Metall., 1985, **33**, 991.
20) H. I. AARONSON, H. B. AARON, and K. R. KINSMAN: Metallography, 1971, **4**, 1.
21) H. I. AARONSON, J. K. LEE, and K. C. RUSSELL: in Proc. Conf. 'Precipitation Processes in Solids', 1976, The Metallurgical Society of AIME, 31.
22) P. R. HOWELL, and R. W. K. HONEYCOMBE: in Proc. Conf. 'Solid-Solid Phase Transformations', August 10-14, 1981, Pittsburgh Pennsylvania, U.S.A, The Metallurgical Society of AIME, 399.
23) M. H. LEWIS, and B. HATTERSLEY: Acta Metall., 1965, **13**, 1159.
24) L. K. SINGHAL, and J. W. MARTIN: JISI, 1967, **205**, 947.
25) E. J. DULIS: ISI Special Report, 1964, **86**, 162.
26) G. R. SPEICH, and R. A. ORIANI: Trans. Met. Soc. AIME, 1965, **233**, 623.
27) G. R. PURDY: Met. Sci. J., 1971, **5**, 81.
28) F. R. BECKITT, and B. R. CLARK: Acta Metall., 1967, **15**, 113.
29) R. W. K. HONEYCOMBE, and A. K. SEAL: JISI, 1958, **188**, 9.
30) T. M. F. RONALD, and C. BODSWORTH: JISI, 1965, **203**, 252.
31) J. BEECH, and D. H. WARRINGTON: JISI, 1966, **204**, 460.
32) C. T. SIMS, N. S. STOLOFF, and W. C. HAGEL (Eds.), "Superalloys II", John Wiley & Sons, New York, 1987.

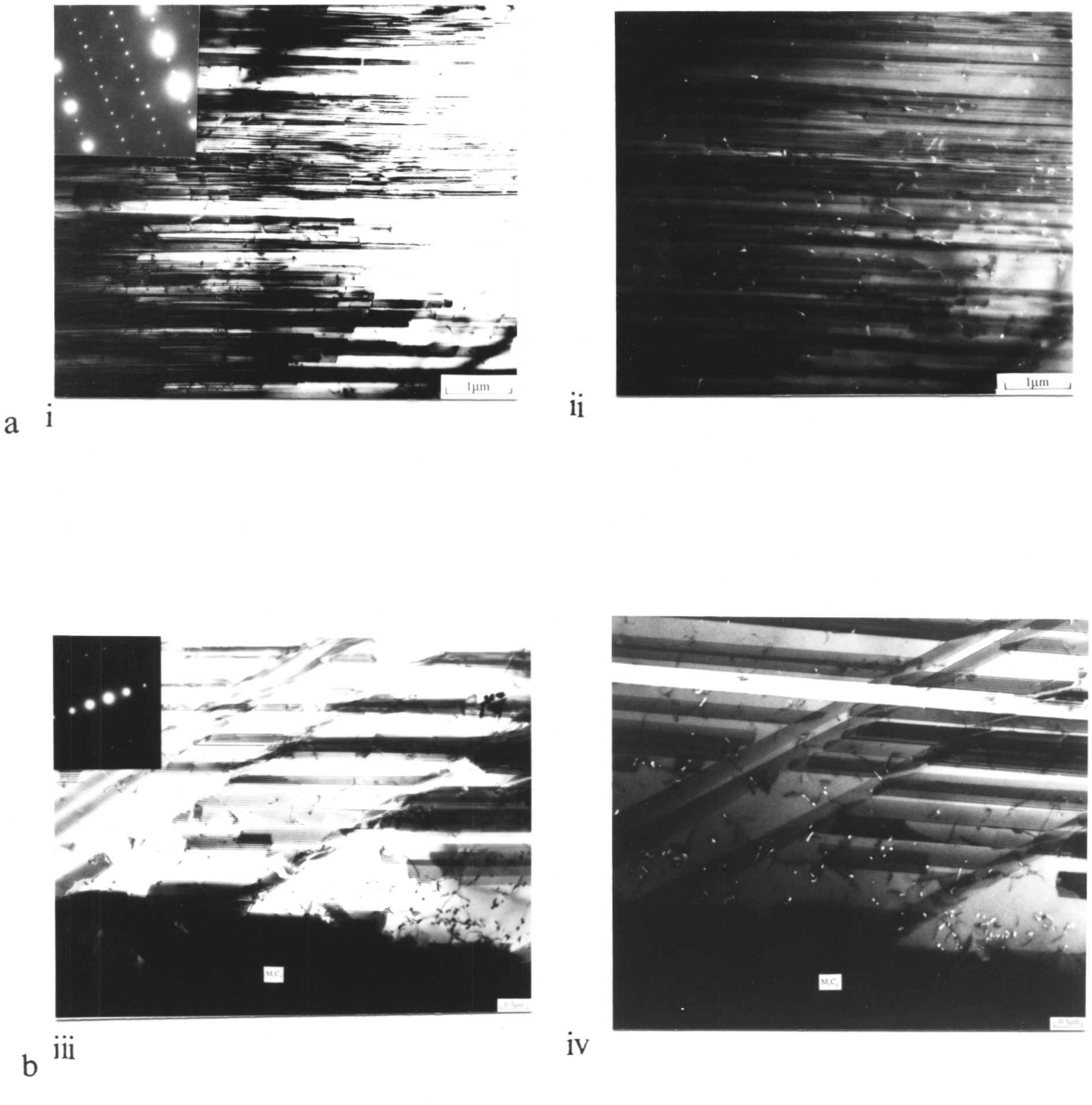

Fig. 12.1 : Transmission electron micrographs of the MMA deposit aged 130 seconds at 850^{o}C showing the nucleation of $M_{23}C_6$ carbides. a) on stacking faults, i) bright field image; ii) dark field image of the carbides; b) on dislocations; iii) bright field image; iv) dark field image of the carbides using a (224) $M_{23}C_6$ spot which coincides with (01.0) hcp spot. The diffraction patterns in the insets show the cube-cube orientation relationship between the fcc matrix and $M_{23}C_6$ carbides.

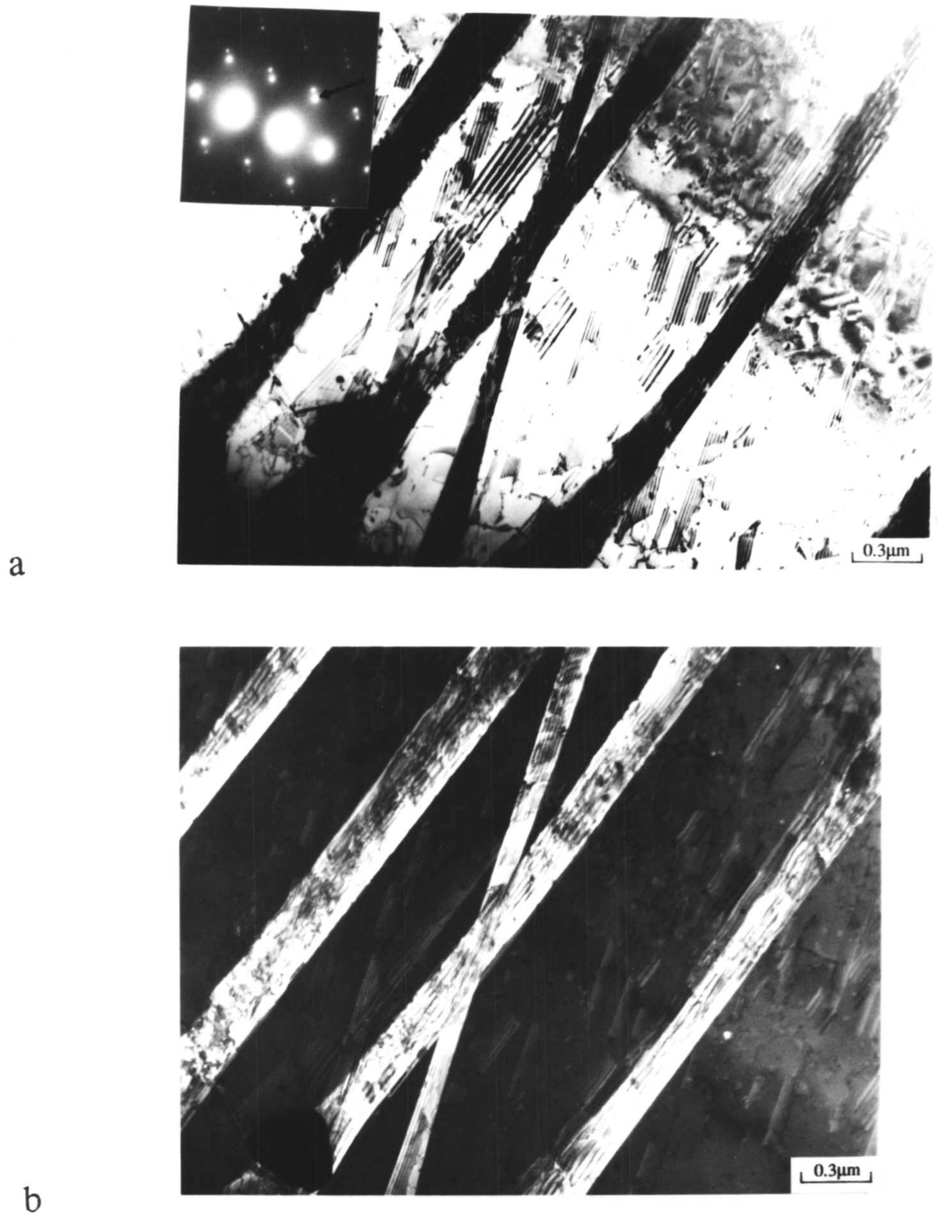

Fig. 12.2 : Transmission electron micrographs of the MMA deposit aged 120 seconds at 850°C. a) bright field image; b) dark field image using a $(01.0)_{hcp}$ spot (marked with arrow) showing a high density of hcp platelets.

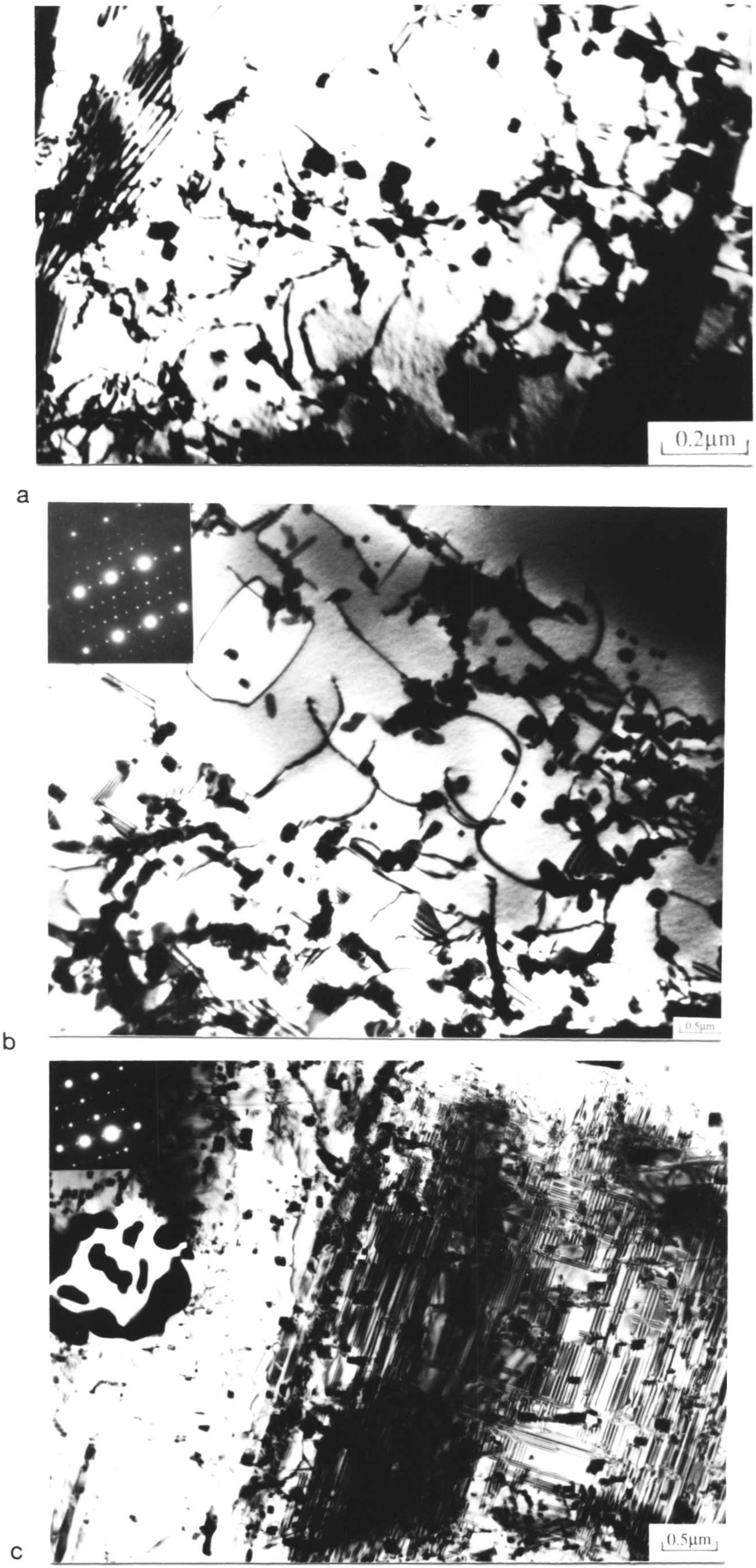

Fig. 12.3 : Bright field transmission electron micrographs of the deposits aged at 850^{o}C after different aging times. a) MMA deposit after 10min; b) laser clad deposit after 30min; c) TIG deposit after 1 hour.

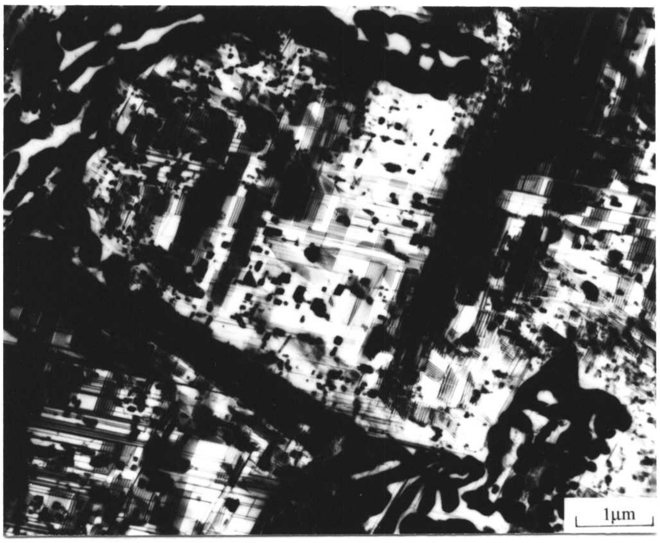

Fig. 12.4 : Transmission electron micrograph of the TIG deposit after 24 hours.

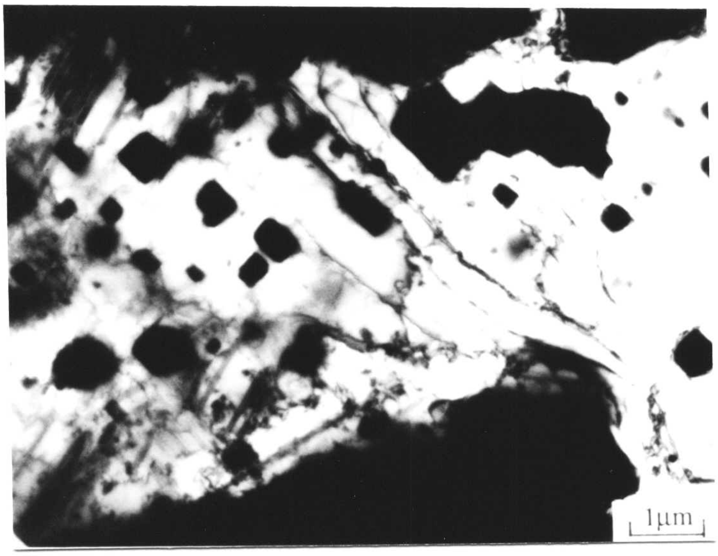

Fig. 12.5 : Bright field transmission electron micrograph of the MMA deposit after 300 hours showing joining of $M_{23}C_6$ carbides.

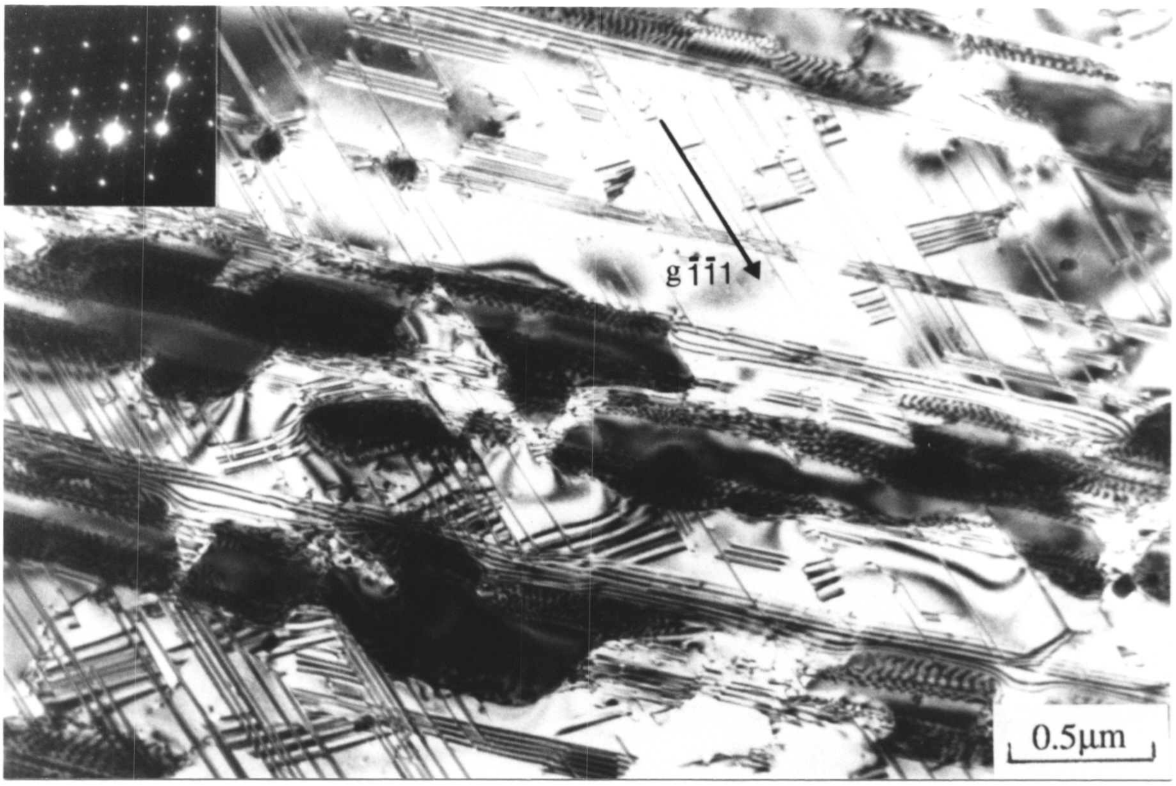

Fig. 12.6 : Bright field transmission electron micrograph of the MMA deposit showing discontinuous $M_{23}C_6$ carbides after 450hrs.

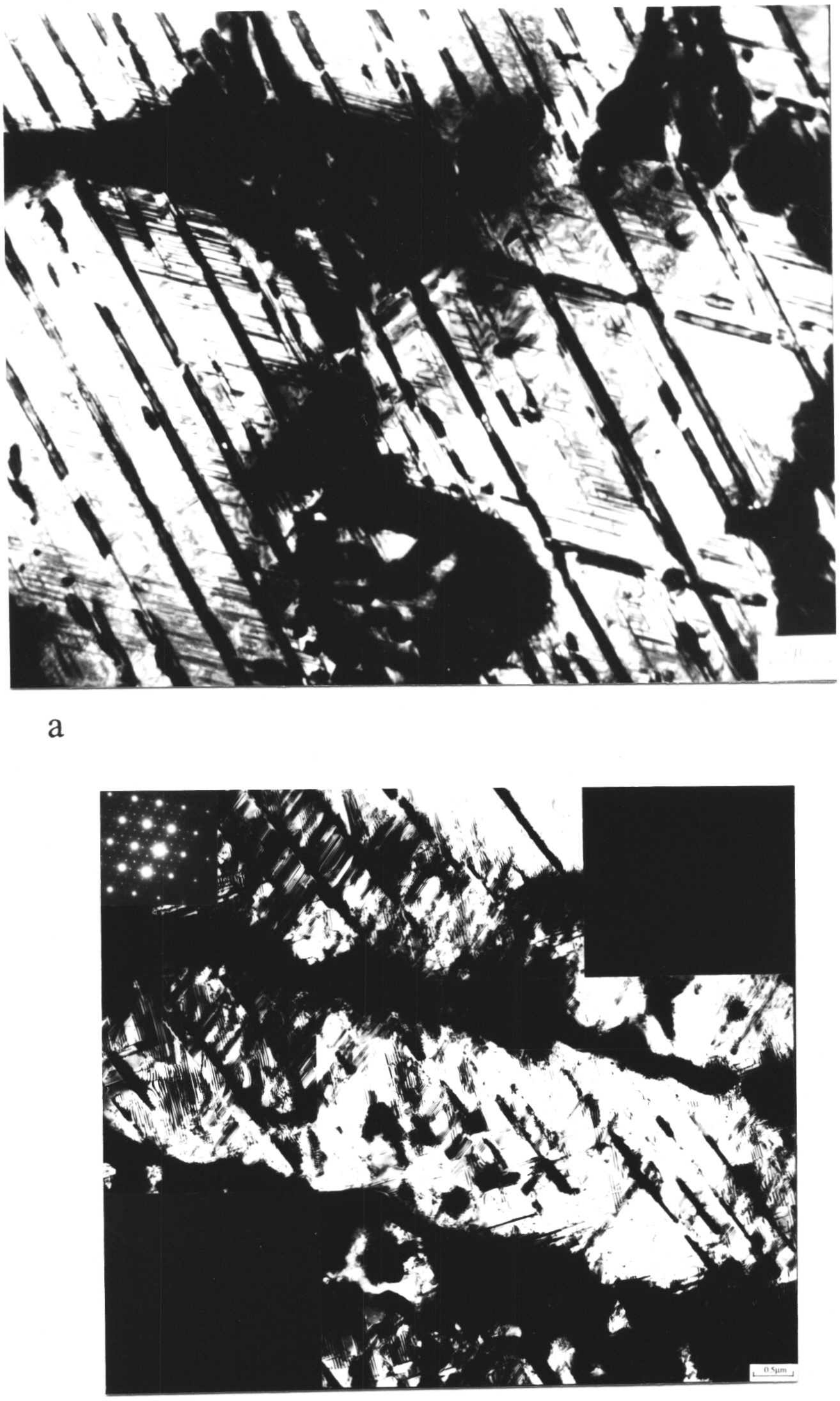

Fig. 12.7 : Bright field transmission electron micrographs after 750hrs showing continuous preferentially orientated $M_{23}C_6$ carbides in the a) MMA; b) laser clad deposit

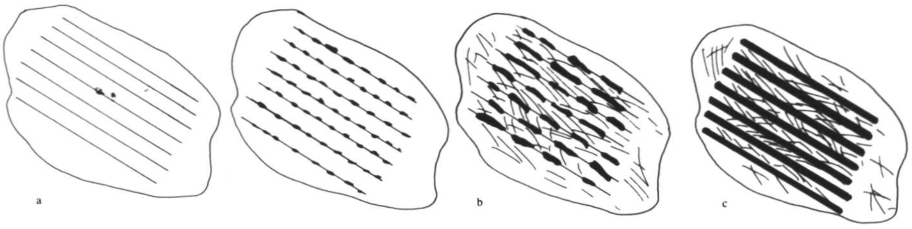

Fig. 12.8 : Schematic representation of the carbide growth mechanism. a) Stacking faults exist preferentially on a particular variant of {1 1 1} planes due to residual stresses; b) nucleation of $M_{23}C_6$ carbides leads to formation of one set of carbides; c) joining of carbides leads to formation of continuous carbides. Since the supersaturation is released from the matrix, further nucleation on the stacking faults is suppressed.

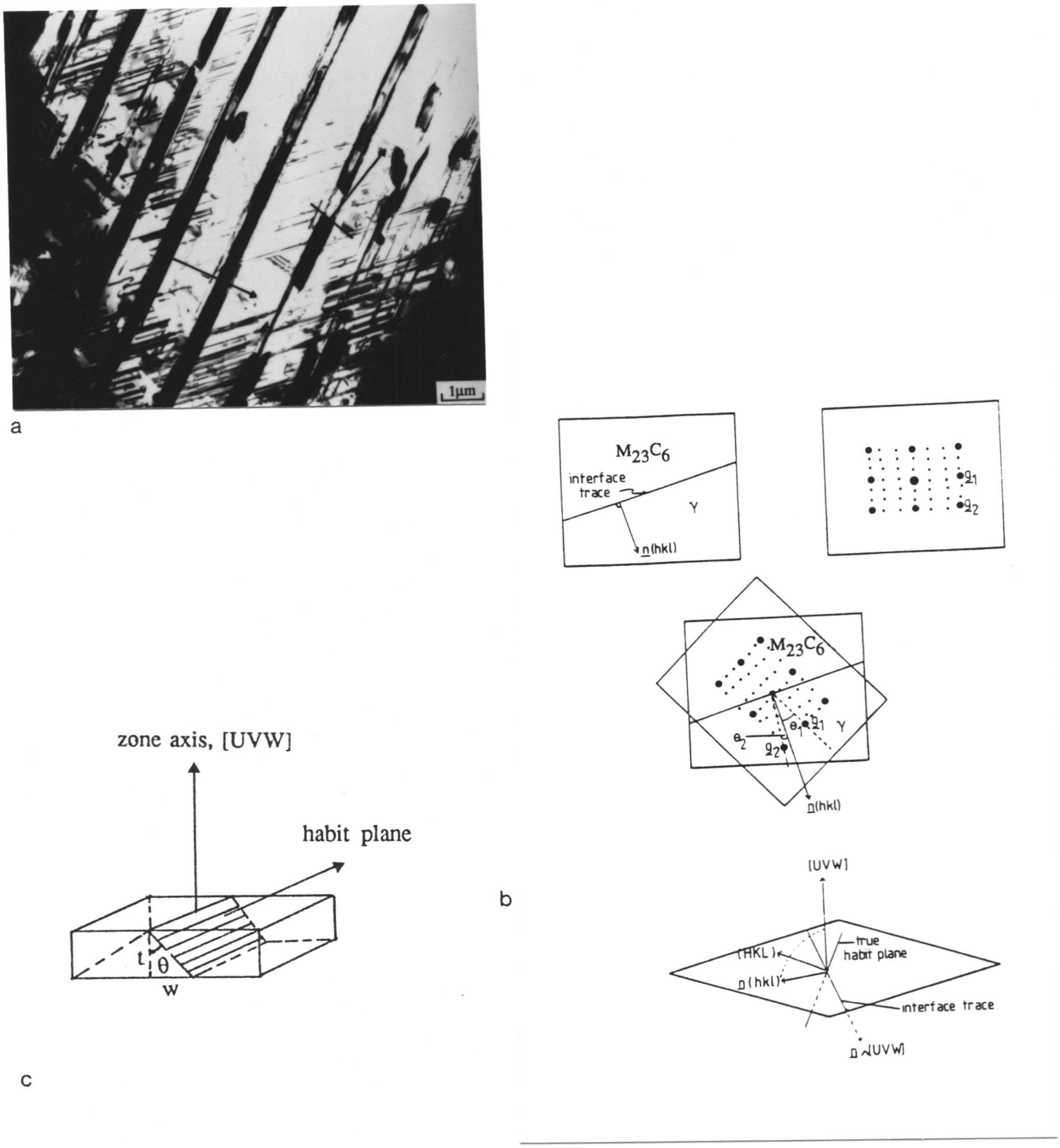

Fig. 12.9 : a) $M_{23}C_6$ plates and stacking faults indicating mean interface traces and normals n (hkl); b) stages in determination of the fcc matrix/$M_{23}C_6$ habit plane; c) diagram illustrating the geometry of a precipitate within a thin foil.

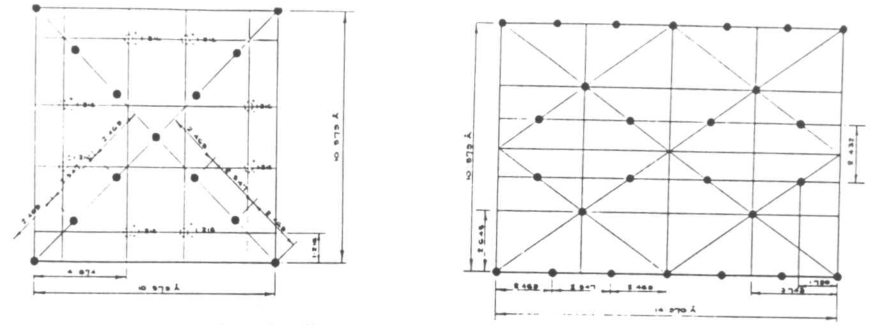

{1 0 0} plane for $M_{23}C_6$ unit cell

{1 1 0} plane for $M_{23}C_6$ unit cell

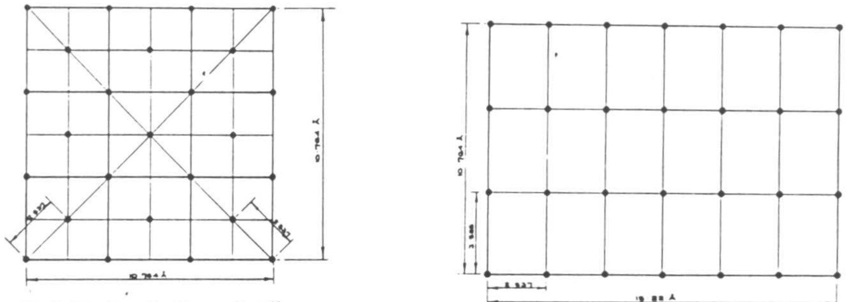

{1 0 0} plane for 9 γ unit cells

{1 1 0} plane for 9 γ unit cells

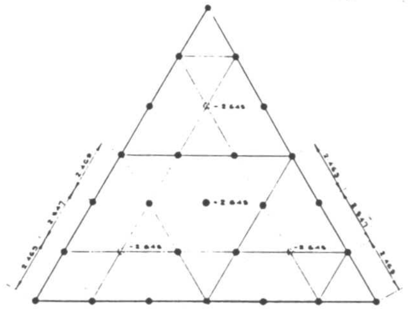

{1 1 1} plane for $M_{23}C_6$ unit cell

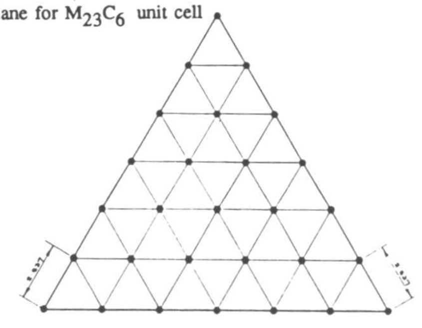

{1 1 1} plane for γ unit cell

Fig. 12.10 : Atomic configurations of both $M_{23}C_6$ and fcc crystals on a) {1 0 0 }; b) {1 1 0); c) {1 1 1} planes.

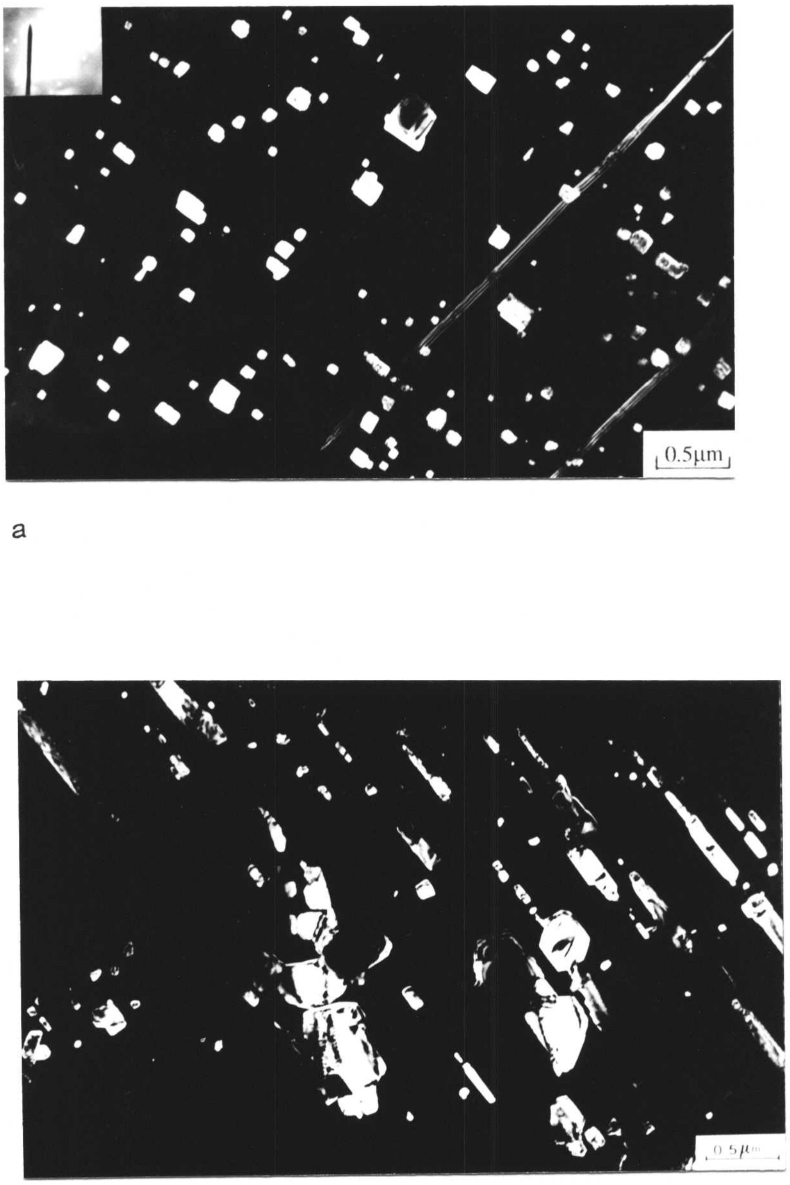

Fig. 12.11 : Dark field transmission electron micrographs after 1000 hours showing facetted $M_{23}C_6$ particles. a) TIG; b) laser clad deposits. Note that carbides are discontinuous and joining does not take place.

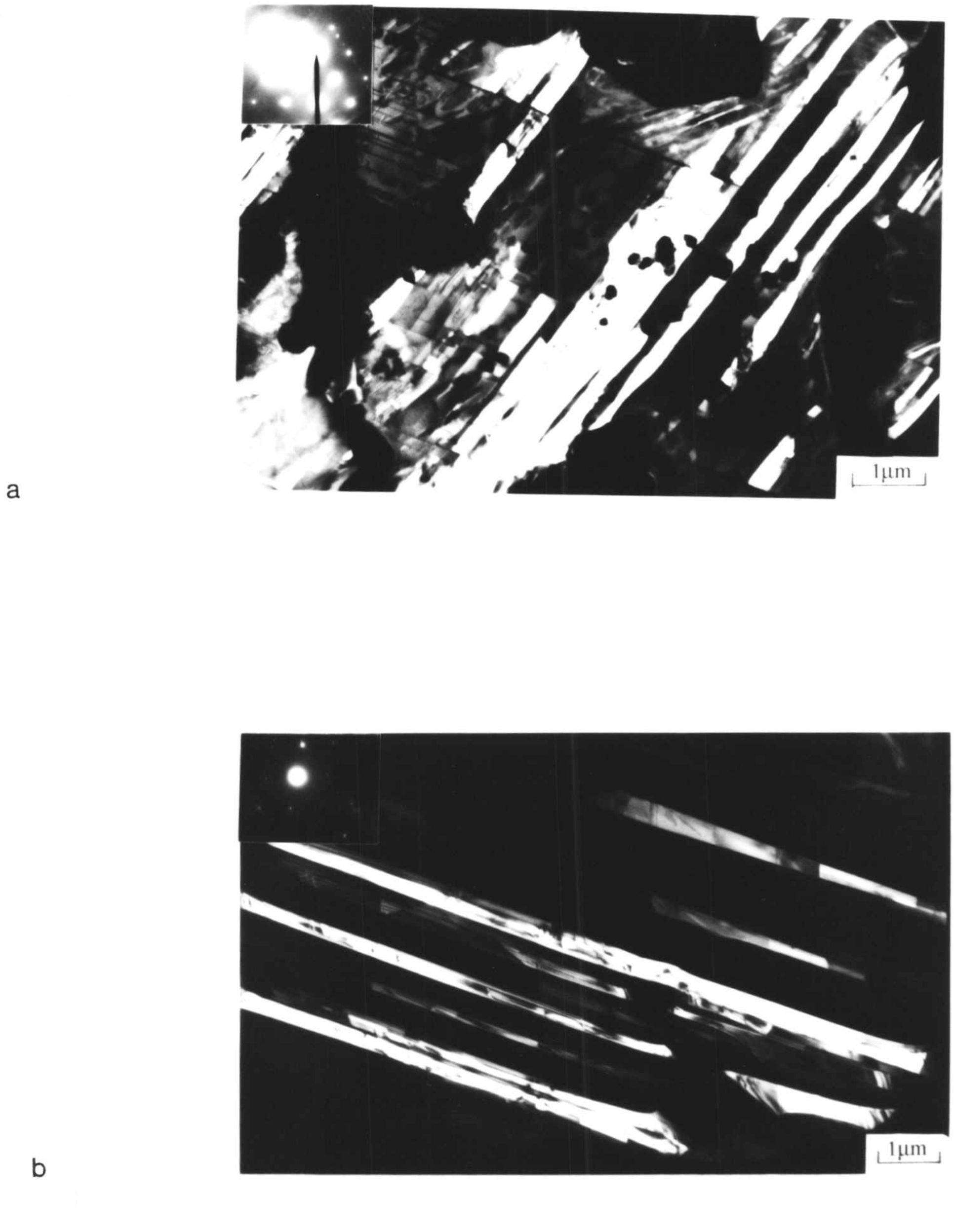

Fig. 12.12 : Dark field transmission electron micrographs after 1000 hours showing hcp platelets in the fcc matrix. a) TIG; b) laser clad samples.

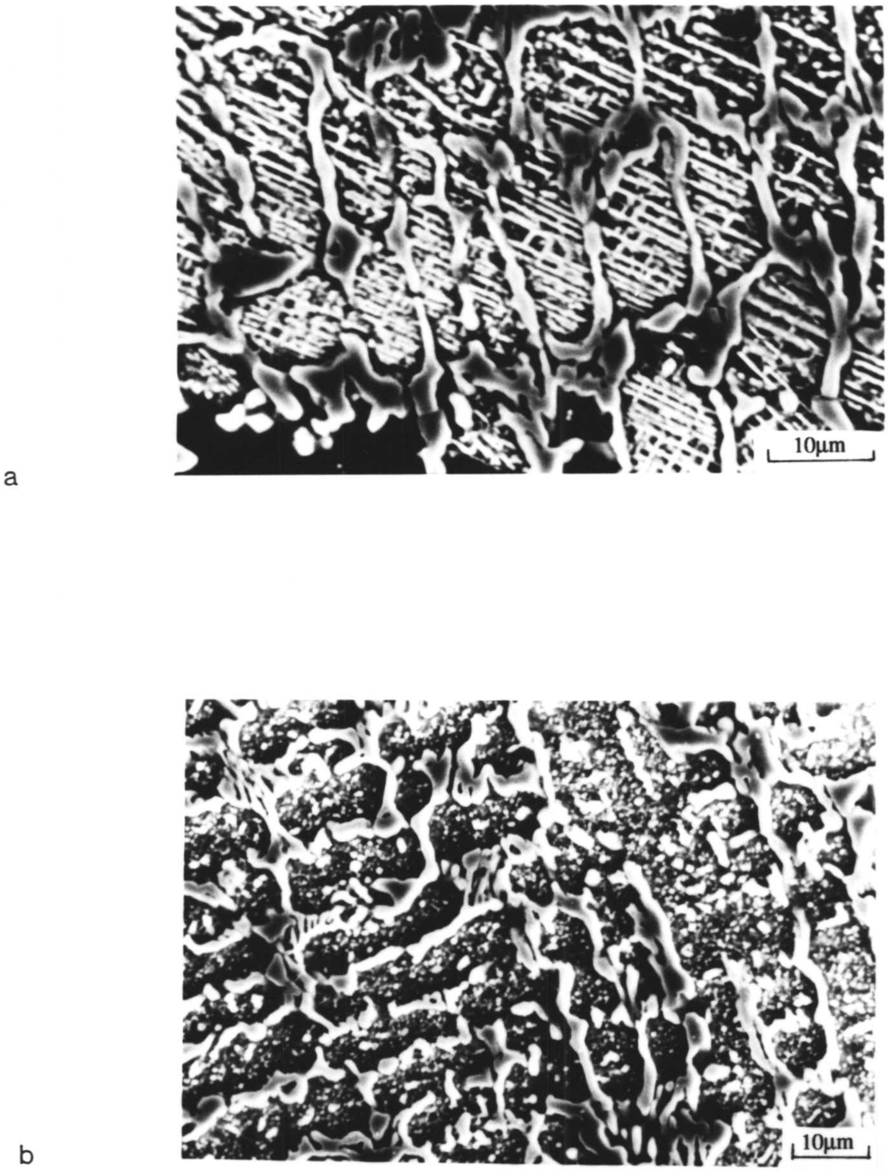

Fig. 12.13 : Scanning electron micrographs of the MMA deposit aged 1 year at 850^{o}C showing, a) continuous parallel array of platelets, and b) discrete irregular particles.

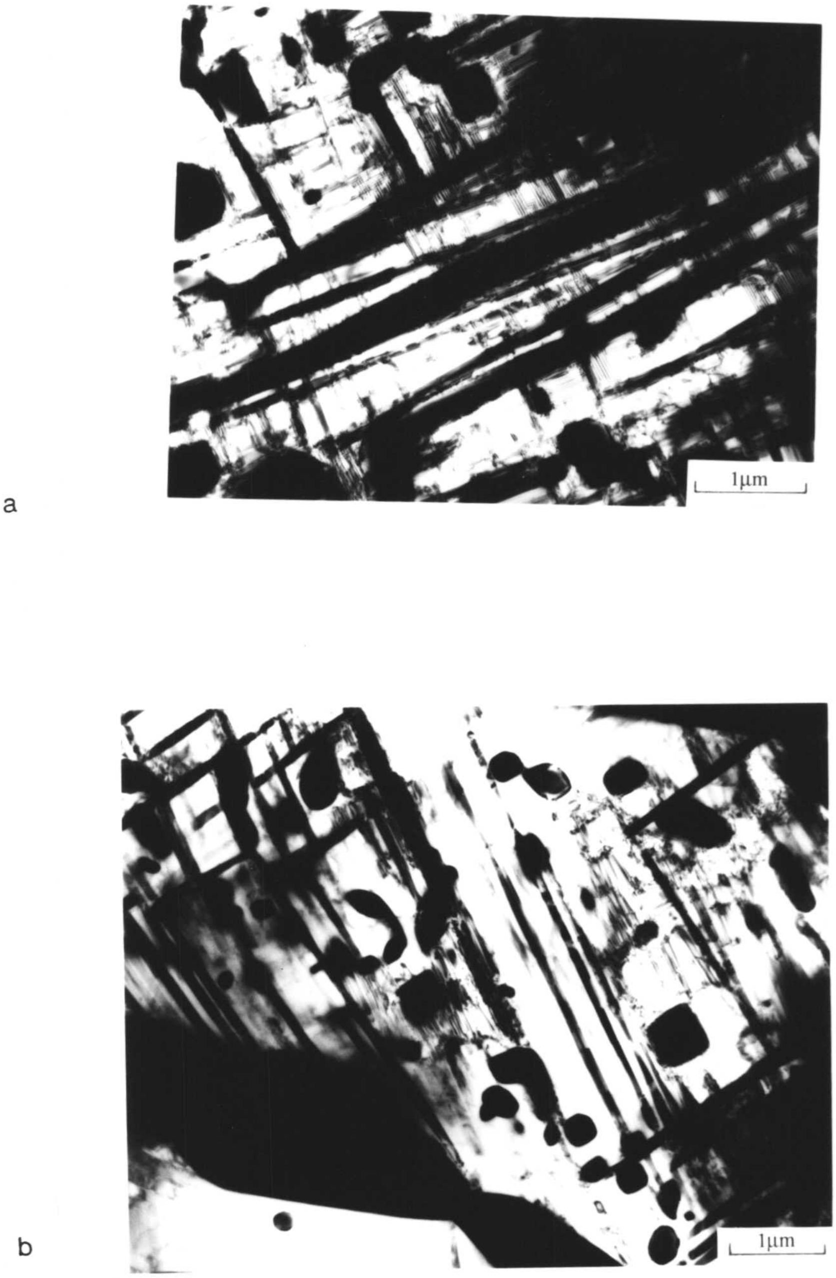

Fig. 12.14: Bright field transmission electron micrographs of the MMA deposit aged 1 year. a) Continuous long carbides; b) discrete irregular particles.

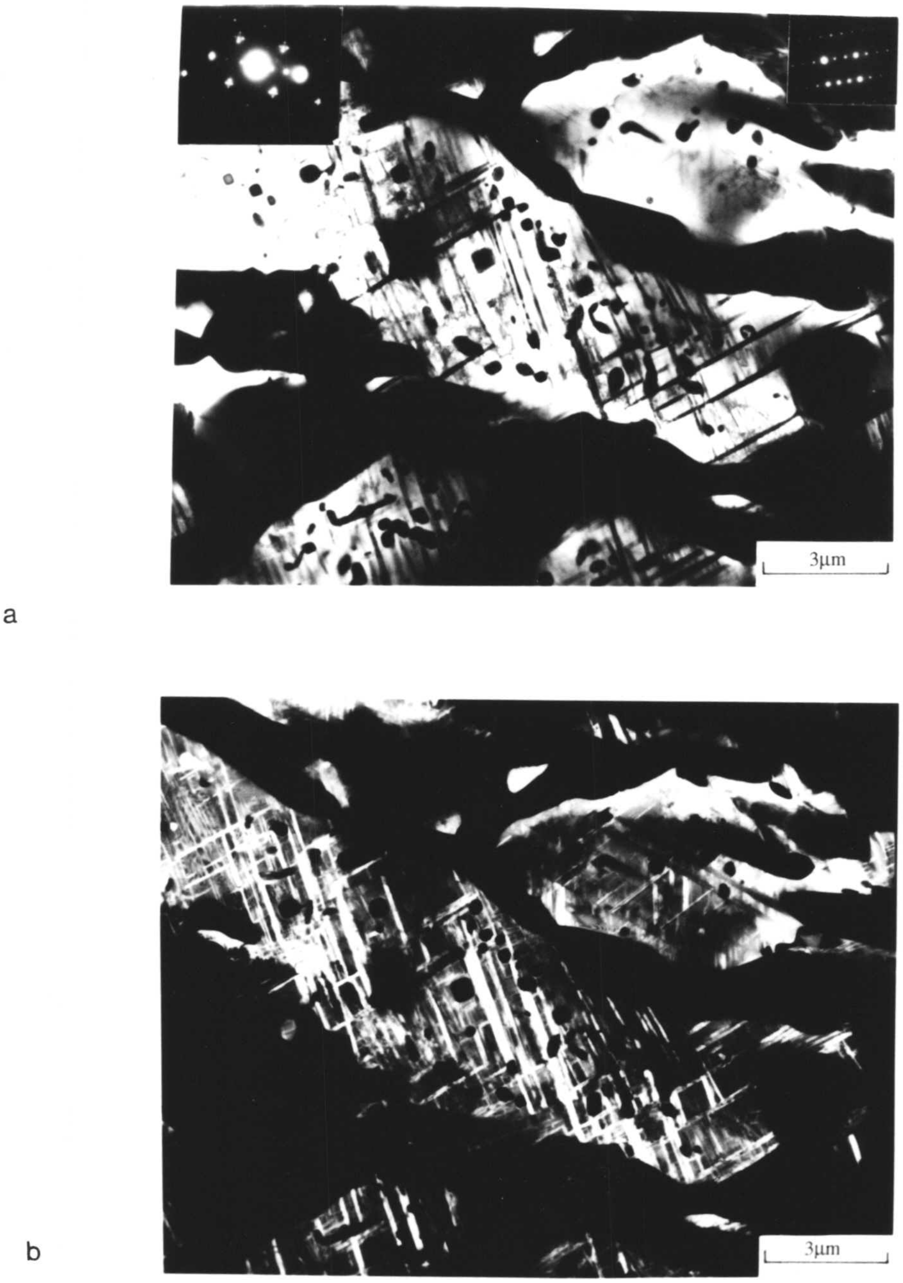

Fig. 12.15: Transmission electron micrographs of the MMA deposit aged 1 year. a) Bright field image consists of the eutectic carbides and the fcc matrix with annealing twins and $M_{23}C_6$ carbides. Selected area diffraction pattern from the interdendritic carbides is given in the right-hand corner; the zone axes of the pattern is $<0\ 1\ 2>_{M_{23}C_6}$ indicating that interdendritic M_7C_3 carbides transformed to $M_{23}C_6$ during aging. Selected area diffraction pattern from the matrix is given in the left-hand corner showing $<0\ 0\ 1>_{fcc}$ twinning; d) dark field image showing fcc twins.

13. NICKEL-BASED HARDFACING ALLOYS FOR HIGH TEMPERATURE APPLICATIONS

13.1 Introduction

Nickel-based hardfacing alloys typically are single phase alloys used where the component does not operate at high temperatures for prolonged periods of time. The alloys are usually deposited by arc welding techniques and provide a tough, wear-resistant and work-hardening surface. The alloys cannot maintain their strength at high temperatures (e.g. 800°C) due to the absence of stable precipitates.

Even though there have been some attempts to strengthen the alloys by the addition of boron and carbon,(1) the modified alloys are not as popular as Co-based hardfacing alloys. Unlike the Ni-based superalloys used in aircraft engines, where high temperature strength, toughness, wear and corrosion resistance are also important, the alloys used for hardfacing do not for some reasons contain aluminium or titanium. The addition of these elements is well established to lead to the formation of γ' ($Ni_3(Al,Ti)$) precipitates in the face-centered-cubic (fcc) γ matrix. Some Ni-based superalloys also contain topologically-closed-packed (TCP) phases (e.g. sigma, mu, chi, and Laves) depending on the composition and heat treatment. These hard phases are generally avoided due to their detrimental effects on mechanical properties. However, they can increase wear resistance in high temperature hardfacing applications through their high hardness.(1) Understandably, the design of these new alloys tends to be costly and time-consuming because of the large number of variables that need to be taken into account. The aim of this chapter is to investigate new alloys which are hardened either by γ' or TCP phases on the basis of a theoretical model which is capable of accounting for the simultaneous effects of several alloy additions.

13.2 Strengthening Mechanisms

13.2.1 Solid Solution Strengthening

Solid solution strengthening is known to be due to distortions of the parent lattice by the solute atoms. However, such effects can manifest themselves in different ways, as discussed below.

13.2.1.1 Size Misfit

Solid solution strengthening due to size misfit is produced by the difference Δa between the atomic radius a_0 of the solvent and a of the solute atom.(2) Typical solid solution strengthening elements found in nickel-based superalloys are aluminium, iron, titanium, chromium, cobalt and tungsten. The difference in atomic radius from that of nickel varies from +1% for cobalt to +13% for tungsten.(3) The influence of the solute atoms on solid solution strengthening is illustrated in

Fig. 13.1. A linear relation between flow stress and lattice parameter change is obeyed for any given solute element in nickel. It is interesting to note that for the same change in lattice parameter, the values for Ni-Cr alloys are higher than Ni-Mo and Ni-W alloys. It has been shown that the change in yield stress for various solutes in nickel depends directly on the position of the solute in the periodic table(4) so that for the same lattice strains, the hardening increases with the valence difference between solute and solvent (Fig. 13.2). Even though Mo and W are highly effective in increasing solid solution strengthening, the concentration of those elements is limited in superalloy applications. This is because they stabilise the intermetallic compound sigma phase.(3)

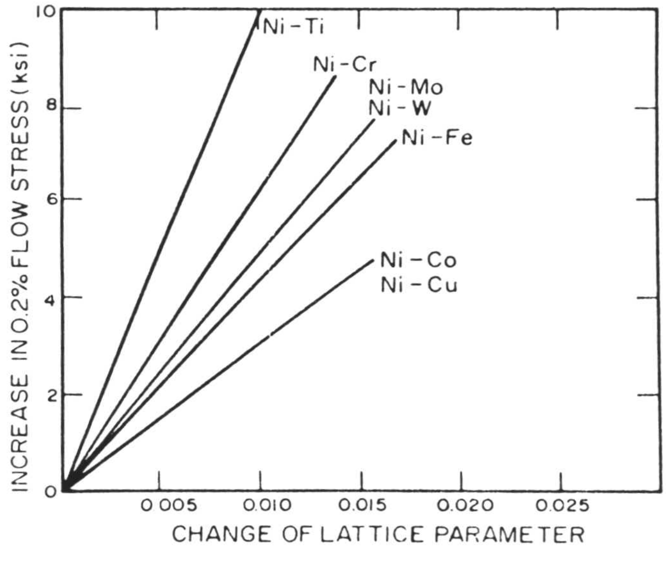

Fig. 13.1: Effect of solute atoms on solid solution strengthening.(3)

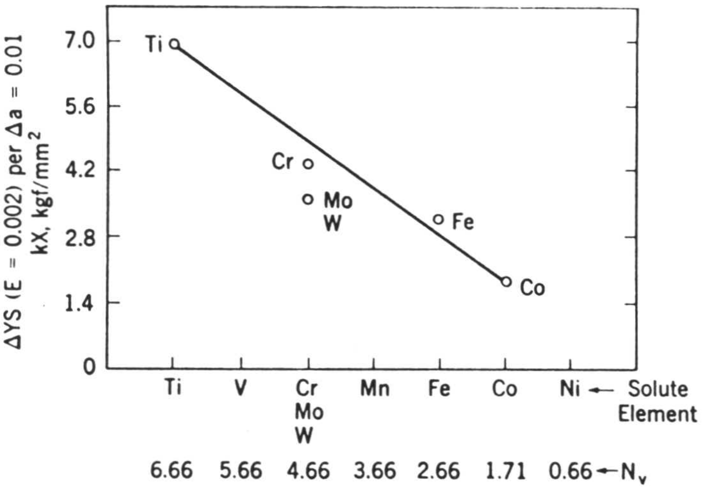

Fig. 13.2: Effect of valency difference of solute atoms on the flow stress in nickel.(3)

13.2.1.2 Modulus Misfit

It has been suggested that modulus differences between solute and solvent crystals lead to strengthening. This is based upon the argument that extra work is needed to force a dislocation through the hard or soft region in the matrix.(5)

13.2.1.3 Short-Range Order

Short-range order gives rise to an increase in flow stress since more energy is required for shear which involves the disruption of such order.(6) Even though strengthening due to short-range order and modulus misfit has been reported in Ni-based superalloys, the effect is negligible compared with the size misfit effect.(3)

13.2.2 Precipitation Hardening

A significant contribution to the strength of nickel-based alloys is provided by coherent stable precipitates γ'($Ni_3(Al,Ti)$). An increase in strength due to precipitation has been attributed to the following factors(7);

1) coherency strains;
2) differences in elastic moduli between particles and the matrix;
3) existence of order in the particles;
4) differences in stacking fault energies of particles and the matrix;
5) the need for energy to create additional particle-matrix interface.

The strengthening of alloys by misfitting coherent precipitates occurs due to the interaction between the stress fields of the precipitate and the dislocation. It has been well established that the relatively small coherency strains and low surface energies associated with coherent precipitates result in a uniform distribution of precipitates and high resistance to coarsening, leading to significant strengthening.(8)(9) The degree of coherency is determined by the mismatch along the matching planes at the precipitate-matrix interface. The fcc matrix and $L1_2$ γ' precipitates have similar atomic arrangements, and therefore form coherent interfaces on $\{1\ 1\ 1\}$ planes.[1] Partitioning of alloying elements between the γ and γ' is the best means of controlling the mismatch. For example, it has been shown that substitution of nickel by either iron, molybdenum or chromium results in a reduced mismatch.(10) However, Ti preferentially partitions into the γ', increases its lattice parameter, and therefore leads to a higher degree of mismatch.(3) This problem will be discussed later in conjunction with the computer model.

Modulus hardening occurs when the shear moduli of the matrix and precipitate phases differ. This is because strain energy of a dislocation is then different in the two phases. Hardening due to modulus mismatch has been reported to be a very weak strengthening mechanism.(6)

Strengthening due to order occurs when a matrix dislocation shears γ' and creates an antiphase boundary (APB) on the slip plane of the precipitate. The antiphase boundary energy per unit area on the slip plane represents the force per unit length opposing the motion of dislocation as it penetrates the γ'. This interaction gives rise to a significant increase in the strength. It has been demonstrated that the APB energy varies considerably as a function of alloy content.(3) For instance, chromium and titanium produce opposite effects, the former increasing the APB energy significantly.(3) It has been concluded that the APB energy should be increased to its greatest possible extent in any alloy design procedure.(6)

The motion of the dislocations can be impeded if the stacking fault energies of the precipitate and matrix phases are different. This is because the separation of the partial dislocations depend upon the phase in which dislocations are lying.

If a dislocation cuts into a precipitate, a new precipitate-matrix interface is created. The energy created is only about one tenth of the antiphase boundary energy, therefore the effect is rather small.(6)

---

[1] The unit cells of fcc Ni (a) and $L1_2$ type γ' precipitates (b) are shown below. The closed-packed (111) planes are stacked in the same sequence indicating good matching on these planes.

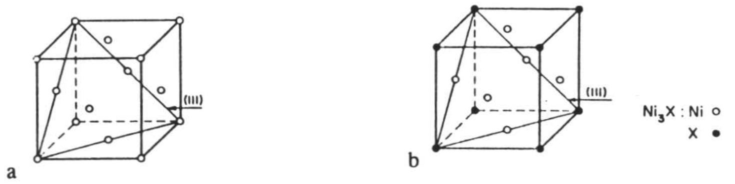

It is quite likely that more than one mechanism might operate simultaneously. However, it has been shown that coherency strains and the presence of order are the major contributors to strength hardening in nickel-based alloys.(3,6)

Besides the strengthening factors defined above, there is a significant influence of the volume fraction of γ' precipitates on the strength. An increase in the volume fraction of γ' up to 0.6 has been shown to enhance the strength considerably, associated with an increase in the resistance to dislocation movement (Fig. 13.3).(10) On the other hand, it has been demonstrated that high temperature strength decreases above a volume fraction of ≈ 0.6.(11) The decrease in the strength is probably associated with an increase of the total grain boundary area, which consequently leads to a higher degree of grain boundary sliding and low strength.

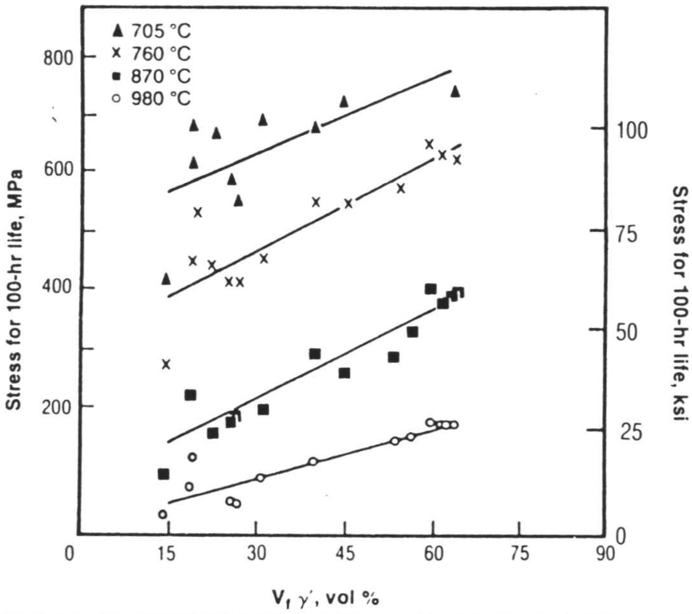

Fig. 13.3: Effect of the volume fraction of γ' precipitates on the strength of nickel-based superalloys.(10)

On the basis of the strengthening mechanisms; large size misfit, large modulus misfit, large short-range order, low stacking fault energy for the matrix phase, and high volume fraction ($\approx$ 0.6), coherent, fine with high antiphase boundary energy and low misfit, γ' precipitates are used to achieve better high-temperature strength.

13.3 Computer Model for Alloy Design

The procedure for the design of nickel-based superalloys for aircraft engines has been successfully used by Harada et al.(11), Yamazaki,(12) and Yamagata et al.(13) in the National Research Institute for Metals in Japan. A similar procedure has been adopted in this present work. A flow chart of the computer program used is given in Fig. 13.4.

The left column in this figure shows the steps which are discussed in detail below.

Concerning step 3: The partitioning ratio of an element (R_i) is defined as the ratio of the concentration of that element in the γ to that in the γ' which is in equilibrium with γ. The values used are given in Table 13.1.

Table 13.1: Partitioning ratios of alloying elements R_i (x_i^{γ} / $x_i^{\gamma'}$) when γ and γ' are in equilibrium.(11)

	Cr	Mo	Al	Ti	Co	W	Ta
R_i	7.37	3.99	0.24	0.19	2.65	1.76	0.20

Concerning step 4: For a given initial guess value of γ' volume fraction and equilibrium partitioning ratios of alloying elements, the γ' composition can be calculated using the mass-balance equations as follows;

$$x_i^T = x_i^{\gamma'} * V_{\gamma'} + x_i^{\gamma} * (1 - V_{\gamma'}) \qquad .....(1)$$

and

$$x_i^{\gamma} = x_i^{\gamma'} * R_i \qquad .....(2)$$

therefore;

$$x_i^{\gamma'} = x_i^T / (V_{\gamma'} + (1 - V_{\gamma'}) R_i) \qquad .....(3)$$

where x_i^T is the average concentration of ith element, R_i is the partitioning coefficient ($x_i^{\gamma}/x_i^{\gamma'}$) and $V_{\gamma'}$ is the mole fraction of γ' precipitates.

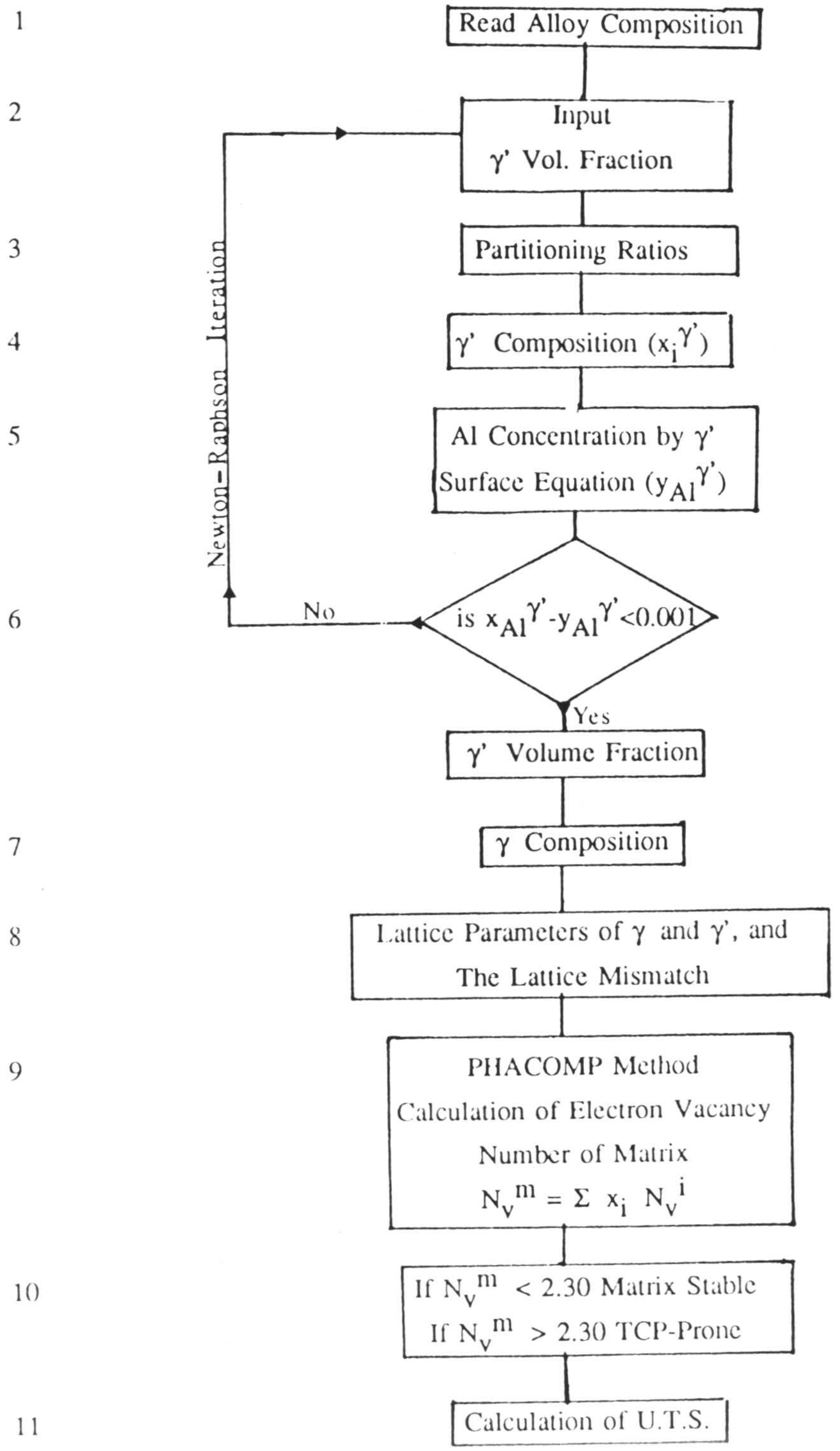

Fig. 13.4: The flow chart of the computer program used in the design of new Ni-based hardfacing alloys.

Concerning step 5: The γ' surface has been defined as a surface in a multicomponent phase diagram on which equilibrium compositions are connected to γ surface by tie lines when γ and γ' are in equilibrium (Fig. 13.5).(13) One hundred nickel-based superalloys have been analysed and the γ' surface is expressed by the Al concentration in γ' as a function of other alloying elements, excluding Ni, in γ' (Eq. 4).(11)

$$\%Al = 29.203 - 1.096x_{Cr}^{\gamma'} - 1.195x_{W}^{\gamma'} - 1.220x_{Ti}^{\gamma'} - 1.066x_{Ta}^{\gamma'} - 1.950x_{Mo}^{\gamma'} - 1.446x_{Nb}^{\gamma'} \quad (at\%) \qquad .....(4)$$

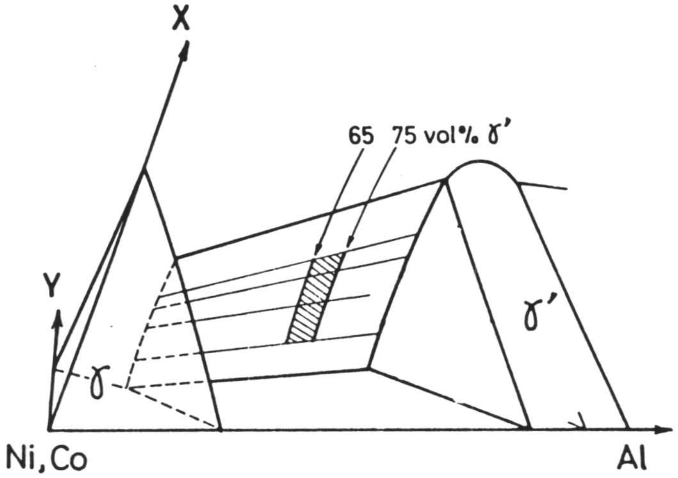

Fig. 13.5: Pseudo-quaternary phase diagram showing the γ and γ' surfaces. X and Y represent solid solution elements Cr, W, Mo, etc.(13)

Concerning step 6: The mole fraction of aluminium in γ' ($x_{Al}^{\gamma'}$) calculated using the partitioning coefficients is compared with that calculated by the surface equation ($y_{Al}^{\gamma'}$). If ($x_{Al}^{\gamma'} - y_{Al}^{\gamma'} < 0.001$) then the correct γ' volume fraction is taken to have been reached. If the difference is higher than 0.001, the initial guess value is modified using the Newton-Raphson iteration method. The solution being reached after n iterations. Fig. 13.6 shows a comparison between the observed volume fraction (using data in Table 13.2) against those predicted.

Table 13.2 Chemical compositions and corresponding volume fractions of gamma prime precipitates of nickel-based superalloys used for the comparison against those calculated volume fractions.

Composition (wt%)								
Ni	Cr	Mo	Al	Ti	Co	W	Fe	$V_{\gamma'}$
* 60.10	5.5	0.0	5.2	0.0	7.5	16.6	5.1	0.65
* 40.10	5.5	0.0	5.3	0.0	7.3	18.6	3.4	0.65
* 68.0	6.6	0.0	5.2	0.0	0.0	12.8	7.7	0.65
* 67.6	5.4	0.0	5.5	0.0	0.0	9.4	12.4	0.75
* 69.25	9.0	1.0	5.75	1.2	0.0	10.5	3.3	0.69
* 66.6	8.0	0.6	5.6	0.9	4.6	7.9	5.8	0.64
** 66.5	8.5	0.0	5.5	2.2	5.5	9.5	2.8	0.68
** 68.1	6.7	0.0	4.7	0.0	0.0	7.7	12.8	0.74
** 68.0	8.3	0.0	5.2	2.1	4.9	8.7	2.8	0.63
** 61.3	5.7	0.0	4.4	0.0	7.6	16.2	4.8	0.55
** 69.4	8.8	1.0	5.8	1.2	0.0	10.5	3.3	0.80
***54.5	15.0	0.0	2.6	4.5	13.4	10.0	0.0	0.511
***58.3	12.1	0.0	3.2	5.7	11.9	8.8	0.0	0.65
***58.8	12.8	0.0	3.7	3.9	9.5	8.7	2.6	0.65
***62.3	5.8	0.0	4.0	3.1	8.5	13.3	3.0	0.65
***63.1	4.8	0.0	4.5	3.5	7.9	12.9	3.3	0.75
***58.7	9.7	0.0	4.3	0.6	8.9	13.2	3.8	0.50
***59.8	8.0	0.0	5.2	0.7	8.2	12.6	4.5	0.65
***59.4	8.2	0.0	4.8	0.0	8.2	12.7	4.9	0.65
***59.8	4.8	0.0	5.0	0.8	7.3	18.7	2.7	0.65
***63.7	8.0	6.0	6.0	0.7	10.0	0.0	4.3	0.732
***60.1	8.3	0.6	5.5	1.0	10.0	10.0	3.0	0.614
***62.8	6.1	2.0	5.4	1.0	7.5	5.8	9.0	0.745

* From Ref. 13.

** From Ref. 14.

*** From Ref. 11.

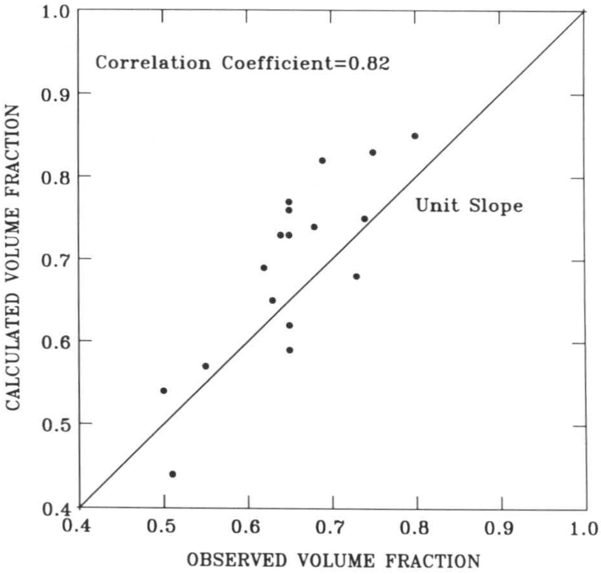

Fig. 13.6: Comparison between the observed volume fraction of γ' precipitates (data are given in Table 13.2) and those predicted.

Concerning step 7: The composition and the volume fraction of γ phase are calculated using the partitioning ratios given in Table 13.1.

Concerning step 8: A regression analysis has been carried out by Harada et al. analysing 100 different alloys to represent the effect of composition on the lattice parameters of γ and γ' phases.(14,15) The results of the regression analyses are given below.

$$a_{\gamma}=3.5240+4.35E-3\ x_{Mo}^{\gamma}+1.20E-3\ x_{Cr}^{\gamma}+1.85E-3\ x_{Al}^{\gamma}+3.40E-3\ x_{Ti}^{\gamma}+0.2E-3\ x_{Co}^{\gamma}+4.12E-3\ x_{W}^{\gamma}+6.3E-3\ x_{Ta}^{\gamma} \quad .....(5)$$

$$a_{\gamma'}=3.5208+4.35E-3\ x_{Mo}^{\gamma'}+1.20E-3\ x_{Cr}^{\gamma'}+1.85E-3\ x_{Al}^{\gamma'}+3.40E-3\ x_{Ti}^{\gamma'}+0.2E-3\ x_{Co}^{\gamma'}+4.12E-3\ x_{W}^{\gamma'}+6.3E-3\ x_{Ta}^{\gamma'} \quad .....(6)$$

where a_{γ} and $a_{\gamma'}$ are the lattice parameters of gamma and gamma prime phases and $x_i^{\gamma,\gamma'}$ represents the mole fraction of ith element in γ or γ'. The lattice mismatch is calculated using the lattice parameters as follows;

$$\text{Lattice mismatch (\%)} = [\ a_{\gamma'} - a_{\gamma})\ /\ a_{\gamma'}]\ *\ 100 \quad .....(7)$$

The results from equations 5 and 6 were tested against experimental data given in Table 13.3 and the agreement was found to be poor. Since the lattice parameters depend on the chemical composition multiple regression analysis was carried out to find out the correlation between the composition and the lattice mismatch. The regression analysis result (using the alloys given in Table 13.3) is represented by equation 8, and the comparison between the observed and calculated lattice misfit values is shown in Fig. 13.7.

$$\%\mathrm{Lattice\ Mismatch}\ (a_{\gamma'}-a_{\gamma}\ /\ a_{\gamma'}) * 100 = 1.216-0.00202{x_{Ni}}^{T} +0.003697{x_{Cr}}^{T}+0.1090{x_{Mo}}^{T}+0.07708{x_{Al}}^{T}-0.04055{x_{Ti}}^{T}-0.006479{x_{Co}}^{T} -0.03787{x_{W}}^{T}-0.003563{x_{Ta}}^{T} \qquad .....(8)$$

Table 13.3 Chemical composition and corresponding lattice mismatch (LM) $(a_{\gamma'}-a_{\gamma} / a_{\gamma'}) * 100$ values of the alloys used in the regression analysis.

	Composition (wt%)							
%LM	Ni	Cr	Mo	Al	Ti	Co	W	Ta
* 0.32	60.10	5.5	0.0	5.2	0.0	7.5	16.6	5.1
* 0.17	40.10	5.5	0.0	5.3	0.0	7.3	18.6	3.4
* 0.49	68.0	6.6	0.0	5.2	0.0	0.0	12.8	7.7
* 0.28	66.40	9.2	0.0	5.3	0.0	0.0	8.7	10.4
* 0.78	67.6	5.4	0.0	5.5	0.0	0.0	9.4	12.4
*-0.04	69.25	9.0	1.0	5.75	1.2	0.0	10.5	3.3
* 0.39	66.6	8.0	0.6	5.6	0.9	4.6	7.9	5.8
* 0.28	62.5	10.0	0.0	5.0	1.5	5.0	4.0	12.0
* 0.25	66.5	8.5	0.0	5.5	2.2	5.5	9.5	2.8
**0.35	68.1	6.7	0.0	4.7	0.0	0.0	7.7	12.8
**0.16	68.0	8.3	0.0	5.2	2.1	4.9	8.7	2.8
**0.08	61.3	5.7	0.0	4.4	0.0	7.6	16.2	4.8
**-0.56	69.4	8.8	1.0	5.8	1.2	0.0	10.5	3.3
**-0.04	69.25	9.0	1.0	5.75	1.2	0.0	10.5	3.3
**0.393	87.20	0.0	0.0	12.8	0.0	0.0	0.0	0.0
**0.5635	87.30	0.0	0.0	12.7	0.0	0.0	0.0	0.0
**0.521	87.81	0.0	0.0	12.19	0.0	0.0	0.0	0.0
**0.449	87.70	0.0	0.0	12.30	0.0	0.0	0.0	0.0
**0.056	75.90	18.7	0.0	5.4	0.0	0.0	0.0	0.0
**0.244	84.30	5.2	0.0	10.50	0.0	0.0	0.0	0.0
**0.398	79.3	9.9	0.0	10.8	0.0	0.0	0.0	0.0
**0.918	77.80	15.0	0.0	2.4	4.5	0.2	0.0	0.0
**0.779	76.70	15.1	1.0	2.5	4.5	0.2	0.0	0.0
**0.417	75.70	15.1	3.0	2.5	4.5	0.2	0.0	0.0
**0.724	73.80	21.9	0.0	1.90	2.4	0.0	0.0	0.0
**0.363	73.30	21.7	0.0	3.70	1.30	0.0	0.0	0.0
**0.028	73.00	20.6	0.0	6.3	0.0	0.0	0.0	0.0
**0.306	52.0	18.0	4.2	3.0	3.0	19.0	0.0	0.0
**0.640	71.0	21.0	0.0	2.8	2.8	0.5	0.0	0.0

* After Ref. 13.

** After Ref. 16.

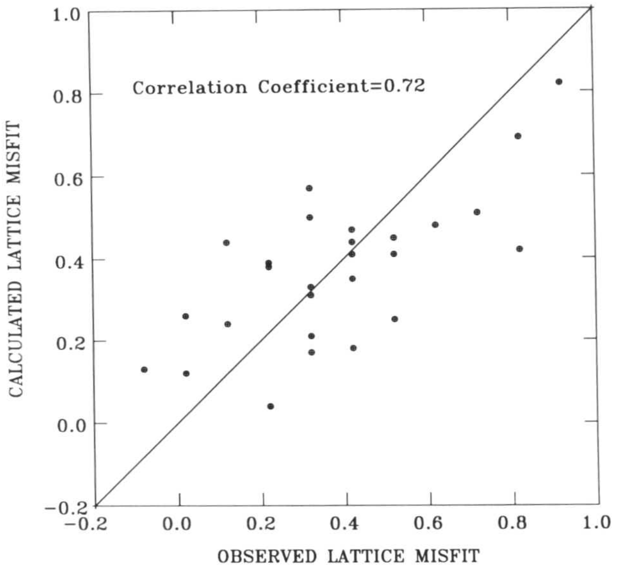

Fig. 13.7: Comparison between the observed lattice mismatch $(a_{\gamma'}-a_{\gamma} / a_{\gamma'})$ * 100 (data are given in Table 13.3) against those predicted using equation 8.

Concerning step 9: The phase computation method (PHACOMP) has been applied to predict the presence or absence of topologically-closed-packed (TCP) phases. As discussed in Chapter 9, this model suggests that TCP phases form after the critical value of electron vacany concentration (N_V^{crit}) of the matrix. The value of N_V^{crit} depends on the composition and the temperature. This value is taken to be 2.30 which is known to be a good assumption.(10) Above N_V^{crit}, the matrix is unstable and TCP phases may form.

Concerning step 11: Ultimate tensile strength (U.T.S) as a function of alloy composition (wt%) at different temperatures has been calculated using equations 9-13.

$$\mathrm{U.T.S}\ (20^{\circ}\mathrm{C}) = 461.9+12.91x_{Cr}^{T}+2.473x_{Co}^{T}+15.85x_{Mo}^{T}+9.621x_{W}^{T}+26.95x_{Ta}^{T}+34.44x_{Al}^{T}+32.51x_{Ti}^{T} \qquad .....(9)$$

$$\mathrm{U.T.S}\ (650^{\circ}\mathrm{C}) = 148.2+11.39x_{Cr}^{T}+4.088x_{Co}^{T}+14.82x_{Mo}^{T}+11.80x_{W}^{T}+29.21x_{Ta}^{T}+82.19x_{Al}^{T}+61.05x_{Ti}^{T} \qquad .....(10)$$

$$\mathrm{U.T.S}\ (760^{\circ}\mathrm{C}) = 96.52+12.16x_{Cr}^{T}+1.008x_{Co}^{T}+20.40x_{Mo}^{T}+15.19x_{W}^{T}+33.17x_{Ta}^{T}+88.68x_{Al}^{T}+58.92x_{Ti}^{T} \qquad .....(11)$$

$$\mathrm{U.T.S}\ (871^{\circ}\mathrm{C}) = 56.53+5.184x_{Cr}^{T}+2.559x_{Co}^{T}+23.87x_{Mo}^{T}+12.93x_{W}^{T}+28.21x_{Ta}^{T}+84.14x_{Al}^{T}+37.96x_{Ti}^{T} \qquad .....(12)$$

$$\mathrm{U.T.S}\ (982^{\circ}\mathrm{C}) = 37.23-3.992x_{Cr}^{T}-0.0091x_{Co}^{T}-0.55x_{Mo}^{T}+6.53x_{W}^{T}+20.05x_{Ta}^{T}+67.91x_{Al}^{T}+42.92x_{Ti}^{T} \qquad .....(13)$$

These equations were derived using multiple regression analysis from the data given in Table 13.4. The strengthening due to pure nickel was subtracted for each composition, and used as a regression constant. In this way, the contributions of the individual alloying elements to the strength of nickel-based hardfacing alloys could be evaluated. The strength of pure nickel as a function of temperature is taken from Table 13.5 and represented in Fig. 13.8. Fig. 13.9a-e show comparisons between the observed ultimate tensile strength against those predicted using Eqs. 9-13 at different temperatures. The correlation coefficients were found to be 0.84, 0.84, 0.83, 0.86, and 0.85 at 21, 650, 760, 871 and 982°C, respectively illustrating the good agreement between the observed and calculated strength values.

Table 13.4 Chemical composition and corresponding ultimate tensile strength (U.T.S.) values of cast nickel-based superalloys used in the multiple regression analyses.[17]

U.T.S. (MPa) (°C)					Composition (wt%)								
20	650	760	871	982	Ni	Cr	Mo	Co	W	Ta	Al	Ti	Fe
710	660	-	-	-	63.0	15.5	0.0	5.3	0.0	0.0	3.0	2.0	10.0
500	-	-	-	-	73.0	20.0	0.0	0.0	0.0	0.0	0.2	0.4	5.0
730	-	-	-	-	71.0	20.0	0.0	0.0	0.0	0.0	1.3	2.4	5.0
700	560	490	260	-	53.0	20.0	17.5	0.0	0.0	0.0	1.3	2.4	5.0
1040	1080	1195	1215	595	74.0	0.0	0.0	18.0	0.0	0.0	8.0	0.0	0.0
975	1015	950	793	550	64.0	8.0	10.0	6.0	0.0	4.0	6.0	1.0	0.0
1185	-	1295	1020	-	66.0	8.0	4.6	0.6	7.9	5.8	5.6	0.9	0.0
1015	1110	1070	885	565	60.0	10.0	15.0	3.0	0.0	0.0	5.5	4.7	0.0
835	895	915	750	525	67.0	9.5	10.0	2.5	0.0	0.0	5.5	4.6	0.0
1035	1085	965	770	455	61.0	16.0	8.5	1.7	2.6	1.7	3.4	3.4	0.0
1170	-	1130	840	-	61.0	12.4	9.0	1.9	3.8	3.9	3.1	4.5	0.0
1050	985	915	640	325	48.0	22.5	19.0	0.0	2.0	1.4	1.9	3.7	0.0
1170	1090	990	840	-	61.0	12.4	9.0	1.9	3.8	3.9	3.1	4.5	0.0
730	835	910	885	545	71.0	5.7	0.0	2.0	11.0	3.0	6.3	0.0	0.0
930	950	930	840	550	60.0	9.0	10.0	0.0	12.0	0.0	5.0	2.0	0.0
1000	1020	1080	915	655	60.0	9.0	10.0	0.0	12.0	0.0	5.0	2.0	0.0
965	1035	1035	860	550	60.0	9.0	10.0	2.5	10.0	1.5	5.5	1.5	0.0
1035	1070	1035	825	550	61.0	9.0	10.0	0.0	10.0	2.5	5.5	1.5	0.0
1000	1000	895	655	380	74.0	12.0	0.0	4.5	0.0	0.0	5.9	0.6	0.0
1070	1070	1070	860	550	59.0	8.5	10.0	2.0	8.0	3.8	4.8	2.5	0.0
1105	1070	1070	860	565	63.0	9.0	10.0	2.5	10.0	1.5	5.5	1.5	0.0
1035	1070	1035	825	540	59.0	9.0	10.0	0.0	12.5	0.0	5.0	2.0	0.0
1085	-	1135	950	-	60.0	8.3	10.0	0.7	10.0	3.0	5.5	1.0	0.0
965	1050	1035	825	550	60.0	8.2	10.0	0.0	10.0	3.0	5.5	1.0	0.0
1140	1140	1130	995	685	63.0	10.0	5.0	0.0	4.0	12.0	5.0	1.5	0.0
1020	1050	940	-	-	58.0	14.6	15.0	4.2	0.0	0.0	4.3	3.3	0.0
1030	1030	995	705	-	60.0	14.0	9.5	4.0	4.0	0.0	3.0	5.0	0.0
1020	910	875	-	-	51.0	15.0	22.0	4.5	0.0	0.0	4.4	2.4	0.0
1060	1100	1090	840	-	58.0	11.0	14.5	6.5	1.5	0.0	5.4	2.5	0.0
1050	1140	1095	870	595	61.0	6.1	7.5	2.0	5.8	9.0	5.4	1.0	0.0
930	885	855	650	130	52.0	18.0	19.0	4.2	0.0	0.0	3.0	3.0	0.0
945	950	945	710	-	64.0	16.0	5.0	1.5	6.0	0.0	4.5	2.0	0.0
1075	1110	1055	730	415	55.0	18.0	15.0	3.0	15.0	0.0	2.5	5.0	0.0
895	830	830	775	485	72.0	0.0	0.0	0.0	20.0	0.0	6.5	0.0	0.0
1040	1080	1195	1215	595	74.0	0.0	0.0	18.0	0.0	0.0	8.0	0.0	0.0

Table 13.5: Ultimate Tensile Strength (U.T.S) of annealed pure nickel as a function of temperature.(18)

Temperature (°C)	U.T.S. (MPa)
21	461
93	458
149	459
204	458
260	465
315	456
343	427
371	361
426	303
482	255
538	217
593	182
649	148
760	96
815	84
871	56
982	37
1093	24

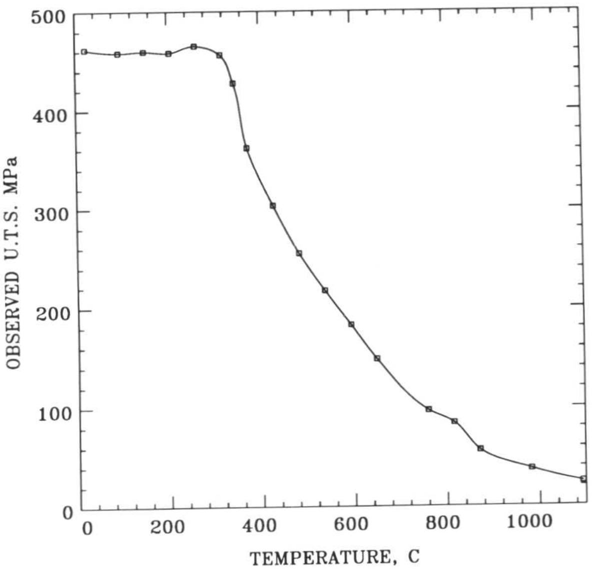

Fig. 13.8: Strength of pure nickel as a function of temperature. Data from Ref. 18.

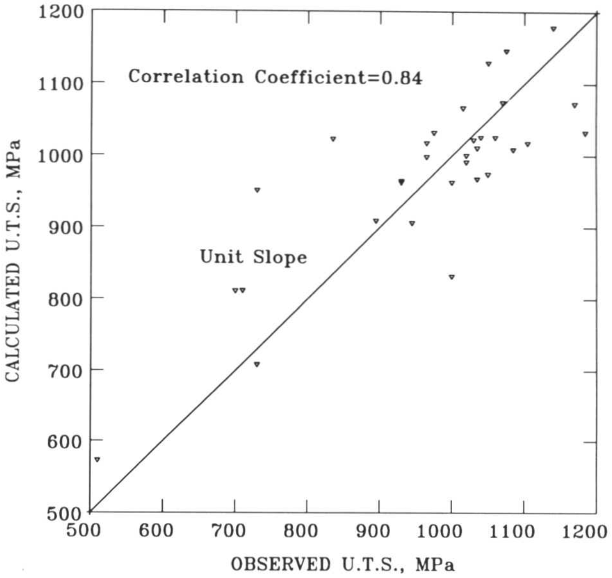

a

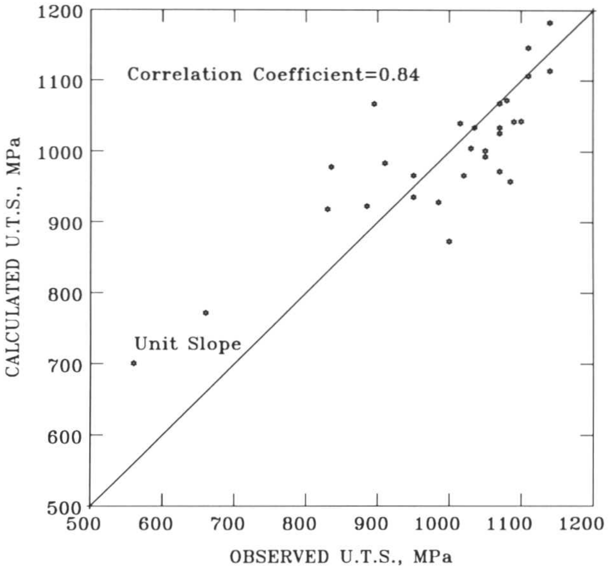

b

Fig. 13.9: Comparison between the observed ultimate tensile strength (U.T.S) against values calculated using equations 9-13, at

a) room temperature,

b) 650^{0}C

c) 760^{0}C

d) 871^{0}C

e) 982^{0}C.

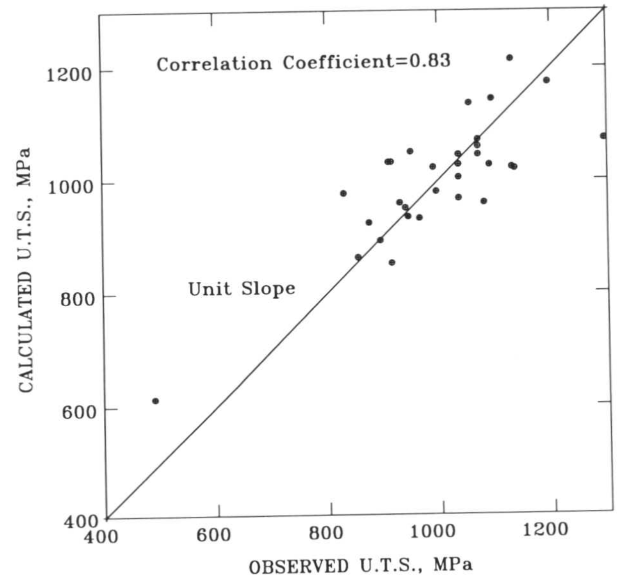

c

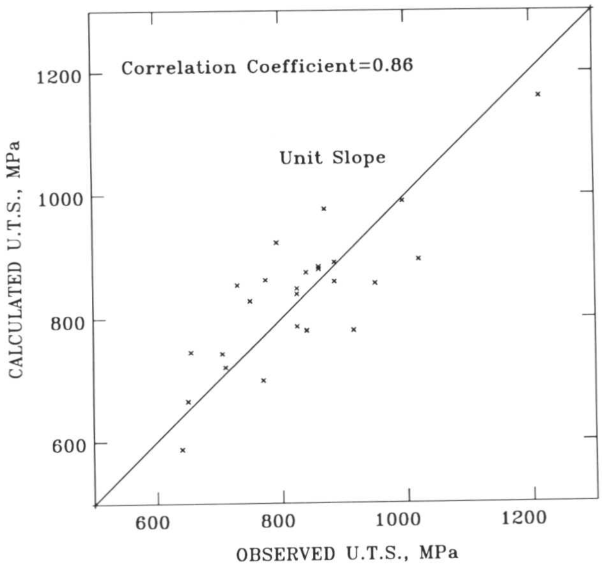

d

Fig. 13.9 Comparison between the observed ultimate tensile strength (U.T.S) against values calculated using equations 11 and 12, at c) 760°C; d) 871°C respectively.

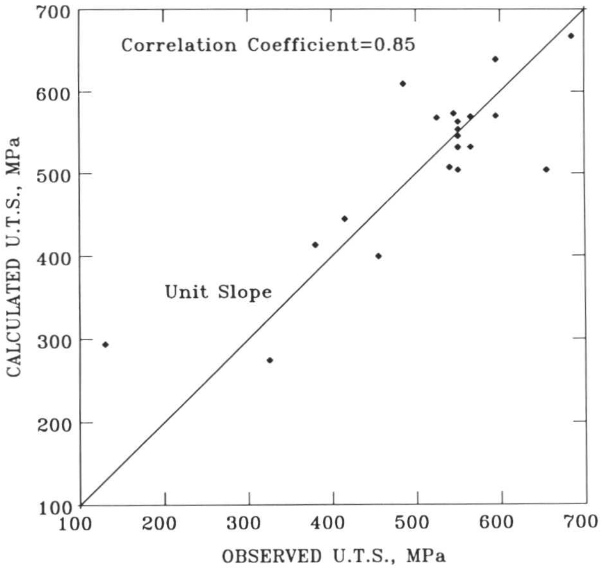

e

Fig. 13.9 Comparison between the observed ultimate tensile strength (U.T.S) against values calculated using equation 13 at e) 982^{0}C.

13.4 Experimental Alloys

Hastelloy type nickel-chromium-molybdenum hardfacing alloys with the nominal composition Ni-15Cr-16Mo (wt%) are currently used for high temperature applications (e.g. hot shear blades, valve seats) where, in addition to the high temperature strength, oxidation and corrosion resistance are also important. These alloys are nominally single phase and include other alloying additions such as tungsten and iron. The composition of Hastelloy C-276 which was deposited by the manual metal arc welding process is given in Table 13.6. The weld was deposited in three layers so that the top layer could be examined in an essentially undiluted condition. Electrodes 4mm in diameter were used, the welding conditions being 160A, 23V A.C., with a welding speed of about 0.004m/s and an interpass temperature of about 350^{o}C. The influence of Al, Ti, and Al+Ti on the microstructure was studied on experimental casts ($\approx$ 65g) made from high purity elements in an argon arc furnace with a water cooled copper mould. The chemical compositions of the alloys studied are presented in Table 13.6. A number of 3mm diameter rods were machined from the weld deposit, parallel to the welding direction. For heat treatment experiments, specimens and 3mm diameter discs were cut from the casts and were sealed off in a quartz tube, after flushing three times with argon, pumping down to a pressure of 10^{-6} torr and backfilling with a partial pressure of argon. The alloys were first analysed theoretically using the computer program and the results are presented in Table 13.7, including the ultimate tensile strength values as a function of temperature. The electron vacancy concentration of the matrix phase (N_v^{m}) is also calculated and compared with the critical electron vacancy concentration (N_v^{crit} = 2.30). The ratio of (N_v^{m}) / (N_v^{crit}) is a measure of the degree of the stability of the matrix phase. It can be seen that (N_v^{m}) for all the alloys studied is higher than 2.30 indicating that topologically-closed-packed phases are likely to form. The Ti containing alloy was found to be the most metastable due to the high electron vacancy number of Ti.

Table 13.6 Chemical compositions of the alloys studied (wt%).

	Ni	Cr	Mo	Al	Ti	Fe	W	Si	Mn	C
C-217	62.6	14.94	15.48	-	-	2.25	3.78	0.26	0.58	0.068
Cast-1	57.8	15.2	16.9	0.3	8.1	-	-	0.18	0.20	0.012
Cast-2	63.1	15.4	15.7	5.2	0.02	-	-	0.13	0.20	0.008
Cast-3	62.0	15.4	16.0	3.3	2.4	-	-	0.14	0.20	0.004
Cast-4	74.0	10.0	10.0	3.3	2.4	-	-	-	-	- *

* Nominal composition.

Table 13.7 Calculated volume fraction of gamma prime precipitates ($V_{\gamma'}$), Ultimate Tensile Strength (UTS) values (MPa) as a function of temperature (^{o}C), and (N_v^{m}) / (N_v^{crit}) ratio of the experimental alloys. In this table UTS20, UTS650 represent the ultimate tensile strength at 20, and $650^{o}C$ respectively and vice versa. (N_v^{crit}) ratio is taken to be 2.30 as discussed in the text.

	$(V_{\gamma'})$	UTS20	UTS650	UTS760	UTS871	UTS982	(N_v^{m}) / (N_v^{crit})
C-217	-	936	593	650	552	-	0.89
Cast-1	0.5	1199	1091	1124	871	335	1.22
Cast-2	0.43	1106	978	1024	887	294	1.13
Cast-3	0.55	1089	984	1066	949	321	1.25
Cast-4	0.48	951	850	878	736	336	0.83

13.5 Results and Discussion

The position of the alloy C-276 in isothermal sections of Ni-Cr-Mo system, at 1250^{o}C, and 850^{o}C(19) ignoring the effect of other alloying elements is shown in Fig. 13.10. It can be seen that the alloy is in the single phase region of fcc nickel at both temperatures. Transmission electron microscopy, however, revealed that the alloy is a mixture of fcc matrix and intermetallic compound P phase, preferentially nucleated on γ/γ grain boundaries (Fig. 13.11a). The P phase has a orthorhombic crystal structure with a = 9.07 A, b = 16.98 A, and c = 4.75 A.(19) This phase has been observed extensively in Hastelloy nickel-based alloys.(3,19-21) The composition range of the P phase was determined to be Cr: 9.1 to 18.4, Ni: 31.2 to 34.5, and Mo: 50.4 to 58.2 pct, with a nominal chemical composition $CrNi_2Mo_2$.(19) It has been demonstrated that alloy additions such as iron and tungsten in Hastelloy C-276 can displace the gamma solvus line so that the alloy can be in P+γ region as the alloy solidifies from 1250 to 850^{o}C. The P+γ field at 850^{o}C is displaced to a region of higher Cr content as the μ+γ field appears at lower Cr and higher Mo concentrations. This is consistent with the experimental results which showed that the alloy contains μ phase in the fcc matrix at 850^{o}C after 20 days (Fig. 13.11b). The μ phase has a hexagonal crystal structure (a = 4.76 A, and c = 25.72 A), having a rhombohedral symmetry(19) with a high fault density (Fig. 13.11c).

The as-received microstructure of titanium containing alloy (Cast-1) was found to be significantly different, consisting of a high volume fraction of sigma phase in the fcc matrix (Fig. 13.12a). The formation of sigma phase is not unexpected since titanium has a high electron vacancy number (6.6),(3) and therefore promotes the formation of topologically-closed-packed phases. Some γ' particles are clear as illustrated in the bright field transmission electron micrograph in Fig. 13.12b. The sigma phase was found to be stable at 750^{o}C after 100 hours as illustrated in Fig. 13.12c.

An addition of aluminium resulted in the formation of a high volume of γ' precipitates (Fig. 13.13a). Even though some sigma phase was occasionally observed (Fig. 13.13b) the quantity of it was found to be small. After 100 hours at 750^{o}C the γ' precipitates were found to be surrounded by a high density of interfacial dislocations resulting from the lattice misfit (Fig. 13.13c). The sigma phase was observed to be stable as seen from Fig. 13.13c.

A high volume fraction of γ' precipitates was also observed in an Al+Ti containing alloy in the as-received condition (Fig. 13.14a). After ageing 100 hours at 750^{o}C, the microstructure was found to be in a four-phase equilibrium, as sigma phase (large particles), Ni_3Ti plates, γ' precipitates, and γ matrix.

These results have shown that the addition of Al, Ti, and Al+Ti to an alloy with nominal composition Ni-16Cr-16Mo (wt%) results in a microstructure which is a mixture of gamma prime precipitates and intermetallic compounds in an fcc matrix. Therefore, molybdenum and chromium additions were decreased to 10wt% in alloy Cast-2 in order to obtain a microstructure consisting of only gamma and gamma prime phases. The electron vacancy concentration of the matrix phase of the new alloy was found to be ≈ 1.8 which is well below the (N_V^{crit}) suggesting that intermetallic compounds are unlikely to form. Transmission electron microscopy analysis results were found to be consistent with the above discussion, showing that the alloy contains very fine gamma prime precipitates with volume fraction ≈ 0.6 in the gamma matrix (Fig. 13.15). Although this result is very encouraging, the high-temperature microstructural stability of this alloy has yet to be determined.

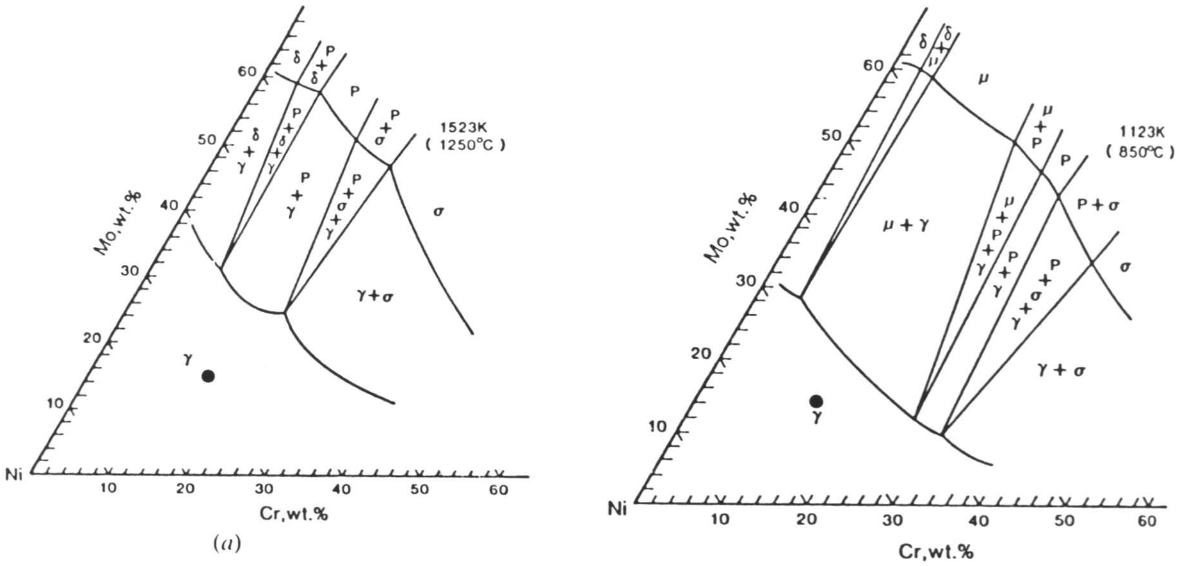

(*a*)

(*b*)

Fig. 13.10: Isothermal sections of Ni-Cr-Mo system at a) 1250°C; b) 850°C. The point indicated on the diagrams shows the position of the alloy C-217.(19)

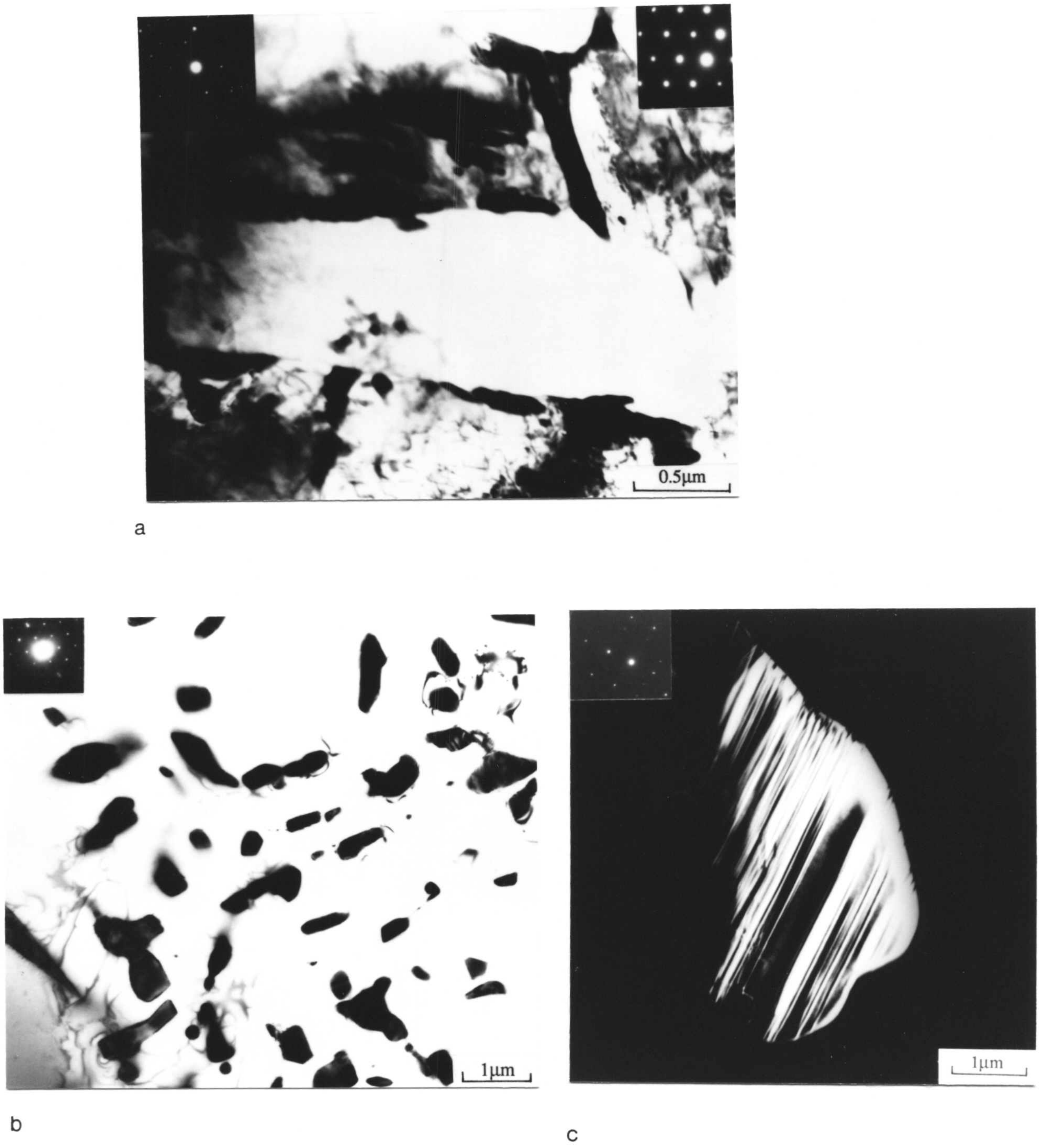

a

b

c

Fig. 13.11: a) Bright field transmission electron micrograph of alloy C-217 after solidification, showing fcc gamma grain and P phase which is preferentially nucleated on γ/γ grain boundaries. Selected area diffraction pattern from the P phase is given in the left-hand corner; the zone axis of the pattern is $<320>_P$. Selected area diffraction pattern from the matrix phase is given in the right-hand corner illustrating $<111>_{fcc}$ pattern; b) bright field transmission electron micrograph after 20 days at 850^{o}C showing two phase equilibrium; fcc matrix and μ phase, indicating that P phase is not stable at this temperature; c) dark field transmission electron micrograph of the μ phase using (132) reflection showing extensive faults; the zone axes of the pattern is <134>.

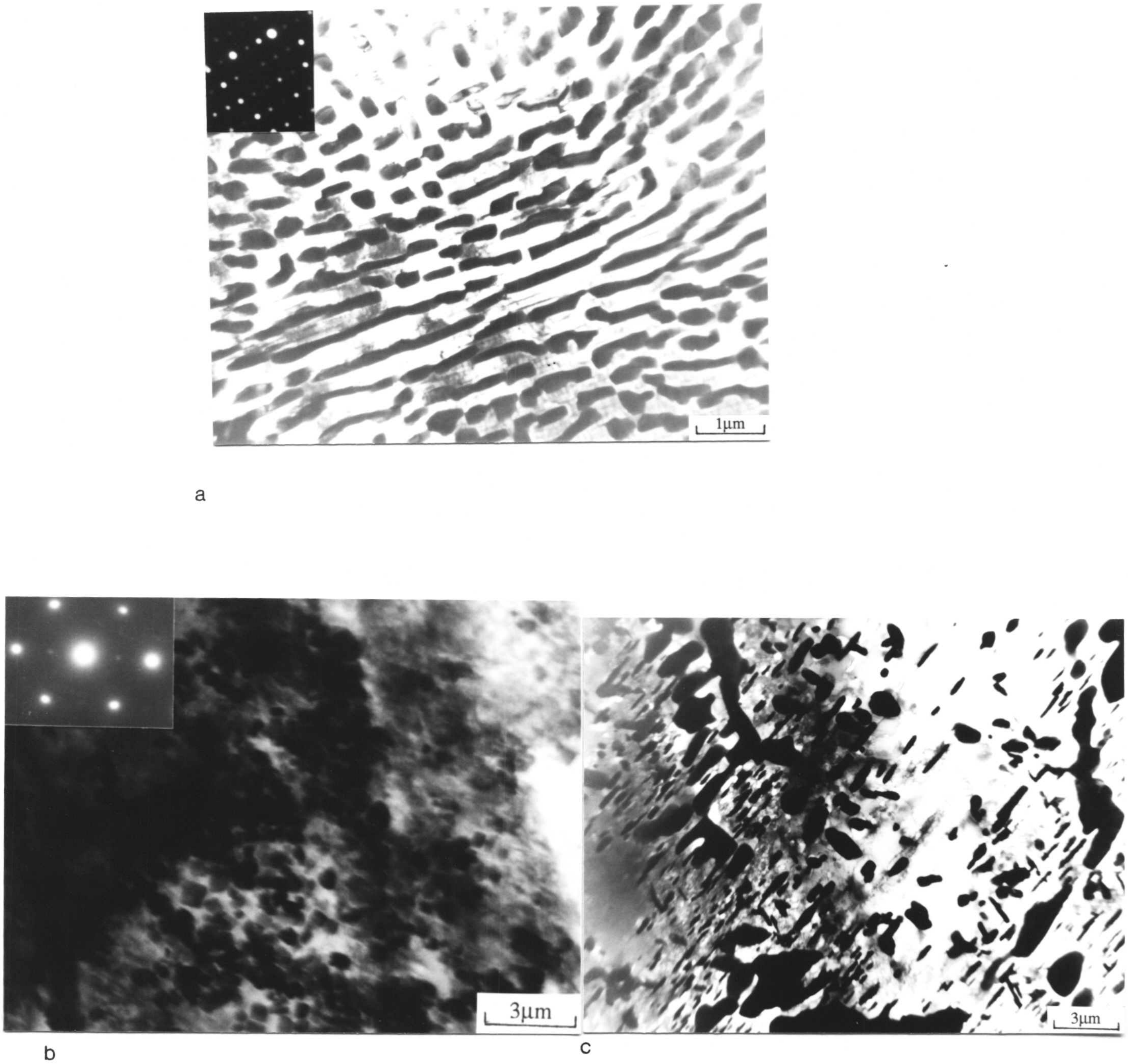

Fig. 13.12: Bright field transmission electron micrographs of alloy Cast-1 (Ni-15.2Cr-16.9Mo-0.3Al-8.1Ti wt%), after solidification showing a) a high volume fraction of sigma phase (selected area diffraction pattern from the sigma phase is inserted; the zone axis of the pattern is $<111>_{\text{sigma}}$; b) γ' precipitates; selected area diffraction pattern from the γ/γ' region is inserted; the zone axes of the pattern is $<011>_{\text{fcc}}$; c) after 100 hours at 750°C, illustrating that the sigma phase is stable and in equilibrium with γ and γ' phases.

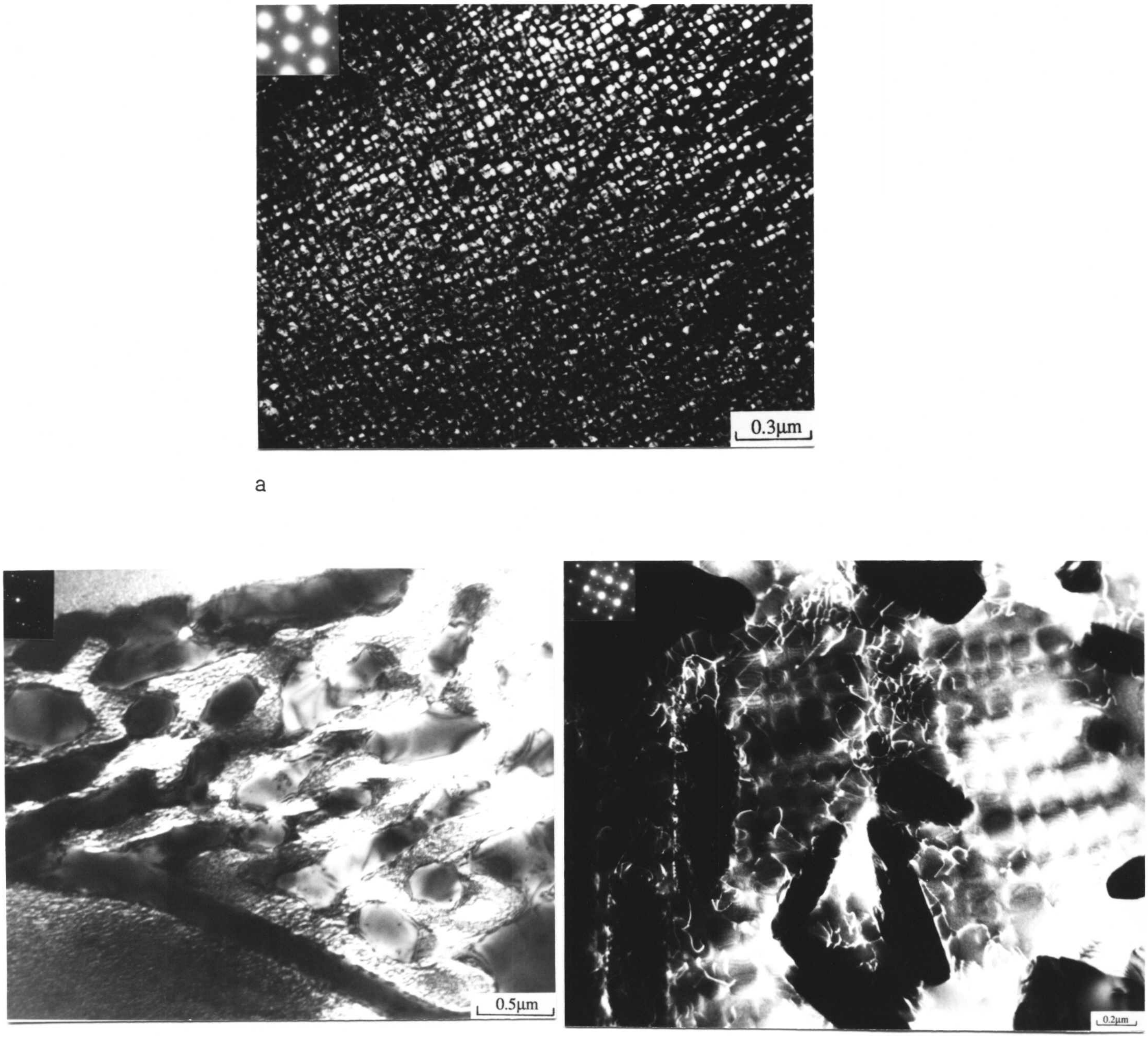

a

b

c

Fig. 13.13: a) Dark field transmission electron micrograph of alloy Cast-2 (Ni-15.4Cr-15.7Mo-5.2Al-0.02Ti wt%) using $(110)_{\gamma'}$ reflection showing a high volume fraction of gamma prime precipitates ($\approx$ 0.6); and b) sigma phases; the zone axis of the inserted diffraction pattern is $<201>_{sigma}$; c) dark field transmission electron micrograph using $(110)_{\gamma'}$ superlattice reflection showing a high density of interfacial dislocations resulting from the γ/γ' lattice mismatch, and some sigma phase (black particles).

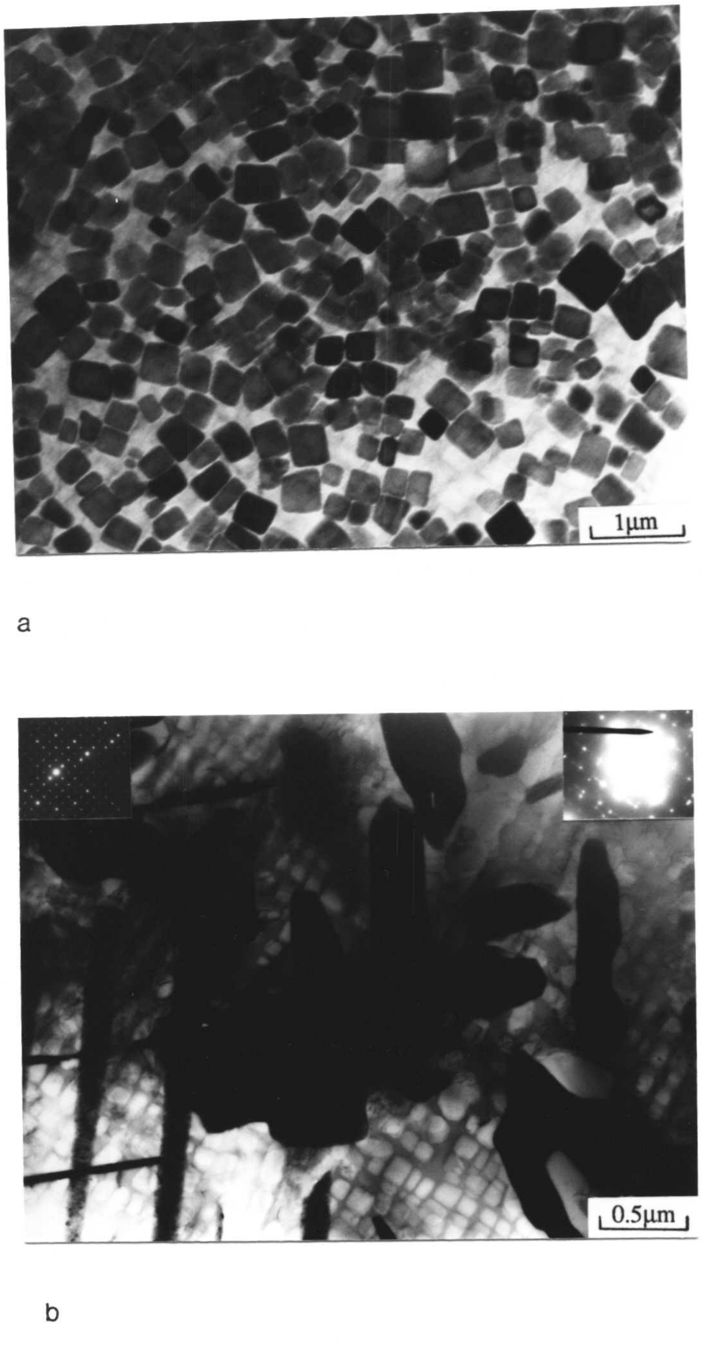

Fig. 13.14: Bright field transmission electron micrographs of alloy Cast-3 (Ni-15.4Cr-16.0Mo-3.3Al-2.4Ti wt%) a) as received microstructure consisting of γ' precipitates; b) after 100 hours at 750°C illustrating four phase equilibrium; sigma phase (large black particles) selected area diffraction pattern inserted in left-hand corner; the zone axis is $<110>_{sigma}$, Ni_3Ti plates (inserted diffraction pattern is taken from these particles; zone axis of the pattern is $<100>_{Ni_3Ti}$) arrow points out $(231)_{Ni_3Ti}$ spot, γ' precipitates and the gamma matrix.

13.6 Conclusions

An attempt has been made to improve the high temperature properties of nickel-based hardfacing alloys. The alloys which are currently used possess poor high temperature wear resistance due to a lack of second phase strengthening. Although the alloys used are nominally single phase fcc nickel at high temperatures, an addition of alloying elements such as tungsten and iron can alter the isothermal sections of Ni-Cr-Mo system so that alloys are located in a two-phase region of the Ni-Cr-Mo equilibrium phase diagram consisting of fcc gamma matrix and one of a variety of intermetallic compounds (e.g. mu phase at 850^oC). These compounds are brittle and therefore detrimental to mechanical properties at nickel-based superalloy applications. On the other hand, their wear resistance is expected to be better compared to an alloy which is in a single phase region γ primarily through their high hardness. One difficulty is that the ranges of the stability of those intermetallic compounds are not very well known, and experimental studies here showed that an addition of alloying elements tend to have a significant influence on Ni-Cr-Mo isothermal sections.

In order to develop new nickel-based hardfacing alloys a theoretical computer program which is capable of accounting for the simultaneous effects of several alloy additions was used. The main purpose was to provide precipitation strengthening via γ' by the addition of Al, and Ti. Multiple regression analysis was therefore carried out using the available data in the literature to rationalise the effect of chemical composition on the high temperature strength, and the lattice mismatch between the γ/γ' phases. The program is also capable of calculating the volume fraction of γ' precipitates, and electron vacancy concentration of the matrix phase, which gives an indication of whether topologically-closed-packed phases will be stable. The addition of Al, Ti, and Al+Ti to an alloy with nominal composition Ni-16Cr-16Mo (wt%) giving $\approx$ 0.6 volume fraction of γ' precipitates was first experimentally studied. These additions resulted in the formation of a high volume fraction of intermetallic compounds whose morphology, volume fraction, and the range of the stability was found to vary significantly with the composition. The actual effects of these intermetallic compounds on alloy mechanical properties is a suitable subject for future research.

Since chromium, and molybdenum are intermetallic compound forming elements, their compositions were reduced to 10wt% in an alloy with nominal composition Ni-10Cr-10Mo-3.3Al-2.4Ti. Theoretical calculations showed that the electron vacancy concentration of the matrix phase is well below the critical concentration indicating that the matrix should be stable. The calculated volume fraction of gamma prime precipitates was found to be $\approx$ 0.5 which provides significant hardening compared to alloy C-217 (Table 13.6). Transmission electron microscopy results showed that the as-received microstructure consists of very fine γ' precipitates in the γ matrix.

This alloy can be replaced by C-217 for applications such as valve seats and hot shear blades. However, its high temperature microstructural stability is yet to be determined. Since these alloys are produced by a variety of welding processes, the microstructure of the weld deposits need to be established.

13.7 References

1) Metals Handbook, 9th edn, 1983, vol. 6, ASM, USA, pp. 771-803.
2) N. F. MOTT, and F. R. N. NABARRO: Rep. Conf. Strength Sol. Phys. Soc., 1984, 1-9.
3) CHESTER T. SIMS, NORMAN S. STOLOFF, and WILLIAM C. HAGEL (Eds.) "Superalloys", 1987, A Wiley-Interscience Publication, John Wiley & Sons, New York, pp. 61-96.
4) R. M. N. PELLOOX, and N. J. GRANT: Trans. Met. Soc. AIME, 1960, **218**, 232.
5) R. L. FLEISCHER: Acta Metall., 1963, **11**, 203.
6) A. J. ARDELL: Metall. Trans. A, 1985, **16A**, 2131.
7) A. K. JENA, and M. C. CHATURVEDI: J. of Mat. Sci., 1984, **19**, 3121.
8) N. M. GUNVANT, and J. E. BRIDGE, JR: Metall. Trans. A, 1971, **2A**, 95.
9) G. N. MANIAR, J. E. BRIDGE, JR., H. M. JAMES, and G. B. HEYDT: Metall. Trans. A, 1970, **1A**, 31.
10) "High Temperature Materials in Gas Turbines", P. R. SAHM, and M. O. SPEIDEL, (Eds.), 1974, Elsevier Scientific Publishing Company, New York, pp. 115-147.
11) H. HARADA, M. YAMAZAKI, K. KOIZUMI, N. SAKUMA, N. FURUYA, and H. KAMIYA: in Proc. Conf. 'High Temperature Alloys for Gas Turbines', 1982, Belgium, 4-6 October, pp. 721-735.
12) M. YAMAZAKI: in Proc. Conf. 'High Temperature Alloys for Gas Turbines and Other Applications 1986', 6-9 October, Belgium, pp. 945-954.
13) T. YAMAGATA, H. HARADA, S. NAKAZAWA, M. YAMAZAKI, and Y. G. NAKAGAWA: in Proc. Conf. 'Superalloys 1984', 7-11 October, 1984, Pennsylvania, U.S.A, pp. 157-166.
14) H. HARADA: Special Report, 1985, National Research Institute for Metals, Tokyo, Japan.
15) H. HARADA: Private communication.
16) E. NEMBACH, and G. NEIIE: Progress in Materials Science, 1986, **29**, pp. 177-319
17) "High Temperature, High Strength Nickel Base Alloys", Special Report, International Nickel Japan Limited, Tokyo, Japan.
18) S. J. ROSENDERG: "Nickel and Its Alloys", U.S. Department of Commerce, National Bureau of Standards, 1968, Monograph 106, p. 38.
19) M. RAGHAVAN, R. R. MUELLER, G. A. VAUGHN, and S. FLOREEN: Metall. Trans. A, 1984, **15A**, 783.
20) M. RAGHAVAN, B. J. BERKOWITZ, and J. C. SCANLON: Metall. Trans. A, 1986, **13A**, 979.
21) M. J. CIESLAK, T.J. HEADLEY, and A. D. ROMIG: Metall. Trans. A, 1986, **17A**, 2035.

14. CONCLUSIONS AND SUGGESTIONS FOR FURTHER WORK

Some progress has been made in designing methods for the control of microstructure and in understanding the relationship between abrasive wear resistance and microstructure in iron, cobalt, and nickel-based hardfacing alloys.

It has been demonstrated using a theoretical model, based on three dimensional heat flow equations that the welding variables (e.g. the arc voltage, arc current, travel speed) have a significant influence on the geometry, dilution and microstructure of hardfacing deposits; in particular the cooling rate is dependent upon the the variables. The influence of the heat input on the volume fraction of phases in iron-based hardfacing alloys has been calculated. The results showed that the volume fraction of primary carbides decreases drastically with increased heat input. Similar calculations need to be carried out in order to understand the influence of each welding variable and combinations of them on the microstructure. The method used here does not take into account some important factors such as convective flow and magnetic forces in the weld pool.

The microstructure and abrasive wear resistance of high chromium and high carbon containing iron-based hardfacing deposits has been investigated. In the undiluted state it consists of primary M_7C_3 carbides and a eutectic mixture of austenite and more eutectic M_7C_3. The metastable austenitic matrix was found to contain ≈16Cr (wt%) and was expected to transform to a mixture of ferrite and M_7C_3 below ≈750°C. The ferrite that forms has a significantly lower chromium content. The kinetics of this transformation have been studied at 800, 750 and 700°C. At the initial stage of transformation, $M_{23}C_6$ type carbides were observed to form in the austenitic phase. $M_{23}C_6$ is not expected from the Fe-Cr-C equilibrium phase diagram. The nucleation of these carbides could be associated with a good match at the interface between austenite and $M_{23}C_6$ resulting in a low interfacial energy and hence a smaller barrier to nucleation. Eventually the austenite was found to transform to ferrite, the final microstructure after 24 hours being ferrite and M_7C_3 carbides. The chromium concentration in the ferrite was found to be ≈3 wt%, well below the amount needed for good oxidation and corrosion resistance. Therefore, an attempt has been made to modify the microstructure using thermodynamic modelling of Fe-Cr-C-X (where X refers to a fourth alloying addition) systems, when γ is in equilibrium with M_7C_3. The calculations suggested that additions of Mn and Ni increase the Cr concentration of the austenitic matrix. On the other hand, silicon was found to have an opposite effect. The volume fraction of M_7C_3 carbides was found to decrease drastically with additions of Mn and Ni and to increase with Si. Experimental alloys confirmed the calculations. Si also significantly changed the morphology of the primary M_7C_3 carbides, the particles tending to become more equiaxed with increased silicon concentration. This may be because the orientation dependence of liquid/M_7C_3 interfacial energy is reduced by Si. The abrasive wear resistance of the Si containing alloy was found to be better than that of the Mn and Ni containing alloys, primarily due to the morphological effect. The morphological changes may improve impact abrasion resistance and need further investigation. New welding electrodes and deposits have already been prepared in which the effect of dilution on the first two layers of the usual manual metal arc deposits will also need to be studied.

The effect of Nb and Ti on the microstructure and abrasive wear resistance was studied in weld deposits and in cast alloys. MC (NbC, TiC) type carbides precipitate first and later the liquid transforms to austenite and M_7C_3 carbides via a eutectic reaction. Microanalysis showed that Nb and Ti are used mainly in the formation of MC carbides with only limited amounts being found in the matrix phase. High-stress abrasion test experiments showed that the width of the scratch grooves was narrower in the primary hard MC carbides than in the eutectic region indicating an improved abrasion resistance.

The effects of Mo on the microstructure of Fe-based hardfacing deposits have been examined. The optical microscopy and microanalysis revealed the high molybdenum containing dark etching regions along the austenite dendrite boundaries, which form due to segregation during solidification.

Vanadium and tungsten in Fe-Cr-C-Nb alloys were found to partition preferentially into the M_7C_3 carbides and did not form any tungsten or vanadium-rich carbides.

The microstructure and abrasive wear properties of cobalt-based Stellite 6 type hardfacing alloys deposited by manual metal arc (MMA) welding, tungsten inert gas (TIG) welding, and laser cladding were investigated in order to establish the relationship between microstructure and wear properties. The degree of dilution was greatest with MMA, and found to decrease in the order MMA, TIG, laser cladding. Subsequently, the strength of the microstructure decreased on the reverse order of processes. Microanalysis experiments indicated that the laser cladding process involves less turbulence within the fusion zone as evident from the nonuniform distribution of alloying elements. The TIG deposits however, were observed to have the most uniform chemical composition. The microstructure of the undiluted top layer of each deposit was found to contain primary fcc cobalt-rich dendrites and interdendritic M_7C_3 carbides. The matrix phase was found to contain a high density of stacking faults oriented in a particular variant probably due to the presence of residual stresses in each deposit. The microanalysis experiments indicated that tungsten preferentially partitions into the M_7C_3 carbides. This property needs to be controlled, since a high concentration of tungsten is needed in the matrix phase for improved solid solution strengthening. Among the other alloying elements, Fe and Ni were found to partition strongly into the fcc matrix phase. It is well known that these alloying elements stabilise the fcc phase so that this result may be of use in controlling the microstructure. Silicon hardly dissolves in the carbide phase as is the case in iron-based alloys. It is likely that an increased Si level may alter the volume fraction and morphology of carbides and consequently the abrasive wear resistance. This also needs further investigation.

The abrasive wear properties of these deposits were examined using two different abrasives; SiC and alumina. With alumina abrasives, the MMA samples were found to show the poorest wear resistance because of their coarser microstructure and lower starting hardness. The TIG deposits showed the highest initial wear resistance because of a high matrix stacking fault energy. Strain hardening was noted in laser clad samples due to the relatively low stacking fault energy of the matrix phase resulting in easy fcc-hcp strain-induced phase transformation. With relatively hard SiC abrasives the wear rate in all samples were found to be almost the same, although laser clad deposits showed slightly lower wear rate, probably due to their strain hardening capacity. The overall weight loss with SiC abrasives for each deposit was found to be higher than that of alumina abrasives. This is a reflection of the relatively large size of SiC abrasives. This work was carried out on samples prepared using what are believed to be typical process parameters. There are a number of variables which can be adjusted to modify the microstructure. Therefore, the influence of those variables on the microstructure and abrasive wear resistance needs to be studied. It is also important to study the effect of chemical composition on abrasive wear resistance. For instance, abrasion properties of a high Fe and high Ni containing alloy may be compared with an alloy without any addition of these elements. In the former alloy the fcc matrix may be stabilised and in the latter case the fcc-hcp transformation should become easier. This gives a chance to understand the influence of the matrix phase and strain hardening on abrasive wear resistance. The wear test experiments need to be carried out at high temperatures, simulating the service conditions.

The high temperature microstructural stability of the Co-based deposits was investigated. $M_{23}C_6$ carbides were observed to nucleate on stacking faults or dislocations. With increasing time, two different carbide morphologies were observed; long continuous carbides which are preferentially oriented in the matrix, and discrete irregular particles with no favoured orientation. Elastic interactions between adjacent particles are believed to be responsible for the aligenment of the carbides during coarsening. The presence of the residual stresses may also play an important role for the alignment. The effect of the residual stresses can be eliminated by annealing the samples before heat treatments so that the significance of elastic interactions on carbide growth can be better understood. The interdendritic M_7C_3 carbides were found to transform to $M_{23}C_6$ carbides. Direct evidence of the transformation has not been obtained and this may be very interesting subject for future work.

Nickel-based alloys in current use, possess poor high temperature wear resistance due to the lack of second phase strengthening. In order to modify the microstructure a model which is capable of accounting for the simultaneous effects of several alloy additions was developed and used. Precipitation hardening was provided experimentally by the addition of Al, Ti or Al+Ti resulting in a formation of γ' precipitates. The stability of the matrix phase was controlled so that probability of the formation of topologically-closed-packed phases was low. The effect of chemical composition on the high temperature strength was also analysed. A Ni-10Cr-10Mo-

3.3Al-2.4Ti (wt%) cast alloy was designed with a microstructure having $\gamma+\gamma'$ mixture. The alloy was found to contain very fine γ' precipitates in the γ matrix, consistent with the calculations. The calculated high temperature strength of this alloy is also much better than the currently used alloys. However, high temperature microstructural stability and the effect of dilution on the weld deposits need to be studied.

APPENDIX 1: THERMODYNAMIC PROGRAM TO CALCULATE EQUILIBRIUM COMPOSITIONS

```
FTVSCLR PROGRAM=%H% DATA=.DATA NAG
C THIS PROGRAM CALCULATES THE AUSTENITE/M7C3, FERRITE/M7C3
C EQUILIBRIUM IN FE-CR-C, Fe-Cr-C-Si, Fe-Cr-C-Mn, Fe-Cr-C-Ni
C QUATERNARY SYSTEM, ON THE BASIS OF
C MINIMAZATION OF THE TOTAL GIBBS FREE ENERGY OF THE SYSTEM.
C THE SUBROUTINE "GROWTH" CALCULATES THE COARSENING RATE
C OF M7C3 CARBIDES EITHER IN AUSTENITE OR FERRITE.
IMPLICIT REAL*8 (A-H,O-Z)
DOUBLE PRECISION F
INTEGER IBOUND, IFAIL, J, LIW, LW, N, NOUT
DOUBLE PRECISION BL(4), BU(4), W(54), X(4)
DOUBLE PRECISION TFE,TCE,TC,R,T,TSI,TCR
DOUBLE PRECISION TTOP,TNI1,TMN1,TSI1,TC1
DOUBLE PRECISION V1,V2,V3,V4,VSI,TFE1,TCR1
DOUBLE PRECISION PART,DIF1,DIFCO,PR1,PR2,PR3,RADIUS
DOUBLE PRECISION ESI,ALPHA,TMN,TNI,VX
DOUBLE PRECISION CMN,CNI,EMN,ENI
INTEGER IW(6),TIME
COMMON/PACAK/TFE,TCR,TSI,TMN,TNI
COMMON/ZARZA/R,T
COMMON/TARTA/ESI,ALPHA,A3
COMMON/EXTR/J
COMMON/PIRE/EMN,ENI
READ (5,*) J
READ (5,*) TFE1,TCR1,TTOP
IF (J .EQ. 1) THEN
TNI=TTOP
TNI1=TTOP
ELSE IF (J .EQ. 2) THEN
TMN=TTOP
TMN1=TTOP
ELSE IF (J .EQ. 3) THEN
TSI=TTOP
TSI1=TTOP
ENDIF
IF (J .EQ. 1) THEN
```

```
TC1=1.0D0-TCR1-TFE1-TNI1
ELSE IF (J .EQ. 2) THEN
TC1=1.0D0-TCR1-TFE1-TMN1
ELSE IF (J .EQ. 3) THEN
TC1=1.0D0-TCR1-TFE1-TSI1
ENDIF
V1=TFE1/55.85
V2=TCR1/52.0
IF (J .EQ. 1) THEN
VX=TNI/58.09
ELSE IF (J .EQ. 2) THEN
VX=TMN/55.0
ELSE IF (J .EQ. 3) THEN
VX=TSI/28.09
ENDIF
V3=TC1/12.01
V4=V1+V2+V3+VX
TFE=V1/V4
TCR=V2/V4
TMN=VX/V4
TNI=VX/V4
TSI=VX/V4 &SA 7 SEP 88 16.20
TC=V3/V4
TFE=TFE/(1.0D0-TC)
TCR=TCR/(1.0D0-TC)
TNI=TNI/(1.0D0-TC)
TMN=TMN/(1.0D0-TC)
TSI=TSI/(1.0D0-TC)
TC=TC/(1.0D0-TC)
WRITE(6,*) TCR,TC
T=12.73D2
R=1.987D0*4.182D0
DATA NOUT /6/
X(1)=0.71D0
X(2)=0.032D-1
X(3)=0.25
X(4)=0.71D0
WRITE (6,*) X(1),X(2),X(3),X(4)
N = 4
```

```
IBOUND = 0
BL(1) =0.40D0
BU(1)=0.8D0
BL(2)=0.02D0
BU(2)=0.09D0
BL(3)=0.20D0
BU(3)=0.30D0
BL(4)=0.55D0
BU(4)=0.80D0
LIW = 6
LW = 54
IFAIL = 1
CALL E04JAF(N, IBOUND, BL, BU, X, F, IW, LIW, W, LW, IFAIL)
C SINCE IFAIL WAS SET TO 1 BEFORE ENTERING E04JAF, IT IS
C ESSENTIAL TO TEST WHETHER IFAIL IS NON-ZERO ON EXIT
IF (IFAIL.NE.0) WRITE (NOUT,99998) IFAIL
IF (IFAIL.EQ.1) GO TO 20
WRITE (6,*) ' ISOTHERMAL TEMPERATURE IS (KELVIN): ', T
WRITE (6,*) ' WEIGHT PERCENT OF TOTAL FE IN THE ALLOY ', TFE1
WRITE (6,*) ' WEIGHT PERCENT OF TOTAL CR IN THE ALLOY ', TCR1
IF (J .EQ. 1) GOTO 66
IF (J .EQ. 2) GOTO 67
IF (J .EQ. 3) GOTO 68
66 WRITE (6,*) ' WEIGHT PERCENT OF TOTAL NI IN THE ALLOY ', TNI1
GOTO 69
67 WRITE (6,*) ' WEIGHT PERCENT OF TOTAL MN IN THE ALLOY ', TMN1
GOTO 69
68 WRITE (6,*) ' WEIGHT PERCENT OF TOTAL SI IN THE ALLOY ', TSI1
69 CONTINUE
WRITE (6,*) ' WEIGHT PERCENT OF TOTAL C IN THE ALLOY ', TC1
CALL STAR
CALL STAR
WRITE (6,*) ' MINIMUM GIBBS FREE ENRGY OF THE SYSTEM IS ', F
CALL STAR
IF (J .EQ. 1) THEN
GOTO 323
ELSE IF (J .EQ. 2) THEN
GOTO 324
ELSE IF (J .EQ. 3) THEN
```

```
GOTO 325
ENDIF &SA 7 SEP 88 16.20
323 WRITE (6,*) ' MOLE FRACTION OF NI IN AUSTENITE: ', ENI
GOTO 327
324 WRITE (6,*) ' MOLE FRACTION OF MN IN AUSTENITE: ', EMN
GOTO 327
325 WRITE (6,*) ' MOLE FRACTION OF SI IN AUSTENITE: ', ESI
327 CONTINUE
A3=(TCR-(X(4)*(1.0D0-ALPHA)))/ALPHA
WRITE (6,*) ' MOLE FRACTION OF CR IN AUSTENITE: ', A3
WRITE (6,*) ' MOLE FRACTION OF C IN AUSTENITE: ', X(2)
WRITE (6,*) ' MOLE FRACTION OF FE IN M7C3: ', X(3)
WRITE (6,*) ' MOLE FRACTION OF CR IN M7C3: ', X(4)
WRITE (6,*) ' VOLUME FRACTION OF AUSTENITE IS ', ALPHA
20 STOP
C END OF E04JAF EXAMPLE MAIN PROGRAM
99998 FORMAT (///16H ERROR EXIT TYPE, I3, 22H - SEE ROUTINE DOCUMEN,
* 1HT)
END
SUBROUTINE FUNCT1(N, XC, FC)
C ROUTINE EVALUATES THE OBJECTIVE FUNCTION
IMPLICIT DOUBLE PRECISION (L)
IMPLICIT DOUBLE PRECISION (A)
IMPLICIT DOUBLE PRECISION (E)
IMPLICIT DOUBLE PRECISION (C)
DOUBLE PRECISION FC
DOUBLE PRECISION XC(N)
DOUBLE PRECISION X1,X2,X3,X4
DOUBLE PRECISION AC,ACR,ALPHA
DOUBLE PRECISION TFE,TCR,R,T
DOUBLE PRECISION ESI,EMN,ENI,CMN,CNI
DOUBLE PRECISION TMN,TNI,TSI
COMMON/PACAK/TFE,TCR,TSI,TMN,TNI
COMMON/ZARZA/R,T
COMMON/TARTA/ESI,ALPHA,A3
COMMON/EXTR/J
COMMON/PIRE/EMN,ENI
INTEGER N
X1=XC(1)
```

```
154 X2=XC(2)
155 X3=XC(3)
156 X4=XC(4)
157 C
158 C
159 C CALCULATION OF THE FUNCTION
160 C ALPHA MOL AUSTENITE
161 C DEFINING MN, AND NI MOL FRACTIONS IN AUSTENITE AND M7C3
162 C CMN,CNI IN M7C3, EMN, ENI IN AUSTENITE
163 C
164 ALPHA=(TFE-X3)/(X1-X3)
165 A3=(TCR-(X4*(1.0D0-ALPHA)))/ALPHA
166 CMN=(1.0D0-(X3*0.7+X4*0.7+0.3))/0.7
167 EMN=(TMN-(CMN*(1.0D0-ALPHA)))/ALPHA
168 CNI=0.1D-3
169 ENI=(TNI-(CNI*(1.0D0-ALPHA)))/ALPHA
170 A1=SLFE(T)
171 A2=X1*A1
172 A4=SLCR(T)
173 A5=A3*A4
174 IF (J .EQ. 1) GOTO 121 &SA 7 SEP 88 16.20
175 IF (J .EQ. 2) GOTO 122 233 C EXCESS GIBBS FREE ENERGY DUE TO NI
176 IF (J .EQ. 3) GOTO 123 234 C
177 121 E1=SLNI(T) 235 130 AN1=-14.600D3
178 E2=ENI*E1 236 AN2=ANI*X2
179 GOTO 125 237 AN3=-14.600D3
180 122 E1=SLMN(T) 238 AN4=(1.0D0-X2)*AN3
181 E2=EMN*E1 239 AN5=AN2+AN4
182 GOTO 125 240 ATOP=X1*ENI*AN5
183 123 ESI=TSI/ALPHA 241 GOTO 135
184 E1=SLSI(T) 242 C
185 E2=ESI*E1 243 C
186 125 CONTINUE 244 C EXCESS GIBBS FREE ENERGY DUE TO MN
187 C GIBBS FREE ENERGY FOR THE FORMATION OF FCR CARBIDE 245 C
188 A6=GFF(T) 246 131 AMN1=9.230D3-(1.0D1*T)
189 A7=X2*A6 247 AMN2=AMN1*X2
190 A8=X1*DLOG(X1) 248 AMN3=7.30D2-(1.0D1*T)
191 A9=A3*DLOG(A3) 249 AMN4=(1.0D0-X2)*AMN3
192 A10=X2*DLOG(X2) 250 AMN5=AMN2+AMN4
```

```
    193 IF (J .EQ. 1) THEN 251 ATOP=X1*EMN*AMN5
    194 E3=ENI*DLOG(ENI) 252 GOTO 135
    195 ELSE IF (J .EQ. 2) THEN 253 C
    196 E3=EMN*DLOG(EMN) 254 C EXCESS GIBBS FREE ENERGY DUE TO SI
    197 ELSE IF (J .EQ. 3) THEN 255 C
    198 E3=ESI*DLOG(ESI) 256 132 ASI1=(-10.8280D4*X2)+(1.0D0-X2)*(-10.8280D4)
    199 ENDIF 257 ATOP=ASI1*X1*ESI
    200 A11=(1.0D0-X2)*DLOG(1.0D0-X2) 258 C
    201 A12=A8+A9+A10+A11+E3 259 135 CONTINUE
    202 A13=R*T*A12 260 AEX1=A21+ATOP
    203 A14=DGCRA(T) 261 C
    204 A15=A14*A3*X2 262 A22=LCVF(T)
    205 IF (J .EQ. 1) THEN 263 A23=X1*A22
    206 E4=46.000D3 264 A24=LCVCR(T)
    207 E5=E4*ENI*X2 265 A25=A3*A24
    208 ELSE IF (J .EQ. 2) THEN 266 IF (J .EQ. 1) THEN
    209 E4=-48.500D3 267 AF1=LCVNI(T)
    210 E5=E4*EMN*X2 268 AF2=AF1*ENI
    211 ELSE IF (J .EQ. 3) THEN 269 ELSE IF (J .EQ. 2) THEN
    212 E4=DGSIA(T) 270 AF1=LCVMN(T)
    213 E5=E4*ESI*X2 271 AF2=AF1*EMN
    214 ENDIF 272 ELSE IF (J .EQ. 3) THEN
    215 A16=LFCRC(T) 273 AF1=LCVSI(T)
    216 A17=A16*X2 274 AF2=AF1*ESI
    217 275 ENDIF
    218 A18=LFCRV(T) 276 A26=A23+A25+AF2
    219 A19=(1.0D0-X2)*A18 277 A27=X2*(1.0D0-X2)*A26
    220 A20=A17+A19 278 C
    221 A21=X1*A3*A20 279 A28=A2+A5+A7+A13+A15+AEX1+E2+E5+A27
    222 C 280 C ALPHA MOL AUSTENITE
    223 C EXCESS GIBBS FREE ENERGIES DUE TO ADDITION OF FOURTH ELEMENT
281 GMAUS=ALPHA*A28
    224 C 282 C
    225 IF (J .EQ. 1) THEN 283 C (1-ALPHA) MOL M7C3 CALCULATION
    226 GOTO 130 284 C
    227 ELSE IF (J .EQ. 2) THEN 285 A30=GFECA(T)
    228 GOTO 131 286 A31=X3*A30
    229 ELSE IF (J .EQ. 3) THEN 287 A32=GCRCA(T)
    230 GOTO 132 288 A33=X4*A32
```

```
231 ENDIF 289 IF (J .EQ. 1) THEN
232 C 290 A42=GNICA(T) &SA 7 SEP 88 16.20
291 A43=CNI*A42 349 LFCRC=P3
292 ELSE IF (J .EQ. 2) THEN 350 RETURN
293 A42=GMNCA(T) 351 END
294 A43=A42*CMN 352 C
295 ENDIF 353 DOUBLE PRECISION FUNCTION LFCRV(T)
296 A34=X3*DLOG(X3) 354 DOUBLE PRECISION T,P
297 A35=X4*DLOG(X4) 355 P1=13.110D3-(31.82D0*T)
298 IF (J .EQ. 1) THEN 356 P2=2.7481D0*T*DLOG(T)
299 A45=CNI*DLOG(CNI) 357 LFCRV=P1+P2
300 ELSE IF (J .EQ. 2) THEN 358 RETURN
301 A45=CMN*DLOG(CMN) 359 END
302 ENDIF 360 C
303 A36=R*T*(A34+A35+A45) 361 DOUBLE PRECISION FUNCTION LCVF(T)
304 A37=7.5D2*X3*X4 362 DOUBLE PRECISION T
305 A38=A31+A33+A43+A36+A37 363 LCVF=-21.058D3-(11.581D0*T)
306 C (1-ALPHA) MOL GIBBS FREE ENERGY OF M7C3   364 RETURN
307 GMM7C3=(1.0D0-ALPHA)*A38 365 END
308 C TOTAL GIBBS FREE ENERGY OF THE SYSTEM 366 C
309 TGFES=GMAUS+GMM7C3 367 DOUBLE PRECISION FUNCTION LCVCR(T)
310 FC=TGFES 368 DOUBLE PRECISION T
311 RETURN 369 LCVCR=-21.058D3-(11.581D0*T)
312 END 370 RETURN
313 C 371 END
314 C 372 C
315 C LATTICE STABILITY VALUES 373 DOUBLE PRECISION FUNCTION GFECA(T)
316 C 374 DOUBLE PRECISION T
317 DOUBLE PRECISION FUNCTION SLFE(T) 375 GFECA=16.730D3-(12.42*T)
318 DOUBLE PRECISION T,BY1,BY2,BY3 376 RETURN
319 BY1=5.23502D3-(9.4006*T) 377 END
320 BY2=0.52949D-2*(T**2.0D0) 378 C
321 BY3=-0.92215D-6*(T**3.0D0) 379
322 SLFE=BY1+BY2+BY3 380 DOUBLE PRECISION FUNCTION GCRCA(T)
323 RETURN 381 DOUBLE PRECISION T
324 END 382 GCRCA=-16.000D3-(7.62D0*T)
325 DOUBLE PRECISION FUNCTION SLCR(T) 383 RETURN
326 DOUBLE PRECISION T 384 END
327 SLCR=10.460D3+(0.6276D0*T) 385 C
```

```
328 RETURN 386 DOUBLE PRECISION FUNCTION SLSI(T)
329 END 387 DOUBLE PRECISION T
330 DOUBLE PRECISION FUNCTION GFF(T) 388 SLSI=-64.818D3+(35.543*T)
331 DOUBLE PRECISION T 389 RETURN
332 GFF=67.208D3-(7.640D0*T) 390 END
333 RETURN 391 C
334 END 392 DOUBLE PRECISION FUNCTION DGSIA(T)
335 DOUBLE PRECISION FUNCTION DGCRA(T) 393 DOUBLE PRECISION T
336 DOUBLE PRECISION T 394 DGSIA=12.3000D4
337 DGCRA=-25.1160D4+(1.18D2*T) 395 RETURN
338 RETURN 396 END
339 END 397 SUBROUTINE STAR
340 C 398 WRITE (6,*) ' ******************************************* '
341 C CALCULATION OF INTERACTION PARAMETERS 399 RETURN
342 C 400 END
343 DOUBLE PRECISION FUNCTION LFCRC(T) 401 C
344 DOUBLE PRECISION T 402 C
345 DOUBLE PRECISION P 403 DOUBLE PRECISION FUNCTION LCVSI(T)
346 P1=13.110D3-(31.82D0*T) 404 DOUBLE PRECISION T
347 P2=2.7481D0*T*DLOG(T) 405 LCVSI=-21.058D3-(11.581D0*T)
348 P3=P1+P2 406 RETURN &SA 7 SEP 88 16.20
407 END 465 GMNCA=-54.827D3+(5.579D0*T)
408 SUBROUTINE GROWTH (X) 466 RETURN
409 DOUBLE PRECISION PART,DIF1,DIFCO,PR1,PR2,PR3,RADIUS 467 END
410 DOUBLE PRECISION R,T 468
411 DOUBLE PRECISION X(4) 469 %
412 DOUBLE PRECISION P21,P22,P23
413 COMMON/ZARZA/R,T
414 RO=1.0D-12
415 PART=X(4)/X(1)
416 DIFCO=1.8D0*DEXP(-(97.000D3*4.182D0)/(R*T))
417 DO 1111 TIME=1, 1000000, 1000
418 PR1=0.7D0*8.0D1*5.8D-6*DIFCO
419 P21=6.3D1*R*T
420 P22=(1.0D0-PART)**2.0D0
421 P23=1.0-X(1)
422 PR2=P21*P22*P23
423 PR3=(PR1/PR2)*TIME
424 PR4=PR3+(RO**3.0)
```

```
RADIUS=PR4**(1.0/3.0)
1111 CONTINUE
RETURN
END
C
DOUBLE PRECISION FUNCTION SLNI(T)
DOUBLE PRECISION T
SLNI=-5.650D3-(3.35D0*T)
RETURN
END
C
DOUBLE PRECISION FUNCTION SLMN(T)
DOUBLE PRECISION T
SLMN=-1.800D3+(1.276*T)
RETURN
END
C
DOUBLE PRECISION FUNCTION LCVNI(T)
DOUBLE PRECISION T
LCVNI=-21.058D3-(11.581D0*T)
RETURN
END
C
DOUBLE PRECISION FUNCTION LCVMN(T)
DOUBLE PRECISION T
LCVMN=-21.058D3-(11.581D0*T)
RETURN
END
C
DOUBLE PRECISION FUNCTION GNICA(T)
DOUBLE PRECISION T
DOUBLE PRECISION GN1,GN2,GN3
GN1=-3.550D3+(4.568D0*T)
GN2=3.050D-3*(T**2.0D0)
GN3=-7.480D-7*(T**3.0D0)
GNICA=GN1+GN2+GN3
RETURN
END
DOUBLE PRECISION FUNCTION GMNCA(T)
```

```
DOUBLE PRECISION T
GMNCA=-54.827D3+(5.579D0*T)
RETURN
END %
```

APPENDIX 2: THERMODYNAMIC DATA

The following thermodynamic parameters (J/mol) have been used for the calculation of the γ/M_7C_3 equilibrium in Fe-Cr-C-M (M = Mn, Ni, and Si) system.

$^oG_C^\gamma - {}^oG_C^\alpha = -65563 + 23.815\ T$(1)

$^oG_{Fe}^\gamma - {}^oG_{Fe}^\alpha = 6108.64 + 3.4618\ T - 0.747E\text{-}2\ T^2 + 0.5125E\text{-}5\ T^3$ (700 - 1100 K)(2)

$^oG_{Fe}^\gamma - {}^oG_{Fe}^\alpha = 5235.02 - 9.4006\ T + 0.52949E\text{-}2\ T^2 - 0.92215E\text{-}6\ T^3$ (1100 - 1500 K)(2)

$^oG_{Cr}^\gamma - {}^oG_{Cr}^\alpha = 10460 + 0.628\ T$(3)

$^oG_{Mn}^\gamma - {}^oG_{Mn}^\alpha = -1800 + 1.276\ T$(3)

$^oG_{Ni}^\gamma - {}^oG_{Ni}^\alpha = -5650 - 3.35\ T$(3)

$^oG_{Si}^\gamma - {}^oG_{Si}^\alpha = 9000 + 3.556\ T$(3)

$L_{Cv}^{Fe} = -21058 - 11.581\ T$(1)

$L_{Cv}^{Cr} = -21058 - 11.581\ T$(1)

$L_{Cv}^{Mn} = -21058 - 11.581\ T$(3)

$L_{Cv}^{Ni} = -21058 - 11.581\ T$(3)

$L_{Cv}^{Si} = -21058 - 11.581\ T$(3)

$L_{FeCr}^{C} = 13110 - 31.820\ T + 2.748\ T\ LnT$(1)

$L_{FeMn}^{C} = 9230 - 10\ T$(3)

$L_{FeNi}^{C} = -14600$(3)

$L_{FeSi}^{C} = -108280$(3)

$L_{FeCr}^{v} = 13110 - 31.820\ T + 2.748\ T\ LnT$(1)

$L_{FeMn}^{v} = 730 - 10\ T$(3)

$L_{FeNi}^{v} = -14600$(3)

$L_{FeSi}^{v} = -108280$(3)

$\Delta G_{Cr} = -251160 + 118\ T$(1)

$\Delta G_{Mn} = -48500$(3)

$\Delta G_{Ni} = 46000$(3)

$\Delta G_{Si} = 123000$(3)

${}^{o}G_{FeC_{3/7}} - {}^{o}G_{Fe}^{\gamma} - 3/7\,{}^{o}G_{C}^{graph} = 16730 - 12.42\ T$(1)

${}^{o}G_{CrC_{3/7}} - {}^{o}G_{Cr}^{\alpha} - 3/7\,{}^{o}G_{C}^{graph} = -16000 - 7.62\ T$(1)

${}^{o}G_{NiC_{3/7}} - {}^{o}G_{Ni}^{\alpha} - 3/7\,{}^{o}G_{C}^{graph} = 42683.49 + 3.4794\ T$(2)

$A_{FeCr} = 750$(1)

$A_{CrNi} = -54182.8$(2)

References

1) R. LUNDBERG, M. WALDENSTROM, and B. UHRENIUS: Calphad, 1977, **1**, 159.
2) I. ANSARA, T. G. CHART, P. Y. CHEVALIER, K. HACK, G.McHUGH, M. H. RAND, P. J. SPENCER: "Phase Diagrams for Fe-Cr-Ni Based Alloys", Part 1, Physical Sciences, Published by the Commission of the European Communities, Report EUR 9657/I/EN, 1985.
3) B. UHRENIUS: "Hardenability Concepts with Applications to Steel", Eds. D. V. DOANE, and J. J. KIRKALDY, Met. Soc. AIME, USA, 1977, pp. 28-81.

APPENDIX 3: COARSENING OF M_7C_3 CARBIDES IN THE AUSTENITE AND FERRITE

The rate-controlling process for the coarsening of the M_7C_3 carbides in the austenite and ferrite is assumed to be diffusion-controlled so that the solute concentrations in the matrix at each carbide will be in equilibrium values. The coarsening rate of precipitates under the diffusion-controlled growth mechanism in binary alloys is well approximated by the following equation;

$$r^3-r_0^3 = 8/9\ \sigma D_M V_M x_M t\ /\ \nu RT \quad \text{(1)} \qquad .....(1)$$

where r_0 is the average carbide radius at the time t=0, V_M the volume of the carbide per 1 mole of alloying element M, σ the interfacial energy, D_M the diffusion coefficient of M in the austenite, x_M the solubility of M atoms, and ν the stoichiometric factor depending upon the composition of carbides.

Since the above equation is valid only for binary systems it can not be directly applied to the Fe-Cr-C system. However, a thermodynamic model has been proposed by Wey et al.,(2) and the same model is accepted in this present study.

1. Thermodynamic Model for the Growth of M_7C_3 Carbides in the Austenite

Spherical carbides with radius r have an excess free energy $2\sigma V^c/r$[1] compared with the carbides having a planar interface ($r=\infty$). The free energies of the carbides with radius r and with critical radius r_c are written as

$$G^c(r) = G^c(\infty) + 2\sigma V^c/r \qquad .....(2)$$

$$G^c(r_c) = G^c(\infty) + 2\sigma V^c/r_c \qquad .....(3)$$

where $G^c(\infty)$ is the free energy of the carbide with plane interface, and r_c is the critical radius below which all carbides are shrinking and above which all carbides are growing.

The change in the Gibbs free energy of the carbides with radius r and r_c is written as

$$\Delta G^c = G^c(r)-G^c(r_c)= 2\sigma V^c\ (1/r - 1/r_c) \qquad .....(4)$$

In the Fe-Cr-C system when the austenite or ferrite and M_7C_3 carbides are in equilibrium the free energies of the carbides can be written as follows

$$G^c(r)= x_{Fe}{}^c\mu_{Fe}{}^\alpha(r) + x_C{}^c\mu_C{}^\alpha(r) + x_{Cr}{}^c\mu_{Cr}{}^\alpha(r) \qquad .....(5)$$

and

$$G^c(r_c)= x_{Fe}{}^c\mu_{Fe}{}^\alpha(r_c) + x_C{}^c\mu_C{}^\alpha(r_c) + x_{Cr}{}^c\mu_{Cr}{}^\alpha(r_c) \qquad .....(6)$$

where $x_{Fe}{}^c$, $x_C{}^c$, $x_{Cr}{}^c$ are the mole fractions of Fe, C, and Cr in the carbide respectively and $\mu_{Fe}{}^\alpha$, $\mu_C{}^\alpha$, $\mu_{Cr}{}^\alpha$ are the corresponding chemical potentials of each element. Applying the Gibbs-Duhem equation to the ternary austenite, the following equation is obtained

$$x_{Fe}{}^\gamma\{\mu_{Fe}{}^\alpha(r)-\mu_{Fe}{}^\alpha(r_c)\}+ x_C{}^\gamma\{\mu_C{}^\alpha(r)-\mu_C{}^\alpha(r_c)\}+ x_{Cr}{}^\gamma\{\mu_{Cr}{}^\alpha(r)-\mu_{Cr}{}^\alpha(r_c)\}= 0 \qquad .....(7)$$

---

[1] V^c is the volume of the carbide per 1 mole of constituent atoms.

Due to relatively high diffusivity of carbon in the austenite, the chemical potential of carbon is assumed to be constant for different sizes of carbides. Subsequently, from equations 5, 6, and 7 Gibbs free energy change due to carbide growth is written as

$$\Delta G^{c} = (x_{Fe}{}^{\gamma} x_{Cr}{}^{c} - x_{Cr}{}^{\gamma} x_{Fe}{}^{c} / x_{Fe}{}^{\gamma}) \, \Delta\mu_{Cr}{}^{\alpha} \qquad .....(8)$$

where $\Delta\mu_{Cr}{}^{\alpha}$ arises due to the difference in carbide size and can be written using equations 4 and 8 as follows;

$$\Delta\mu_{Cr}{}^{\alpha} = (2\sigma V^{c} x_{Fe}{}^{\gamma} / x_{Fe}{}^{\gamma} x_{Cr}{}^{c} - x_{Cr}{}^{\gamma} x_{Fe}{}^{c}) \, (1/r - 1/r_{c}) \qquad .....(9)$$

The positive chemical potential difference arises due to the fact that growth of the carbide requires a net flux of Cr atoms from the austenite into the M_7C_3 carbides. The net flux of Cr atoms in the austenite is represented as follows.

$$J_{Cr}{}^{\alpha} = -x_{Cr}{}^{\gamma} m_{Cr}{}^{\gamma} \Delta\mu_{Cr}{}^{\alpha} / V^{\alpha}\delta \qquad .....(10)$$

where $m_{Cr}{}^{\gamma}$ is the mobility of Cr atoms in the austenite,[2] and V^{α} is the molar volume of austenite, and δ the effective diffusion distance which is assumed to be equal to the particle radius r. When the flux balance across the interface between austenite and carbide is applied $J_{Cr}{}^{\alpha}$ is written as follows.

$$J_{Cr}{}^{\alpha} = 1/V^{Cr} \, \{x_{Cr}{}^{c} - x_{Cr}{}^{\gamma}(1 - x_{C}{}^{c}/1 - x_{C}{}^{\gamma})\} dr/dt \qquad .....(11)$$

Then the following equation is obtained from equations 10 and 11

$$1/V^{c}\{x_{Cr}{}^{c} - x_{Cr}{}^{\gamma}(1 - x_{C}{}^{c}/1 - x_{C}{}^{\gamma})\} dr/dt = - x_{Cr}{}^{\gamma} D_{Cr}{}^{\gamma} \Delta\mu_{Cr}{}^{\alpha} / V^{\alpha} r RT \qquad .....(12)$$

Using the molar fractions which are defined in the regular solution model as $y_{Cr} = x_{Cr}/1 - x_{C}$, $y_{Fe} = x_{Fe}/1 - x_{C}$, $y_{C} = x_{C}/1 - x_{C}$, and approximating that $V/(1 - x_{C})$ has the same value for both M_7C_3 and γ and clarifying that r_c is equal to the average particle radius r, the rate-controlling equation is written as follows;

$$r^{3} - r_{o}{}^{3} = 8(a+b)\sigma V^{c} D_{Cr}{}^{\gamma} y_{Cr}{}^{\alpha} t \, / \, 9aRT(y_{Cr}{}^{c} - y_{Cr}{}^{\alpha})^{2} \qquad .....(13)$$

This equation is used for the calculation of M_7C_3 carbide growth in the austenite and ferrite. The values of $D_{Cr}{}^{\gamma/\alpha}$, $y_{Cr}{}^{M_7C_3}$, $y_{Cr}{}^{\gamma/\alpha}$, and $y_{C}{}^{\gamma/\alpha}$ used for the calculations are shown in Table 1. The interface energy σ is assumed to be $0.7 J/m^2$ referring to the ferrite/cementite interface energy, and the molar volume $V^{M_7C_3}$ for Cr_7C_3 is $7.1 \ 10^{-6} \ m^3/mol$.

---

[2] The mobility of Cr atoms is defined as $D_{Cr}{}^{\gamma}/RT$, where $D_{Cr}{}^{\gamma}$ is the diffusion coefficient of Cr in the austenite, R the gas constant, and T is the temperature.

Table 1: Theoretically calculated Cr and C concentrations when the austenite, or ferrite* is in equilibrium with M_7C_3 in Fe-Cr-C system, and diffusion coefficient of Cr as a function of temperature.[3]

Temperature	$y_{Cr}^{\gamma/\alpha}$	$y_{C}^{\gamma/\alpha}$	$y_{Cr}^{M_7C_3}$	$D_{Cr}^{\gamma/\alpha}$
700*	0.025	0.015	0.71	$2.984\ 10^{-17}$
750*	0.039	0.016	0.70	$1.356\ 10^{-16}$
800*	0.04	0.018	0.70	$5.357\ 10^{-16}$
900	0.06	0.020	0.68	$1.111\ 10^{-16}$
1000	0.08	0.028	0.66	$1.164\ 10^{-15}$
1100	0.11	0.032	0.64	$8.661\ 10^{-15}$

Fig. 1 represents the calculated curves illustrating the change in the cube of average particle radius (μm^3) as a function of time (hours) at 1100, 1000, 900, 800, 750, and 700°C. This figure demonstrates the linear relationship between the cube of average particle radius and the time indicating that Cr_7C_3 carbides increase their size by the Ostwald ripening mechanism in the wide range of temperature region.

---

[3] Diffusion coefficient of Cr in the austenite and ferrite is calculated using the following equations given by Bowen and Leak.(3)

$$D = 8.52 \exp(-59.900 / RT) \text{ for ferrite}$$
$$D = 10.80 \exp(-69.700 / RT) \text{ for austenite}$$

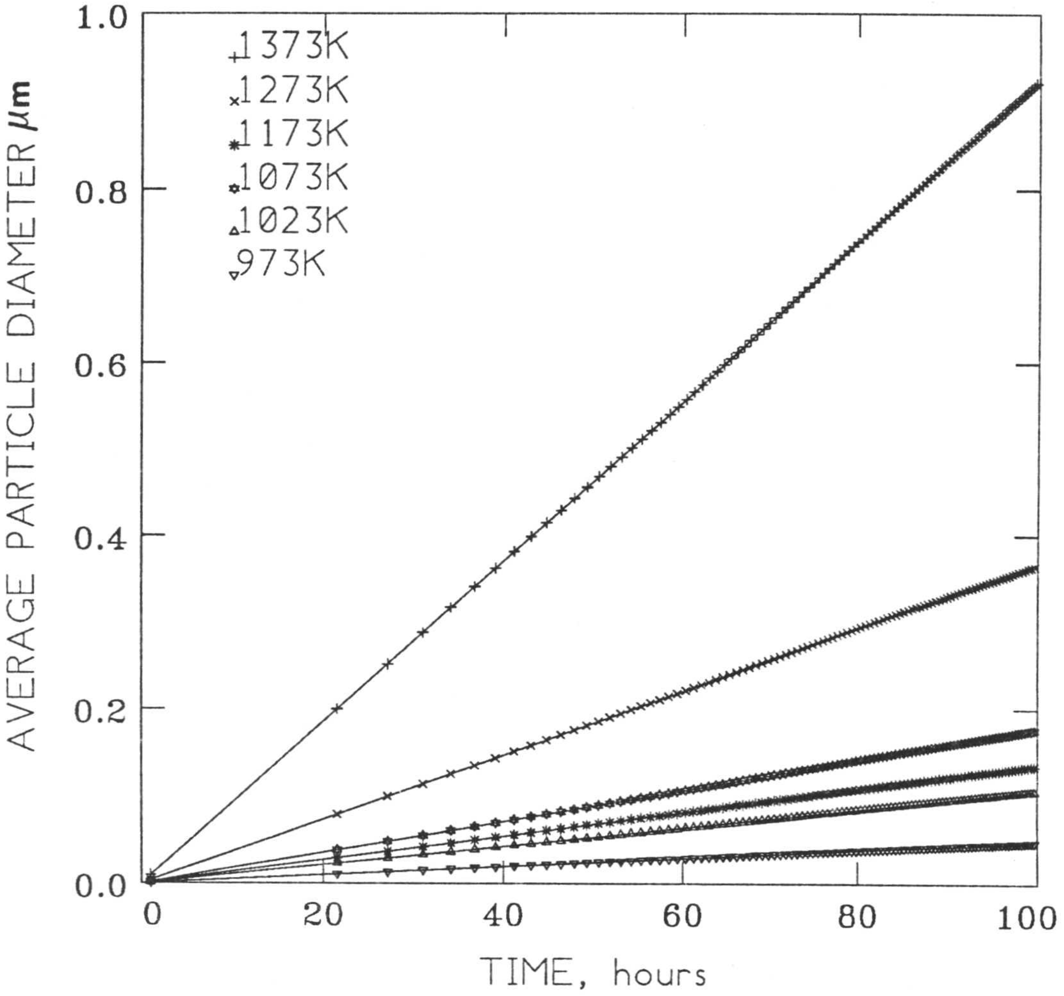

Fig. 1: The cube of average particle radius versus time curves representing the coarsening of the Cr_7C_3 carbides in the austenite and ferrite at 1100, 1000, 900, 800, 750, and 700°C.

1. References

1) J. W. MARTIN, and R. D. HONERTY: "Stability of Microstructure in Metallic Systems", Cambridge University Press, 1976.
2) M. Y. WEY, T. SAKUMA, and T. NISHIZAWA: Trans. of the Japan Institute of Metals, 1981, **22**, 733.

APPENDIX 4: COMPUTER PROGRAM FOR PREDICTION OF WELD BEAD DIMENSIONS AND DILUTION

```
FTVSCLR PROGRAM=%H% DATA=* NAG
C PROGRAM CALCULATES THE WELD BEAD DIMENSIONS AND THE DILUTION
C AS A FUNCTION OF WELDING VARIABLES
C TPEAK=PEAK TEMPERATURE (K)
C TPHEAT=PREHEAT TEMPERATURE $T_o$
C SAB=SURFACE ABSORPTIVITY 0.7
C Q=ARC POWER (J/s)
C V=ARC VELOCITY (m/s)
C THCON=THERMAL CONDUCTIVITY $\lambda$ (J $s^{-1}m^{-1}$ $K^{-1}$)
C T=TIME (s)
C TO=THE TIME TAKEN FOR HEAT TO DIFFUSE OVER THE
C BEAM HALF-WIDTH, $r_b$.
C $r_b$=RADIUS OF HEAT SOURCE (m), WHICH IS ASSUMMED TO BE
C PROPORTIONAL TO THE RADIUS OF THE WELDING ELECTRODE
C THDIF=THERMAL DIFFUSIVITY ($m^2$/s)
C VTCAP=VOLUME THERMAL CAPACITY J $m^{-3}K^{-1}$
C Z=DISTANCE BELOW SURFACE (m)
C Y=DISTANCE FROM CENTRE (m)
C $Z_0$=MEASURES THE DISTANCE OVER WHICH HEAT CAN DIFFUSE
C DURING THE INTERACTION TIME $r_b/\upsilon$
C BEADA=BEAD AREA ($m^2$)
C BEADH=BEAD HEIGHT (m)
C DILUT=DILUTION
C ZMELT=MELT DEPTH (m)
C LAHEAT=LATENT HEAT PER UNIT VOLUME (J $m^{-3}$)
C TDIF=TOTAL C DIFFUSION TIME FROM THE FUSION ZONE TO THE
C BASE MATERIAL ($m^2s^{-1}$)
C CDEPO=C CONCENTRATION OF THE DEPOSIT (Wt%)
C CBASE=C CONCENTRATION OF THE BASE MATERIAL (Wt%)
C DIFCO=DIFFUSION COEFFICIENT OF CARBON IN THE AUSTENITE
C
IMPLICIT REAL*8 (A-H,O-$)
DOUBLE PRECISION TPHEAT,SAB,Q,V,PI,THCON,POPO
DOUBLE PRECISION T,TO,RB,THDIF,Y,Z,Z0,TIMEP,TNEW
DOUBLE PRECISION TNEW1,TNEW2,TNEW3,TNEW4,TNEW5
DOUBLE PRECISION TNEW6,TNEW7,TNEW8,TNEW9
```

```
DOUBLE PRECISION BEADA,BEADH,DILUT,ZMELT,LAHEAT
DOUBLE PRECISION RECO,DIA,FEEDS,AREA1,AREA2
DOUBLE PRECISION Y1,Y2,Y3,Y4,Y5,YNEW,ZNEW
DOUBLE PRECISION LAZ,S1,S2,S3
INTEGER N,J
COMMON/ONE/ZO,TO,TPHEAT,THDIF,THCON
COMMON/TWO/Q,V,PI
COMMON/THREE/Y,Z
COMMON/FOUR/VTCAP
CALL STAR
WRITE (*,40)
CALL STAR
998 WRITE (*,50)
CALL STAR
40 FORMAT ( ' CALCULATION OF THE WELD BEAD GEOMETRY AND ' ,
& ' THE DILUTION ' /' USING TWO DIMENSIONAL HEAT ',
& ' FLOW EQUATIONS ' /// ' NOTE: ALL ' ,
& ' UNITS IN KELVIN, JOULE, METER, AND SECOND ' //)
50 FORMAT ( ' PLEASE CHOOSE ONE OF THE OPTIONS ' ///
& ' 1: CALCULATION OF THE PEAK TEMPERATURE FOR A GIVEN POINT ' /
& ' 2: TEMPERATURE TIME CURVES FOR A GIVEN POINT ' /
& ' 3: CALCULATION OF THE WELD BEAD DIMENSIONS ' /
& ' AND CALCULATION OF THE DILUTION ' /
& ' 4: MINIMUM HEAT INPUT (J/m) VALUE IN ORDER TO ACHIEVE ' /
& ' SUFFICIENT SURFACING FOR A GIVEN ARC SPEED ' /
& ' 5: CALCULATION OF CARBON DIFFUSION PROFILE ' /
& ' FROM THE FUSION ZONE TO THE SUBSTRATE ' //)
READ (5,*) J
IF (J .EQ. 4) THEN
GOTO 12
ENDIF
WRITE (6,*) ' ARC POWER: '
READ (5,*) Q
12 CONTINUE
IF (J .EQ. 3) THEN
WRITE (6,*) ' FEED SPEED: '
READ (5,*) FEEDS
ENDIF
WRITE (6,*) ' ARC VELOCITY: '
```

```
READ (5,*) V
WRITE (6,*) ' PREHEAT TEMPERATURE: '
READ (5,*) TPHEAT
WRITE (6,*) ' RADIUS OF HEAT SOURCE '
READ (5,*) RB
IF (J .EQ. 3) THEN
GOTO 327
ELSE IF (J .EQ. 4) THEN
GOTO 327
ELSE IF (J .EQ. 5) THEN
GOTO 327
ENDIF
WRITE (6,*) ' DISTANCE BELOW THE SURFACE '
READ (5,*) Z
WRITE (6,*) ' DISTANCE FROM THE CENTRE LINE '
READ (5,*) Y
327 CONTINUE
SAB=0.7D0
PI=X01AAF(DUMMY)
THCON=0.41D2
THDIF=9.1D-6
VTCAP=4.5D6
LAHEAT=2.1D9
DIA=4.0D-3
RECO=0.67
TO=(RB**2.0)/(4.0*THDIF)
ZO=SQRT((RB/EXP(1.0))*(SQRT(PI*THDIF*RB/V)))
IF (J .EQ. 1) THEN
GOTO 130
ELSE IF (J .EQ. 2) THEN
GOTO 128
ELSE IF (J .EQ. 3) THEN
GOTO 129
ELSE IF (J .EQ. 4) THEN
GOTO 127
ELSE IF (J .EQ. 5) THEN
GOTO 144
ENDIF
130 CONTINUE
```

```
CALL TPEAK (TPHEAT,Q,V,PI,THCON,TO,THDIF,Y,Z,ZO,TIMEP)
TNEW=TP(TIMEP)
WRITE (6,*) ' PEAK TEMPERATURE IS EQUAL TO ' , TNEW
GOTO 221
C *********************************************************
128 CONTINUE
C TEMPERATURE - TIME CURVES FOR A GIVEN POINT
C
CALL TEMPTI
GOTO 221
C ************************************************************
C CALCULATION OF WELD BEAD DIMENSIONS, MELTED AREA,
C DEPOSITED AREA, AND THE DILUTION.
C
129 CONTINUE
DO 69 Z=0.1D-4, 0.06, 0.1D-3
Y=0.0
CALL TPEAK(TPHEAT,Q,V,PI,THCON,TO,THDIF,Y,
&Z,ZO,TIMEP)
TNEW1=TP(TIMEP)
IF (TNEW1 .LT. 1.820D3) THEN
GOTO 132
ENDIF
69 CONTINUE
132 WRITE (6,*) ' MELT DEPTH IS EQUAL TO ' , Z
ZNEW=Z
C *******************************************************
C CALLING THE SUBROUTINE CALCULATING THE MELT DEPTH BY
C TAKING INTO ACCOUNT THE LATENT HEAT
C *******************************************************
CALL DIFZ(VTCAP,LAHEAT,Q,V,ZO,TPHEAT,LAZ,PI)
C
DO 70 Y=0.1D-4, 0.06D0, 0.1D-2
Z=0.0
CALL TPEAK(TPHEAT,Q,V,PI,THCON,TO,THDIF,Y,
&Z,ZO,TIMEP)
TNEW2=TP(TIMEP)
IF (TNEW2 .LT. 1.820D3) THEN
GOTO 135
```

```
ENDIF
70 CONTINUE
135 WRITE (6,*) ' BEAD WIDTH IS EQUAL TO ' , 2.0D3*Y
C ***************************************************************
YNEW=Y
C GENERATION OF THE WHOLE FUSION BOUNDARY
C *****************************************************************
Y=Y/2.0
DO 80 Z=0.1D-4, 0.06D0, 0.1D-3
CALL TPEAK(TPHEAT,Q,V,PI,THCON,TO,THDIF,Y,
&Z,ZO,TIMEP)
TNEW4=TP(TIMEP)
IF (TNEW4 .LT. 1.820D3) THEN
GOTO 332
ENDIF
80 CONTINUE
332 CONTINUE
C
Y=Y/4.0
DO 81 Z=0.1D-4, 0.06D0, 0.1D-3
CALL TPEAK(TPHEAT,Q,V,PI,THCON,TO,THDIF,Y,
&Z,ZO,TIMEP)
TNEW5=TP(TIMEP)
IF (TNEW5 .LT. 1.820D3) THEN
GOTO 333
ENDIF
81 CONTINUE
333 CONTINUE
C
Y=Y/6.0
DO 82 Z=0.1D-4, 0.06D0, 0.1D-3
CALL TPEAK(TPHEAT,Q,V,PI,THCON,TO,THDIF,Y,
&Z,ZO,TIMEP)
TNEW6=TP(TIMEP)
IF (TNEW6 .LT. 1.820D3) THEN
GOTO 334
ENDIF
82 CONTINUE
334 CONTINUE
```

```
C
Y=Y/8.0
DO 83 Z=0.1D-4, 0.06D0, 0.1D-3
CALL TPEAK(TPHEAT,Q,V,PI,THCON,TO,THDIF,Y,
&Z,ZO,TIMEP)
TNEW7=TP(TIMEP)
IF (TNEW7 .LT. 1.820D3) THEN
GOTO 335
ENDIF
83 CONTINUE
335 CONTINUE
C *****************************************************
CALL BEAD1 (RECO,DIA,FEEDS,V,AREA1)
CALL FIRST1 (BEADH,YNEW,ZNEW,AREA1)
CALL FIRST2 (BEADH,YNEW,ZNEW,AREA2)
C CALCULATION OF THE DILUTION
C
DILUT=(AREA2/(AREA1+AREA2))*1.0D2
WRITE (6,*) ' DILUTION IS EQUAL TO ' , DILUT
GOTO 221
C
C CALCULATION OF THE CRITICAL HEAT INPUT VALUE FOR A
C GIVEN ARC SPEED.
C *******************************************************
127 CONTINUE
CALL CRITIC (TPHEAT,VTCAP,MINIM,ZO,PI,RB,THCON,Q)
GOTO 221
C ********************************************************
144 CONTINUE
DO 66 Z=0.1D-4, 0.06, 0.1D-3
Y=0.0
CALL TPEAK(TPHEAT,Q,V,PI,THCON,TO,THDIF,Y,
&Z,ZO,TIMEP)
TNEW9=TP(TIMEP)
IF (TNEW9 .LT. 1.820D3) THEN
GOTO 162
ENDIF
66 CONTINUE
162 CONTINUE
```

```
ZMEL=Z
WRITE (6,*) ' ZMEL IS EQUAL TO ' , ZMEL
CALL DIFT (ZMEL)
221 WRITE (6,43)
43 FORMAT ( ' MORE ANALYSIS? (1=YES, 2=NO) ' /)
READ (5,*) L
IF (L .EQ. 1) THEN
GOTO 998
ELSE IF (L .EQ. 2) THEN
GOTO 85
ENDIF
85 STOP
END
C ************************************************************
C ************************************************************
SUBROUTINE TPEAK (TPHEAT,Q,V,PI,THCON,TO,THDIF,Y,Z,ZO,TIMEP)
IMPLICIT REAL*8 (A-H,O-$)
DOUBLE PRECISION TPHEAT,Q,V,PI,THCON,TO,THDIF,Y,Z,ZO,TIMEP
DOUBLE PRECISION A(4),REZ(4),IMZ(4),TOL
INTEGER K,N,IFAIL,M
N=4
IFAIL=0
M=0
TOL=X02AAF(ZIP)
A(1)=4.0*THDIF
A(2)=(6.0D0*TO*THDIF)-(Z+ZO)**2.0D0-(Y**2.0D0)
A(3)=(2.0D0*(TO**2.0D0)*THDIF)-(2.0D0*TO*(Z+ZO)**2.0D0)
A(4)=-(TO**2.0D0*(Z+ZO)**2.0D0)
CALL C02AEF (A,N,REZ,IMZ,TOL,IFAIL)
DO 75 K=1,3
IF ((IMZ(K) .EQ. 0.0) .AND. (REZ(K) .GT. 0.0)) THEN
TIMEP=REZ(K)
M=M+1
ENDIF
75 CONTINUE
IF (M .EQ. 0) THEN
WRITE (6,*) ' NO MAXIMUM TEMPERATURE WAS FOUND '
STOP
ENDIF
```

```
IF (M .GT. 1) THEN
WRITE (6,*) ' THERE ARE MORE THAN ONE PEAK TEMPERATURE '
STOP
ENDIF
RETURN
END
C ***************************************************************
C ***************************************************************
DOUBLE PRECISION FUNCTION TP(TIMEP)
IMPLICIT REAL*8 (A-H,O-$)
DOUBLE PRECISION TPHEAT,Q,V,PI,THCON,TO,THDIF,Y,Z,ZO,TIMEP
DOUBLE PRECISION P1,P2
COMMON/ONE/ZO,TO,TPHEAT,THDIF,THCON
COMMON/TWO/Q,V,PI
COMMON/THREE/Y,Z
COMMON/FOUR/VTCAP
PI=X01AAF(TRIP)
P1=Q*0.65/(V*2.0*PI*THCON*SQRT(TIMEP*(TIMEP+TO)))
P2=(((Z+ZO)**2.0D0)/TIMEP)+(Y**2.0D0)/(TIMEP+TO)
TP=TPHEAT+P1*EXP(-P2/(4.0D0*THDIF))
RETURN
END
C SUBROUTINE FOR TEMPERATURE TIME CURVES FOR A GIVEN POINT
SUBROUTINE TEMPTI
IMPLICIT REAL*8 (A-H,O-$)
DOUBLE PRECISION TPHEAT,Q,V,PI,THCON,TO,THDIF,Y,Z,ZO
DOUBLE PRECISION TEMP,TIM
DOUBLE PRECISION S1,S2
COMMON/ONE/ZO,TO,TPHEAT,THDIF,THCON
COMMON/TWO/Q,V,PI
COMMON/THREE/Y,Z
COMMON/FOUR/VTCAP
INTEGER M,N
PI=X01AAF(TRIP)
DO 55 TIM=0.1, 50, 0.5
S1=Q/(V*2.0*PI*THCON*SQRT(TIM*(TIM+TO)))
S2=(((Z+ZO)**2.0D0)/TIM)+(Y**2.0D0)/(TIM+TO)
TEMP=TPHEAT+S1*EXP(-S2/(4.0D0*THDIF))
WRITE (6,*) TIM,TEMP
```

```
55 CONTINUE
RETURN
END
C
C CALCULATING THE BEAD AREA FROM RECOVERY
C
SUBROUTINE BEAD1 (RECO,DIA,FEEDS,V,AREA1)
IMPLICIT REAL*8 (A-H,O-$)
DOUBLE PRECISION RECO,DIA,FEEDS,V,AREA1,PI
DOUBLE PRECISION A1,A2
PI=X01AAF(TRIP)
A1=PI*(DIA**2.0)/4.0D0
A2=FEEDS/V
AREA1=A1*A2
WRITE (6,*) ' AREA1 IS EQUAL TO (mm2) ' , AREA1*1.0D6
RETURN
END
C
C CALCULATING THE BEAD HEIGHT BY ITERATION
C
SUBROUTINE FIRST1 (BEADH,YNEW,ZNEW,AREA1)
IMPLICIT REAL*8 (A-H,O-$)
DOUBLE PRECISION BEADH,Y,Z,AREA1
BEADH=0.3D-1
28 T1=2.0D0*YNEW/(2.0D0*BEADH)
T2=BEADH/ZNEW
T3=((2.0D0*T1)/(1.0D0+T1**2.0))*BEADH**2.0D0
T4=((1.0D0+T1**2.0D0)/2.0D0)**2.0D0
T5=DASIN(T3*T4)
T6=(BEADH**2.0D0)*T1
T7=((T1**2.0D0)-1.0D0)/2.0D0
T8=T6*T7
FUNC=T5-T8-AREA1
IF (FUNC .LT. 0.1D-4) THEN
GOTO 152
ENDIF
C CALCULATION OF THE DIFFERENTIATION
T10=1.0D0/SQRT(1.0D0-(T3*T4)**2.0D0)
T11=(1.0D0+(T1**2.0D0))*BEADH*2.0
```

```
T12=(4.0D0*(YNEW**2.0D0))/(BEADH**2.0D0)
T13=T11+T12
T14=(1.0D0+(T1**2.0D0))**2.0D0
T15=T13/T14
T16=-(YNEW**2.0D0*(1.0D0+(T1**2.0)))/(BEADH**3.0D0)
TFINAL=(T15*T4)+(T16*T3)
FIRSTD=T10*TFINAL
T17=YNEW+((T**3.0D0)/(BEADH**2.0D0))
TLAST=FIRSTD+T17
BEADH=BEADH-(FUNC/TLAST)
GOTO 28
152 WRITE (6,*) ' WELD BEAD HEIGHT IS EQUAL TO: ' , BEADH*1.0D3
RETURN
END
C
C CALCULATION OF THE AREA OF THE WELD POOL
C
SUBROUTINE FIRST2 (BEADH,YNEW,ZNEW,AREA2)
IMPLICIT REAL*8 (A-H,O-$)
DOUBLE PRECISION BEADH,YNEW,ZNEW,AREA2
S1=YNEW/BEADH
S2=BEADH/ZNEW
S3=(2.0D0*S1*S2)/(1.0D0+(S1**2.0D0)*(S2**2.0D0))
S4=(BEADH**2.0D0)/(S2**2.0D0)
S5=((1.0D0+(S1**2.0D0)*(S2**2.0D0))/2.0D0)**2.0D0
S6=S3*S4*S5
S7=DASIN(S6)
S8=((BEADH**2.0D0)*S1)/S2
S9=(((S1**2.0D0)*(S2**2.0D0))-1.0D0)/2.0D0
S10=-S8*S9
AREA2=S7+S10
WRITE (6,*) ' AREA2 IS EQUAL TO ' , AREA2*1.0D6
RETURN
END
C
SUBROUTINE STAR
WRITE (6,*) ' *********************************************** '
WRITE (6,*) ' *********************************************** '
RETURN
```

```
END
C
SUBROUTINE DIFZ(VTCAP,LAHEAT,Q,V,ZO,TPHEAT,LAZ,PI)
IMPLICIT REAL*8 (A-H,O-$)
DOUBLE PRECISION VTCAP,LAHEAT,Q,V,ZO,TPHET,LAZ,PI
LAZ=0.1D-4
77 R1=PI*(LAZ**2.0D0)*VλHEAT/2.0D0
R1=(0.7D0*Q)-R1
R2=VTCAP*((LAZ+ZO)**2.0D0)*V
R3=((R1/R2)*2.0D0)/(PI*EXP(1.0))
TFUNC=TPHEAT+R3-1.820D3
IF (TFUNC .LT. 0.1) THEN
GOTO 199
ENDIF
R4=-(R2*PIλZ*VλHEAT)/2.0D0
R5=Q-((PI*(LAZ**2.0D0)*VλHEAT)/2.0D0)
R6=2.0D0*VTCAP*V*(LAZ+ZO)
R7=-R5*R6
R8=(VTCAP*V*((LAZ+ZO)**2.0D0))**2.0D0
R9=(R4+R7)/R8
RTUREV=(2.0D0*R9)/(PI*EXP(1.0))
LAZ=LAZ-(TFUNC/RTUREV)
GOTO 77
199 CONTINUE
WRITE (6,*) ' MELT DEPTH BY TAKING INTO ACCOUNT THE LATENT HEAT
&IS EQUAL TO ' , LAZ*1.0D3
RETURN
END
C ********************************************************
SUBROUTINE CRITIC (TPHEAT,VTCAP,MINIM,ZO,PI,RB,THCON,Q)
DOUBLE PRECISION RB,THCON,Q
DOUBLE PRECISION TPHEAT,VTCAP,MINIM,ZO,PI
DOUBLE PRECISION V1,V2,V3,V4,V5
V1=PI*EXP(1.0)*VTCAP*((0.1D-3+ZO)**2.0D0)
V2=2.0*0.7/V1
V3=(1.820D3-TPHEAT)*V2
MINIM=V3
WRITE (6,*) ' MINIMUM HEAT INPUT (J/m): ' , MINIM
RETURN
```

```
END
C ****************************************************************************
SUBROUTINE DIFT (ZMEL)
IMPLICIT REAL*8 (A-H,O-$)
DOUBLE PRECISION ZMEL,Y,THDIF
DOUBLE PRECISION T12,T13,T14,CBASE,CSURF,DIFCO,CCOMPO
DOUBLE PRECISION TIM,PI,S1,S2,S3
DOUBLE PRECISION TEMP
INTEGER N
COMMON/ONE/ZO,TO,TPHEAT,THDIF,THCON
COMMON/TWO/Q,V,PI
Y=0.0
TIM=0.1D0
CBASE=0.1D0
CSURF=1.5D0
DO 38 N=1, 300
Z=ZMEL+(0.1D-6*(N-1))
TIM=TIM+(0.5D0*(N-1))
S1=Q/(V*2.0D0*PI*THCON*SQRT(TIM*(TIM+TO)))
S2=(((Z+ZO)**2.0D0)/TIM)+(Y**2.0D0)/(TIM+TO)
TEMP=TPHEAT+S1*EXP(-S2/(4.0D0*THDIF))
DIFCO=1.0D-5*DEXP(-1.35D5/(8.314D0*TEMP))
T12=SQRT(DIFCO*TIM)
T15=0.1D-6*(N-1)
T13=T15/(2.0D0*T12)
T14=DERFC(T13)
CCOMPO=CBASE+((CSURF-CBASE)*T14)
WRITE (6,*) T15, CCOMPO
IF (CCOMPO .LT. CBASE+0.1D-3) THEN
GOTO 888
ENDIF
38 CONTINUE
888 CONTINUE
RETURN
END
%
```

APPENDIX 5: WELDING TERMINOLOGY

Arc Voltage: The voltage across the welding arc.

Arc Welding: A group of welding processes which produce coalescence of metals by heating them with an arc, with or without the use of filler metal.

Arc Welding Electrode: A component of the welding circuit through which current is conducted between the electrode holder and the arc.

As-Welded: The condition of weld metal, welded joints, and weldments after welding but prior to any subsequent thermal, mechanical, or chemical treatments.

Automatic Welding: Welding with equipment which performs the welding operation without adjustment of the controls by a welding operator.

Base Metal: The metal to be welded, brazed, soldered or cut.

Burnoff-Rate (melting rate): The weight or length of electrode melted in unit time.

Cladding: A relatively thick layer (>1mm) of material applied by surfacing for the purpose of improved corrosion resistance or other properties.

Coalescence: The growing together or growth into one body of the materials being welded.

Continuous Wave (CW) CO2 Laser: A gas Laser consisting of an optically transparent tube filled with CO2 gas.

Covered Electrode: A composite filler metal electrode consisting of a core of a bare electrode or metal cored electrode to which a covering sufficient to provide a slag layer on the weld metal has been applied.

Deposition Efficiency (Arc Efficiency): The ratio of the weigth of deposited metal to the net weight of filler metal consumed.

Deposition Rate: The weight of material deposited in a unit time.

Depth of Fusion: The distance that fusion extends into the base metal or previous pass from the surface melted during welding.

Dilution: The change in chemical composition of a welding filler material caused by the mixture of the base material in the deposited weld bead. It is normally measured by the percentage of base material or previously deposited weld material in the weld bead.

Direct current electrode negative (DCEN): The arrangement of direct current arc welding leads in which the work is the positive pole and the electrode is the negative pole of the welding arc.

Direct current electrode positive (DCEP): The arrangement of direct current arc welding in which the work is the negative pole and the electrode is the positive pole of the welding arc.

Drag Angle (Electrode Angle): The angle that the electrode makes with the referenced plane or surface of the base metal in a plane perpendicular to the axis of the weld.

Electrode Stickout (Electrode extension): The length of unmelted electrode extending beyond the end of the contact tube during welding.

Filler metal: The metal to be added in making a welded, brazed or soldered joint.

Flux Cored Arc Welding (FCAW): An arc welding process which produces coalescence of metals by heating them with an arc between a continuous filler metal (consumable) elctrode and the work. Shielding is provided by a flux contained within tubular electrode.

Fusion: The melting together of filler metal and base metal, or of base metal only, which results in coalescence.

Fusion Zone: The area of base metal melted as determined on the cross section of a weld.

Gas Tungsten Arc Welding (TIG): An arc welding process which produces coalescence of metals by heating them with an arc between a tungsten (nonconsumable) electrode and the work. Shielding is obtained from a gas or gas mixture. Pressure may or may not be used and filler metal may or may not be used.

Hardfacing: A particular form of surfacing in which a coating or cladding is applied to a substrate for the main purpose of reducing wear or loss of material by abrasion, impact, erosion, galling and cavitation.

Heat-Affected-Zone (HAZ): That portion of the base metal which has not been melted, but whose mechanical properties or microstructure have been altered by the heat of welding, brazing, soldering or cutting.

Inert Gas: A gas which does not normally combine chemically with the base metal or filler metal.

Interpass Temperature: In a multiple-pass weld, the temperature (minumum or maximum as specified) of the deposited weld metal before the next pass is started.

Plasma Arc Welding: An arc welding process which produces coalescence of metals by heating them with a constricted arc between an electrode and the workpiece or the electrode and the constricting nozle.

Residual Stress: Stress remaining in a structure or member as a result of thermal or mechanical treatment or both. Stress arises in fusion welding primarily because the weld metal contracts on cooling from the solidus to room temperature.

Submerged Arc Welding (SAW): An arc welding process which produces coalescence of metals by heating them with an arc or arcs between a bare metal electrode or electrodes and the work. The arc and molten metal are shielded by a blanket of granular, fusible material on the work.

Thermal Spraying (THSP): A group of welding or allied processes in which finely divided metallic or nonmetallic materials are deposited in a molten or semi-molten condition to form a coating.

Thermal Stresses: Stresses in weld metal resulting from nonuniform temperature distributions.

APPENDIX 6: COMPUTER PROGRAM FOR NI-BASED ALLOYS

```
FTVSCLR PROGRAM=%H% DATA=.DATA
C THIS PROGRAM ALLOWS TO CALCULATE THE VOLUME FRACTION OF
C GAMMA PRIME PRECIPITATES, COMPOSITION OF GAMMA AND GAMMA
C PRIME PHASES, LATTICE MISMATCH BETWEEN GAMMA AND GAMMA
C PRIME PHASES, AND STRENGTH AS A FUNCTION OF ALLOY
C COMPOSITION FOR A GIVEN ALLOY
C S(I)=Wt% OF ALLOYING ELEMENTS
C K(I)=ATOMIC WEIGHT OF ALLOYING ELEMENTS
C A(I)=At% OF ALLOYING ELEMENTS
C Y(I)=ATOMIC PERCANTAGE OF ALLOYING ELEMENTS IN GAMMA PRIME
C V(I)=ATOMIC PERCANTAGE OF ALLOYING ELEMENTS IN GAMMA
C X=AL CONCENTRATION BY GAMMA PRIME SURFACE EQUATION
C B=GAMMA PRIME LATTICE PARAMETER
C C=GAMMA LATTICE PARAMETER
C M=%LATTICE MISFIT
C F=VOLUME FRACTION OF GAMMA PRIME
C T=EXPANSION COEFFICIENT AT 538 0C (10E-6/0C
DIMENSION A(8),V(8),Y(8),K(8),S(8),P(8),VAC(8)
DOUBLE PRECISION F,K,M,T
DOUBLE PRECISION OVERS,PS,SSS
DOUBLE PRECISION UTS20,UTS650,UTS760,UTS871,UTS982,LATMIS
201 READ (5,*,END=200)( S(I),I=1,8)
T=14.378+(0.0123*S(6)+0.0284*S(2)-0.1012*S(3)-0.0520*S(7)
+-0.1280*S(5)-0.0214*S(4)-0.0165*S(8))
DATA (P(I),I=1,8)/0.66,4.66,4.66,7.66,6.66,1.71,4.66,4.66/
C FROM WPERC TO APERC
DATA (K(I),I=1,8)/58.71,51.996,95.94,26.9815,47.90,58.9332,
+183.85,180.947/
DO 10 I=1,8
10 A(I)=S(I)/K(I)
SUMI=A(1)+A(2)+A(3)+A(4)+A(5)+A(6)+A(7)+A(8)
DO 15 I=1,8
A(I)=A(I)/SUMI
15 A(I)=A(I)*100
F=0.003
4 N=1
5 Y(2)=A(2)/(F+(1.0-F)*7.3737)
```

```
Y(3)=A(3)/(F+(1.0-F)*3.9932)
Y(4)=A(4)/(F+(1.0-F)*0.2413)
Y(5)=A(5)/(F+(1.0-F)*0.1955)
Y(6)=A(6)/(F+(1.0-F)*2.652)
Y(7)=A(7)/(F+(1.0-F)*1.7615)
Y(8)=A(8)/(F+(1.0-F)*0.2049)
Y(1)=100-(Y(2)+Y(3)+Y(4)+Y(5)+Y(6)+Y(7)+Y(8))
X=24.0484-(0.5765*Y(2))-(1.1096*Y(3))-(0.9016*Y(5))-(0.0292*Y(6))
X=X-(1.0567*Y(7))-(1.1123*Y(8))
DAL=X-Y(4)
IF (ABS(DAL) .LT. 0.001) GOTO 50
IF (N .EQ. 2) GOTO 48
DALO=DAL
FO=F
F=F+0.0001
N=N+1
GOTO 5
48 F=F-0.0001*DAL/(DAL-DALO)
GOTO 4
50 V(2)=Y(2)*7.3737
V(3)=Y(3)*3.9932 SA104.APPENDIX(GAMMA) 7 SEP 88 16.40
V(4)=Y(4)*0.2413
V(5)=Y(5)*0.1955
V(6)=Y(6)*2.702
V(7)=Y(7)*0.552
V(8)=Y(8)*0.261
V(1)=100-(V(2)+V(3)+V(4)+V(5))
B=3.5208+(4.35E-3*Y(3)+1.20E-3*Y(2)+1.85E-3*Y(4)
+3.40E-3*Y(5)+0.2E-3*Y(6)+4.12E-3*Y(7)+6.3E-3*Y(8))
C=3.5240+(4.35E-3*V(3)+1.20E-3*V(2)+1.85E-3*V(4)
+3.40E-3*V(5)+0.2E-3*V(6)+4.12E-3*V(7)+6.3E-3*V(8))
SSS=-12.36+2.60*Y(6)-1.42*Y(2)-1.35*Y(3)+2.75*Y(7)
OVERS=-106.42+1.58*Y(6)+1.43*Y(2)+4.70*Y(3)+7.45*Y(7)
&+5.79*Y(4)+6.76*Y(5)+11.27*Y(8)
PS=OVERS-SSS
OVERS=9.08*OVERS
SSS=9.08*SSS
PS=9.08*PS
M=((B-C)/B)*100
```

```
DO 300 I=1,8
VAC(I)=V(I)/100*P(I)
SUMVAC=VAC(1)+VAC(2)+VAC(3)+VAC(4)+VAC(5)+VAC(6)+
+VAC(7)+VAC(8)
300 CONTINUE
IF (SUMVAC .LE. 2.30) THEN
CALL STARS
WRITE (6,*) 'Elec.Vac.Conc. is ' ,SUMVAC, 'Matrix stable'
ELSE
CALL STARS
WRITE (6,*) 'Elec.Vac.Conc. is ' ,SUMVAC, 'TCP may form'
ENDIF
UTS20=461.9+12.91*S(2)+2.473*S(6)+15.85*S(3)+9.621*S(7)
&+26.95*S(8)+34.44*S(4)+32.51*S(5)
UTS650=148.2+11.39*S(2)+4.088*S(6)+14.82*S(3)+11.80*S(7)
&+29.21*S(8)+82.19*S(4)+61.05*S(5)
UTS760=96.52+12.16*S(2)+1.008*S(6)+20.40*S(3)+15.19*S(7)
&+33.17*S(8)+88.68*S(4)+58.29*S(5)
UTS871=56.53+5.184*S(2)+2.559*S(6)+23.87*S(3)+12.93*S(7)
&+28.21*S(8)+84.14*S(4)+37.96*S(5)
UTS982=37.23-3.992*S(2)-0.0091*S(6)-0.55*S(3)+6.53*S(7)
&+20.05*S(8)+67.91*S(4)+42.92*S(5)
LATMIS=1.216-0.00202*S(1)+3.697D-3*S(2)+1.09D-1*S(3)
&+0.7708D-1*S(4)
&-0.4055D-1*S(5)-6.479D-3*S(6)-3.787D-3*S(7)-3.563D-3*S(8)
CALL STARS
WRITE (6,99)
WRITE (6,119) (S(I),I=1,8)
WRITE (6,120) (A(I),I=1,8)
WRITE (6,121) (Y(I),I=1,8)
WRITE (6,122) (V(I),I=1,8)
CALL STARS
WRITE (6,123) F
CALL STARS
WRITE (6,124) B
WRITE (6,125) C
WRITE (6,126) M
CALL STARS
CALL STARS
```

```
WRITE (6,127) T
CALL STARS
WRITE (6,89)
WRITE(6,899)UTS20,UTS650,UTS760,UTS871,UTS982
WRITE(6,8999)LATMIS
CALL OUTPUT
99 FORMAT(' NI CR MO AL TI CO
+W TA ')
119 FORMAT(' WPERCT: ',8(2X,F5.2))
120 FORMAT(' ALCOMPOS:',8(2X,F5.2))
121 FORMAT(' COMGAMPR:',8(2X,F5.2))
122 FORMAT(' COMPGAMA:',8(2X,F5.2))
123 FORMAT(' VOLFRACT:',F5.3)
124 FORMAT(' GAMPRLAT:',F6.4)
125 FORMAT(' GAMALATI:',F6.4)
126 FORMAT(' LATMISFT:',F8.5)
127 FORMAT(' THERMAL EXPANSION COEFFICIENT AT 538 0C *10E-6: ' ,F5.2)
89 FORMAT(' UTS20 UTS650 UTS760 UTS871 UTS982 ')
899 FORMAT(' MPA:',5(2X,F7.2))
8999 FORMAT(' REGRESSION ANALYSIS RESULTS LAT MISFIT:',F7.5)
GOTO 201
200 STOP
END
SUBROUTINE STARS
WRITE (6,*) '***********************************************'
END
SUBROUTINE OUTPUT
WRITE (6,*) ' '
WRITE (6,*) ' '
END
%
```

APPENDIX 7: SCANNING ELECTRON MICROGRAPHS OF HIGH-SI CONTAINING CASTS

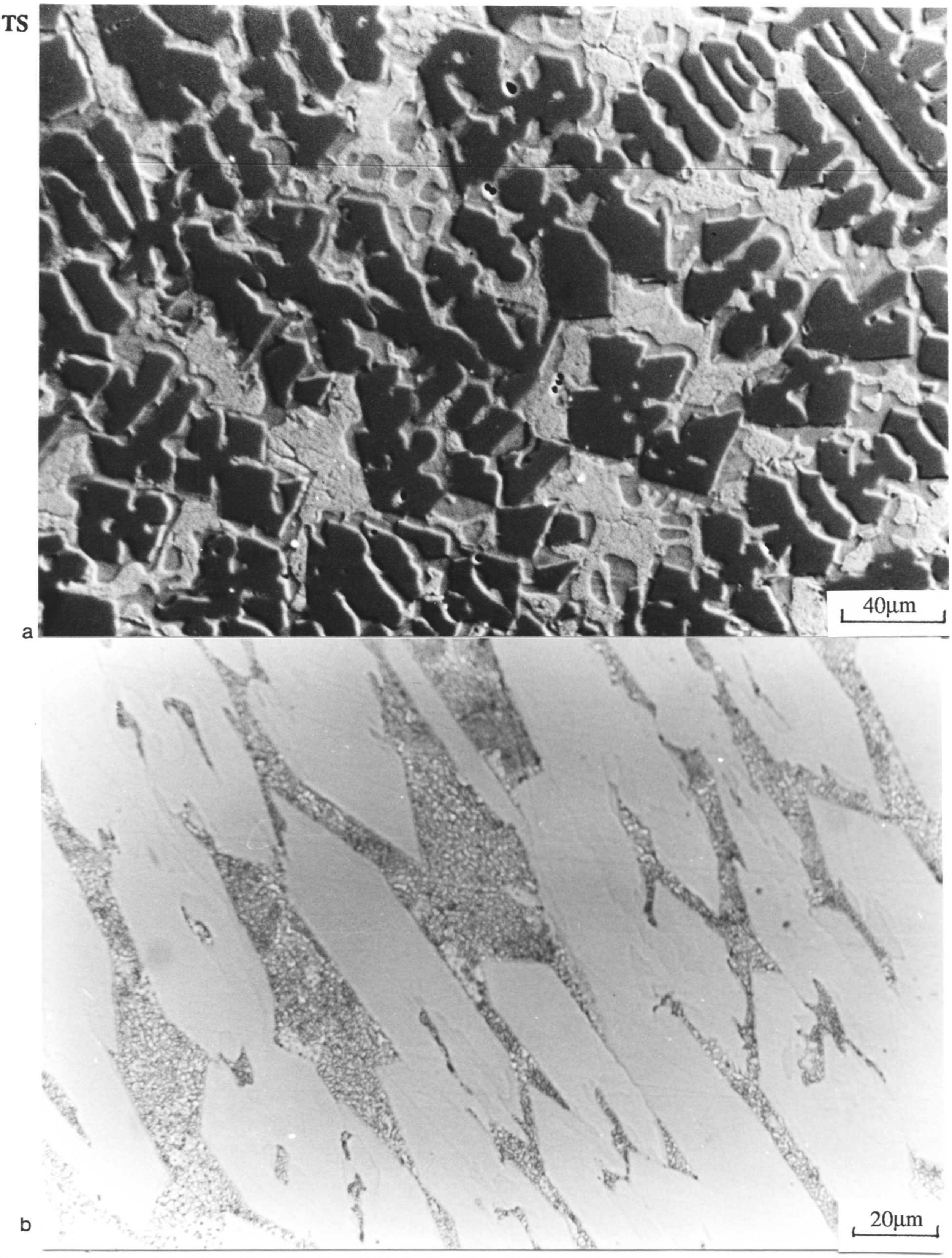

Fig. 1: a) Fe-27.9Cr-15.9Si-3.29C; b) Fe-26.28Cr-20.80Si-3.23C wt%. The primary phase is FeSi intermetallic compound which has a hardness of ≈1600HV.